Identification of muscle activation schemes by inverse methods applied on HD-sEMG signals

Soumaya Berro

Par **Soumaya BERRO**

Identification of muscle activation schemes by inverse methods applied on HD-sEMG signals

Thèse présentée
pour l'obtention du grade
de Docteur de l'UTC

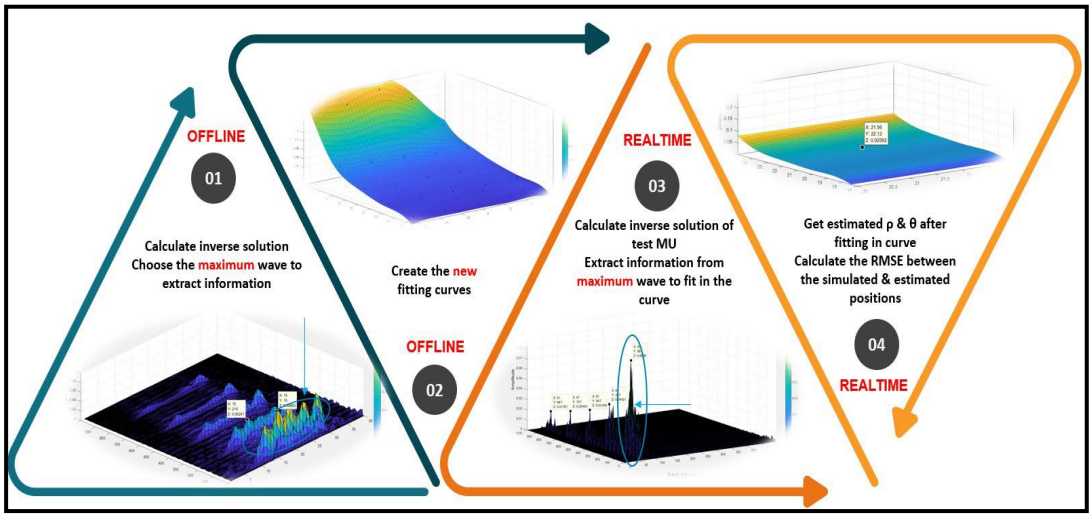

Soutenue le 22 novembre 2022
Spécialité : Bioingénierie : Unité de Recherche en Biomécanique et Bioingénierie (UMR-7338)

D2708

THESIS presented to:

Sorbonne University, Université de Technologie de Compiègne (UTC)

Doctoral school « Sciences pour l'ingénieur »

for the Degree of Doctor

Spécialité : Bioingénierie

Speciality: Bioengineering

Titled:

Identification of muscle activation schemes by inverse methods applied on HD-sEMG signals

Presented and publicly defended by:

SOUMAYA BERRO

22/11/2022

Jury members:

Régine Le Bouquin Jeannès	Prof., Université de Rennes 1	Reviewer
Mohamad Ayache	Associate Prof., Beirut Arab University	Reviewer
Catherine Marque	Prof., Université de Technologie de Compiègne	Examiner
Amar Kachenoura	Research Engineer, Université de Rennes 1	Examiner
Ahmad Diab	Associate Prof., Lebanese University	Co-supervisor (invited)
Mohammad HajjHassan	Associate Prof., Lebanese International University	Co-supervisor (invited)
Mohamad Khalil	Prof., Lebanese University	Co-director
Sofiane Boudaoud	Prof., Université de Technologie de Compiègne	Director

“Remember to look up at the stars and not down at your feet. Be curious. And however difficult life may seem, there is always something you can do and succeed at.”

___ Stephen Hawking

Acknowledgements

Firstly, I would like to give my warmest thanks my director Prof. Sofiane Boudaoud and my co-director Prof. Mohamad Khalil who made the accomplishment of this thesis work possible through their consistent guidance, mentoring, and encouragement. The completion of this work could not have been possible without their vision, expertise, and valuable advice. It was a great privilege working under their direction. Indeed, I feel like I have significantly grown on the scientific and professional level thanks to them.

Also, I would like to sincerely acknowledge the hard work and dedication of my co-supervisors Dr. Ahmad Diab and Dr. Mohammad HajjHassan. Their aid was no less important and had an essential impact on the progress of my work and its success. Without their help and constant feedback, this PhD would not have been attainable. Thank you for the significant contribution you added to my thesis work.

In addition, I would like to thank the rest of my defense jury members Prof. Régine Le Bouquin Jeannès, Prof. Catherine Marque, Dr. Mohamad Ayache, and Dr. Amar Kachenoura. Thank you for your presence and for your time.

Finally, a special thanks to my mother Fayze, my father Mohamad, and my sisters Hiba, Nour, Zeinab, and Aya. Your love and support made me do it all.

Résumé

L'identification rapide ou en temps réel de l'activation spatio-temporelle des unités motrices (UM) qui représentent les unités fonctionnelles du système neuromusculaire est fondamentale dans les applications de contrôle des prothèses et en réhabilitation fonctionnelle. Cependant, cette procédure demande un temps de calcul énorme. Par conséquent, le travail de cette thèse a été consacré à fournir un algorithme permettant l'identification en temps réel des stratégies d'activation spatiale et temporelle des UMs en appliquant des méthodes inverses sur les signaux HD-sEMG (électromyogramme de surface à haute densité) à partir d'une grille placée sur le Biceps Brachial (BB). À cette fin, nous proposons une approche innovante, qui implique l'utilisation de la méthode inverse classique de minimisation de norme et une interpolation de courbe en 3D, à savoir l'approche est nommée CFB-MNE. Cette méthode, fondée sur l'identification inverse (estimation de la norme minimale) couplée à un dictionnaire des potentiels d'action des unités motrices simulées (MUAP) d'un modèle récent et testée sur des simulations, a permis la localisation en temps réel des unités motrices individuelles simulées. Une analyse de robustesse (modifications anatomiques, physiologiques et instrumentales) a ensuite été effectuée pour vérifier l'efficacité de l'algorithme proposé. Enfin, l'algorithme proposé a été testé sur des UMs avec des schémas de recrutement réalistes donnant des résultats prometteurs et encourageants en identification spatiale et temporelle sur trois scenarios. Pour conclure, en perspectives, les résultats prometteurs obtenus suggèrent l'utilisation de l'apprentissage automatique et de l'intelligence artificielle (IA) pour améliorer encore les performances de l'algorithme proposé.

Mots-clés: Électromyographie de surface à haute densité (HD-sEMG), localisation en temps réel, problème inverse, estimation de la norme minimale, identification spatiotemporelle.

Abstract

Fast or real-time identification of the spatiotemporal activation of Motor Units (MUs), functional units of the neuromuscular system, is fundamental in applications as prosthetic control and rehabilitation guidance but often dictates expensive computational times. Therefore, the thesis work was devoted to providing an algorithm that enables the real-time identification of MU spatial and temporal activation strategies by applying inverse methods on HD-sEMG (high-density surface electromyogram) signals from a grid placed over the Biceps Brachii (BB). For this purpose, we propose an innovative approach, that involves the use of the classical minimum norm inverse method and a 3D fitting curve interpolation, namely CFB-MNE approach. This method, based on inverse identification (minimum norm estimation) coupled to simulated motor unit action potential (MUAP) dictionary from a recent model and tested on simulations, allowed the real time localization of simulated individual motor units. A robustness analysis (anatomical, physiological, and instrumental modifications) was then performed to verify the efficiency of the proposed algorithm. Finally, the proposed algorithm was tested on MUs with realistic recruitment patterns giving promising results in both spatial and temporal identification. To conclude, a door to future perspectives was opened, according to the obtained promising results, suggesting the use of machine learning and artificial intelligence (AI) to further boost the performance of the proposed algorithm.

Keywords: High density surface electromyography (HD-sEMG), real-time localization, curve fitting technique, inverse problem, minimum norm estimation, spatiotemporal identification.

Publications

International journal papers

- Berro S., Douania I., Diab A., Hajj-Hassan M., Khalil M., Boudaoud S., "Curve Fitting Based Minimum Norm Estimation (CFB-MNE) for Motor Unit Spatial Localization Using High Density Surface Electromyogram Signals", Biomedical Signal Processing and Control (BSPC), Elsevier Journal, 2022 (Article submitted).

International conference papers

- S. Berro, A. Diab, M. Hajj-Hassan, M. Khalil, H. Amoud and S. Boudaoud, "Identification of motor unit spatial activation by minimum norm estimation," 2019 Fifth International Conference on Advances in Biomedical Engineering (ICABME), 2019, pp. 1-4, doi: 10.1109/ICABME47164.2019.8940273.
- S. Berro, A. Diab, M. Hajj-Hassan, M. Khalil, H. Amoud and S. Boudaoud, "Exploration of motor unit activation pattern using high density sEMG minimum norm estimation," 2020 IEEE 5th Middle East and Africa Conference on Biomedical Engineering (MECBME), 2020, pp. 1-6, doi: 10.1109/MECBME47393.2020.9265172.
- S. Berro, A. Diab, M. Hajj-Hassan, M. Khalil, H. Amoud and S. Boudaoud, "Retrieving motor unit depth using inverse approach on HD-sEMG signals," 2021 Sixth International Conference on Advances in Biomedical Engineering (ICABME), 2021, pp. 159-162, doi: 10.1109/ICABME53305.2021.9604853.

Glossary

Acetylcholine	**ACh**
Action Potential	**AP**
Adenosine diphosphate	**ADP**
Adenosine Triphosphate	**ATP**
Artificial Intelligence	**AI**
Biceps Brachii	**BB**
Boundary Element Method	**BEM**
Body Mass Index	**BMI**
Central Nervous System	**CNS**
Computed Myography	**CMG**
Common Impulse Response	**CIR**
Curve Fitting Based Minimum Norm Estimation	**CFB-MNE**
Energy	**E**
Electroencephalography	**EEG**
Electrocardiography	**ECG**
Electrohysterogram	**EHG**
Electromyography	**EMG**
Fast Fatigable	**FF**
Fast Intermediate	**FI**
Fast Resistant	**FR**
Finite Difference Method	**FDM**
Finite Element Method	**FEM**
Focal Underdetermined System Solution	**FOCUSS**
Fourier Transform	**FT**
High-Density sEMG	**HD-sEMG**
Imaging Electromyography	**iEMG**
Impulse Response	**IR**
Inter Electrode Distance	**IED**
Low-Resolution Electromagnetic Tomography	**LORETA**
Magnetic Resonance Imaging	**MRI**
Maximal Voluntary Contraction	**MVC**

Mean Square Error	**MSE**
Minimum Norm Estimation	**MNE**
Motor Unit	**MU**
MU Action Potential	**MUAP**
Model Aided Diagnosis	**MAD**
Motor Unit Potential	**MUP**
Muscle Activity Imaging	**MAI**
Multiple Classification Algorithm	**MUSIC**
Neuromuscular Junction	**NMJ**
One At a Time	**OAT**
Peripheral Nervous System	**PNS**
Recursive Multiple Classification Algorithm	**RAP-MUSIC**
Root Mean Square Error	**RMSE**
Sarcoplasmic Reticulum	**SR**
Signal to Noise Ratio	**SNR**
Single Fiber Action Potential	**SFAP**
Slow	**S**
Standardized Low-Resolution Electromagnetic Tomography	**sLORETA**
Surface Electromyography	**sEMG**
Ultrasound	**US**
Weighted Minimum Norm	**WMN**
Weighted Minimum Norm Estimation	**wMNE**

Contents

List of Figures

List of Tables

General Introduction

Human motion is an interesting and complex task that requires the coordination between two major systems in our bodies: the neuromuscular and musculoskeletal systems. As a matter of fact, to achieve movement, skeletal muscles must contract (neuromuscular) and work cooperatively with tendons and joints, allowing skeletal bones to move (musculoskeletal) [1, 2]. The process of muscle contraction is initiated in the CNS (central nervous system), which activates α-motor neurons (involved in voluntary movement) found in the PNS (peripheral nervous system) [3]. A synapse is then formed between the motor neuron nerve terminals and each muscle fiber called the neuromuscular junction (NMJ) [4, 5]. At this junction, a neurotransmitter is released causing the depolarization of the excitable muscle fibers and the generation of a voltage signal across its membrane [6]. Each motor neuron and the group of skeletal muscle fibers it innervates form what is known as motor units (MUs) [7]. After the depolarization of the muscle fibers, a resulting voltage signal called the motor unit action potential (MUAP) is generated. This electrical response, also known as the surface electromyogram (sEMG) can be recorded in a non-invasive manner by the help of electrodes placed at the surface of the skin [8]. More recently, the quality of information recorded at the surface of the skin was improved by using a grid of electrodes, and this method was popular as high-density surface EMG (HD-sEMG) [9]. Embedded in such a signal set is a lot of valuable information about the MU activations resulting in it. Indeed, a major concern when studying the musculoskeletal system is investigating how areas within the muscle (formed from MUs) are tuned by the neural drive to perform several activation strategies for different motions. This kind of data is key in the diagnosis of neuromuscular diseases and phenomena (such as muscle fatigue and muscle aging) and the in depth exploration of the physiology of skeletal muscle in sports

sciences and rehabilitation [10, 11]. Thus, the spatial and temporal localization of the MUs is of a great importance [12, 13, 14, 15]. Because MUAPs are produced before the production of force by the muscle, provoking an electromechanical delay [16], those muscle signals (where and when they originated from) can be analyzed and used to anticipate the motor purpose which then can be converted into an action before the real movement. To make this possible, the spatio-temporal localization of the MUs must be done in real-time and hence fast processing is required. This can be useful for applications involving possible prosthetic control improvement and rehabilitation guidance [17,18]. When speaking of real-time analysis, researcher's attempts were restricted to the real-time decomposition (identifying MU spike trains or discharge times only) of intramuscular EMG signals [19] or HD-sEMG signals [16]. However, available attempts targeting the non-invasive spatial localization of the MUs dictated elevated computational durations [20 ,21, 22]. Regarding the real-time spatial localization, to our knowledge, it was not yet available until recently, when a promising study was done by Mesin [20]. Mesin demonstrated the ability to spatially localize regions within the muscle (consisting of several MUs) using a mathematical formalism known as the inverse problem coupled to a pre-simulated MUAP dictionary. This approach was applied to HD-sEMG signals. Motivated by this study and the promising applications it holds [20], and given the scarcity of the available real-time methods for the spatiotemporal localization of single MUs from HD-sEMG signals, the development of a new technique that tackled this issue was identified as a clear need. For this purpose, in this thesis, we will propose a novel real-time spatiotemporal localization technique that can be applied to HD-sEMG signals and retrieve accurate information about individual MUs resulting in those signals using the inverse problem approach coupled with an analytical cylindrical muscle model [23] for dictionary construction. This real-time spatiotemporal localization technique

(tested on simulation) will be applied considering the voluntary and isometric contraction of fusiform skeletal muscles (not pennate) and particularly the Biceps Brachii (BB). Accordingly, this manuscript is divided into three parts:

- Chapter 1: In the first chapter, we will initially introduce the structure and function of the skeletal muscle system including the characteristics and type of skeletal muscle contraction, the anatomy and neural control of skeletal muscles, and the physiology of skeletal muscle contraction (including the electrical and mechanical events). Afterwards, we will demonstrate the correlation between the spatial activation of MUs within a muscle and between certain muscular diseases. Then, we will introduce the HD-sEMG and decomposition techniques and their limitations. Moreover, we will continue by discussing the existing surface EMG (sEMG) forward and inverse methods. Consequently, we will then define and introduce the concept of real-time MU localization and the useful applications it participates in. Finally, we will conclude this chapter by emphasizing on the thesis problematic and main objectives and the innovative aspects of the proposed work.
- Chapter 2: In this chapter, we will first use a simplified and fast single layer and planar muscle model to preliminary test the proposed inverse algorithms. In fact, using this model, we will test two different inverse problem formalisms, the MNE and wMNE. Then, we will propose a predictive spatial identification technique using a 1 D fitting curve constructed from information extracted from the 3D inverse solution space using a dictionary of pre-defined MUs with known discharge times and locations. In the second section of this chapter, we will improve the previous identification methodology, namely CFB-MNE approach, by using a more realistic generation model of the HD-sEMG

signals (which will also be described in detail) and by creating a 3D fitting curve that will aid in the prediction of the spatial localization of MUs using the inverse solution space. In the final section of this chapter, the same algorithm will be tested on other inverse methods (such as the sLORETA).

- Chapter 3: In the final chapter, we will evaluate the robustness of the proposed methods and algorithms. First, we will test how effective the algorithm is in dealing with superposition, where several MUs are recruited at same time during the muscle contraction. We will then test if the algorithm can differentiate between different types of MUs (based on the fiber type composition). Afterwards, we will test if the algorithm must be personalized according to the patient (personalized dictionaries) or if a generic algorithm (generic dictionary) can be used. For this, we will perform a robustness analysis to certain physiological and instrumentational changes. We will assume that there is a difference between, first, one of the instrumentational parameters (the amount of Gaussian additive noise, the change in the number of electrodes in the measuring grid, and the misalignment of the detection grid with respect to the fibers). Secondly, the difference will concern physiological/anatomical parameters (mean conduction velocity value, muscle radius of the analyzed muscle anatomy, fiber length, and fat thickness). After, we will test, using three scenarios, the ability of the method to accurately identify spatiotemporal information from simulated more realistic MU recruitment patterns. Finally, we will discuss the obtained results focusing on their potentials and limitations and open door to prospective future works that can improve the proposed method for the purpose of clinical applications.

Chapter 1

State of the Art and Problematic

Contents

1.1 Introduction

Movement is a vital aspect of life for all living creatures and especially for human beings. Everything is influenced by movement, from the circulation in our body, to the metabolic activities in it, to how our immune system responds, and to how it even digests. With proper movement, we would be able to have strong joints and bones, we will be more powerful physically, we will have a better cardiovascular circulation, and accordingly enhanced concentration. In other words, movement is central for our overall well-being. For movement to occur, an interaction between the brain and muscles should take place (as shown in Figure 1.1). First, an order should be sent and then an actuation must happen. Hence, there is a need for a command center and an execution center. The nervous system (brain and nerves), which is the command center, relays a message through neurons to stimulate the skeletal muscles, which are the execution center.

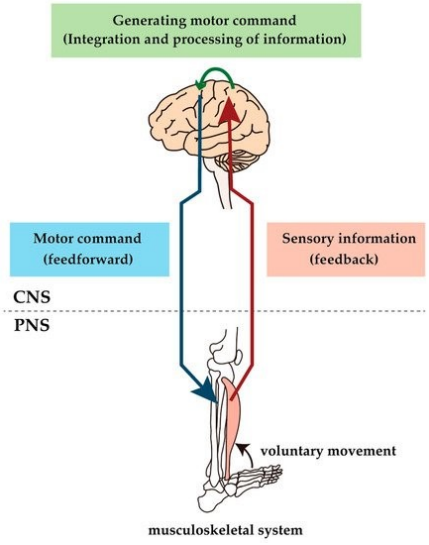

Figure 1.1: A depiction of the interaction of the neuromuscular and musculoskeletal systems in human body [3].

Accordingly, upon stimulation, our skeletal muscle will respond by producing motion. Thus, a complex coordination within the neuromuscular system at the first level, and with the

musculoskeletal system at the second level will occur [1, 2]. Indeed, when we intend to move, a message is relayed along the Peripheral Nervous System (PNS) (which is in turn controlled by the Central Nervous System (CNS)) to the skeletal muscle fibers by the aid of motor neurons. The axon terminal of a motor neuron and the muscle fibers it innervates form what is known as motor units (MUs) [3]. The recruitment of the MUs [6] leads to an electrical phenomenon known as the depolarization of the muscle fibers. This electrical signal can be detected by electrodes positioned at the surface of the skin. This crucial diagnostic technique is called surface electromyography (sEMG) [8]. Advances in the detection of the electromyographic signal from the surface of the skin included using a high-density electrode grid, a technique called high-density surface EMG (HD-sEMG) [9], to improve the characteristics of the signal recorded from the surface of the skin.

As a matter of fact, a sEMG signal combines the motor neuron temporal discharges with the action potentials of the innervated muscle fibers (which have specific spatial locations). This information is frequently employed as a rich source about neural drive leading to the activation of muscle [24]. Exploring the neural drive through the identification of the spatio-temporal MU recruitment scheme is of a great interest since it helps in the diagnosis of neuromuscular diseases and better knowledge of the physiology of skeletal muscle in sports sciences and rehabilitation [10, 11]. Whatsoever, extracting such information from the sEMG signal (non-invasively) is super challenging [24].

For this reason, this thesis will tackle the investigation and testing of signal processing methods related to better exploring the neuromuscular system and gaining an in-depth understanding of the mechanisms underlying muscle contraction through the analysis of surface electromyographical signals.

This work is motivated by the scarcity of existing non-invasive methods that enable the real-time localization of active MUs within the muscle during contraction. Usually, such information cannot be yielded without sophisticated invasive setups [25] or without requiring significantly expensive computational durations [20, 21, 22], the thing that will hinder the usage of such information in medical applications that require immediate intervention. Therefore, in this thesis, we propose a novel HD-sEMG based on an inverse approach for non-invasively localizing active MUs within the muscle and discovering their temporal discharges.

In this chapter, we will first present the structure and function of the skeletal muscle system (Section 1.2) including the characteristics and type of skeletal muscle contraction (sub-section 1.2.1), the anatomy and neural control of skeletal muscles (sub-section 1.2.2), and the physiology of skeletal muscle contraction (sub-section 1.2.3). After that, the significance of the spatial activation of MUs and its correlation with muscular diseases will be pointed out (sub-section 1.3). Then, the HD-sEMG and decomposition techniques will be introduced (Section 1.4). This will be followed by a detailed survey of the existing surface EMG (sEMG) forward and inverse methods and the significance of real time localization (Section 1.5). Finally, this chapter will be concluded by emphasizing on the thesis problematic and main objectives (Section 1.6).

1.2 Skeletal muscle system: structure and function

The muscle tissue is considered as a major part that forms the body and it usually constitutes around 40-50% of our total body weight. It is possible to differentiate between three different muscle types which are the **cardiac**, **smooth**, and **skeletal** muscles. Cardiac muscles participate in the process of the contraction of the heart enabling it to act as a pump, smooth muscles usually line hollow organs such as the walls of the intestines, and skeletal muscle which surround our bone enabling our body to produce movement. Among those muscle types, cardiac

and skeletal muscles are distinctively straited in appearance while the smooth ones are non straited. The difference between the cardiac and skeletal muscles is that the former performs unvoluntary contraction whereas the latter involves voluntary contraction of the muscles [26, 27]. Other than the contractile properties, skeletal muscles come in different shapes. The various ways the fascicles (bundles of muscle fibers) are attached to the tendons result in different skeletal muscle sizes and shapes, as shown in Figure 1.2. Four basic muscle shapes are dominant over the appearance of most of the muscles. Those are the fusiform, triangular, rhomboidal, and pennate. For instance, fusiform muscles (such as the biceps brachii) are composed of fibers which are parallel to each other. At each end, those fibers narrow to a tendon, forming a fusiform (Figure 1.2(A)). On the other hand, resembling the appearance of a feather, pennate structures (like the muscles of the limbs) contain muscle fibers that reach a central tendon at an oblique angle (Figure 1.2(D)) [28, 29]. In this thesis, the work is dictated on the fusiform skeletal muscles and specifically the Biceps Brachii (BB).

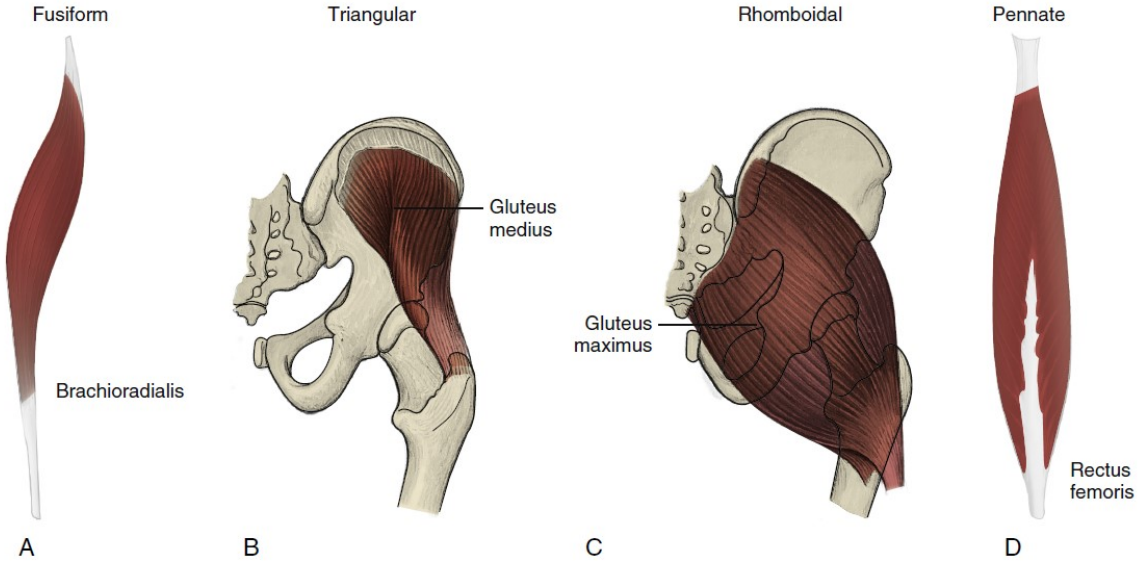

Figure 1.2: Most common shapes of skeletal muscles: (A) fusiform, (B) triangular, (C) rhomboidal and (D) pennate [29].

1.2.1 Skeletal muscle characteristics and types of contraction

As a matter of fact, a skeletal muscle possesses four key traits [4] that enables it to accomplish its tasks:

- **Excitability**: is the muscle's responsiveness or ability to respond by contracting after receiving a definite external stimulus.
- **Contractility**: is when the muscle is capable, upon proper stimulation, to shorten in a forcible manner.
- **Extensibility**: is the possibility of the extension or stretching of the muscle, which should be differentiated from contraction, since a muscle can contract but can also increase its length longer than its initial resting length.
- **Elasticity**: is the recoiling capability of a muscle following a stretching action.

As a matter of fact, based on the type of contraction, the length of the muscle might change or might remain the same. Accordingly, it is possible to differentiate between two different types of muscle contraction which are the isotonic and isometric contractions (Figure 1.3).

- Isotonic: The "iso" in this type means the same and the "tonic" refers to tension. This implies that in this type of contraction the tension is constant but the muscle changes in length. As soon as enough tension is produced to move a load, this tension remains stable during the period of contraction. Based on the type of change of length that a muscle will undergo, this category can further be divided into two types [4]:
    - Concentric: includes the shortening on the muscle, as shown in Figure 1.3 (a), and this occurs when doing actions such as kicking a ball.

- Eccentric: includes the lengthening of the muscle, and usually occurs in the calf muscles when you attempt to walk an inclined or steep mountain.

- Isometric: The "metric" in this word means same measurement. Hence, no change in muscle length is involved in this type of contraction where the myotendineous system neither shortens nor lengthen (as shown in Figure 1.3 (b), but the tension can increase up to the maximum capacity of the muscle [4].

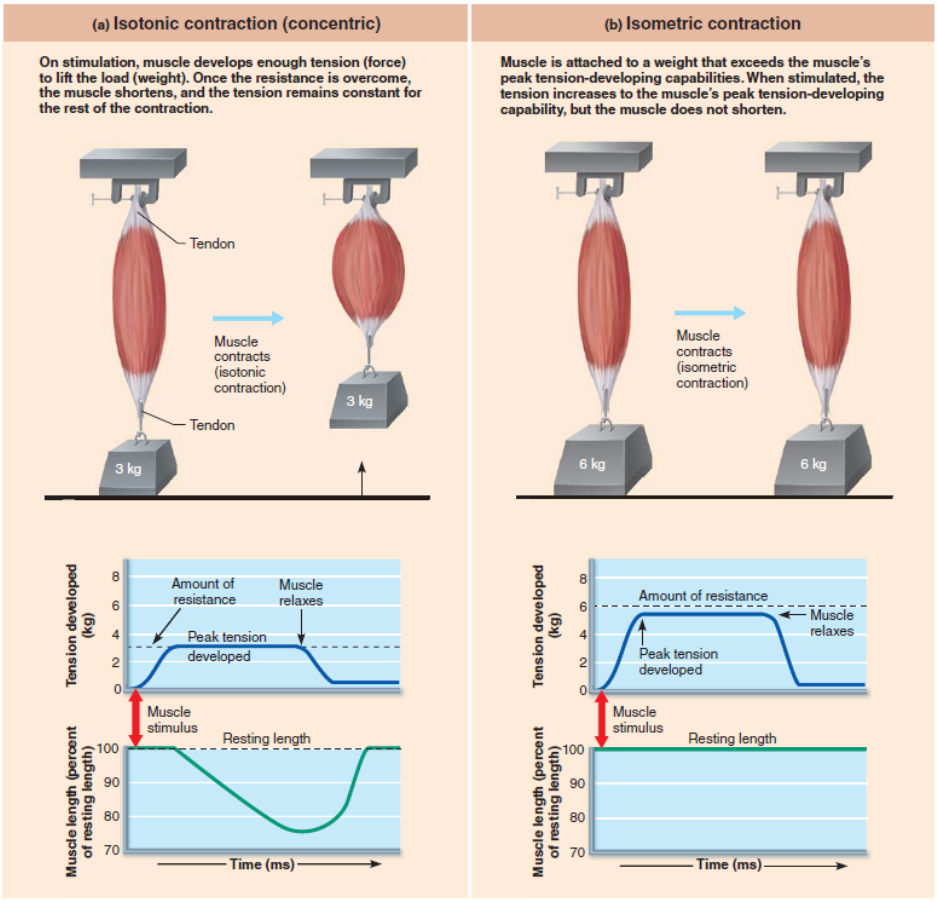

Figure 1.3: A depiction of the difference between isotonic (a) and isometric (b) contractions [4].

The work in this thesis will bear on the use of muscle models producing **voluntary and isometric contractions of the Biceps Brachii**.

1.2.2 Anatomy and neural control of skeletal muscles

Skeletal muscles are connected to the bones through tendons. The outermost surface of the whole muscle is wrapped by a connective layer called the **epimysium**, which is a collagenous membrane. Every skeletal muscle is composed of thousands of **muscle fibers (myofibers)**. Those fibers group together to form bundles known as **fasciculi**, where each fasciculus is surrounded by a connective layer called the **perimysium**. The size of each bundle can vary according to the number of myofibers it holds (it ranges between tens to hundreds of fibers per bundle). Myofibers themselves can also have variable length and diameter; myofiber diameter usually range from 10µm to 100µm and their length fluctuates between 10 and 30cm depending on the type of muscle [4, 27].

Also, inside each bundle, each myofiber is covered by a connective layer called the **endomysium**. Myofibers are excitable cells composed of a **myonucleus** which is situated at the periphery of the myofiber directly below the plasma membrane of the muscle cell which is known as the **sarcolemma**. Inside each myofiber are contractile filaments known as the **myofibrils**. Within the sarcolemma are infoldings into the myofiber termed as **transverse tubules**. Those tubules play an important role in the fast release of calcium (needed for muscle contraction) from the inner **sarcoplasmic reticulum (SR)** (which are fluid-filled membrane sacs surrounding each myofibril and storing calcium ions) to the cytoplasm after depolarization occurs (Figure 1.5) [4, 30].

These tunnel-shaped tubules are recurrently present along the myofiber near the myofibrils. The cylindrically shaped myofibrils, which usually have a diameter of around 2µm, form a special recurring striated pattern when grouped together known as **sarcomeres** (Figure 1.4-A); those are

the basic contractile unit within a skeletal muscle. Each sarcomere is composed of two distinct types of **myofilaments** called **actin** (thin) and **myosin** (thick) [4, 30].

Indeed, throughout a sarcomere, several bands can be differentiated. Generally, a dark region is called the **A band** and a light region is known as the **I band**. The dark A band is composed of both myosin and actin myofilaments (where they might overlap depending on the status of the muscle) whereas the light I band is due to the presence of the actin myofilaments alone. Within the A band, there is a region where the actin and myosin do not overlap, and this is called the **H band**. Centering this band is a region called the **M band** (Figure 1.4-B). This band serves as a support for myosin filaments due to its filamentous nature [31, 32].

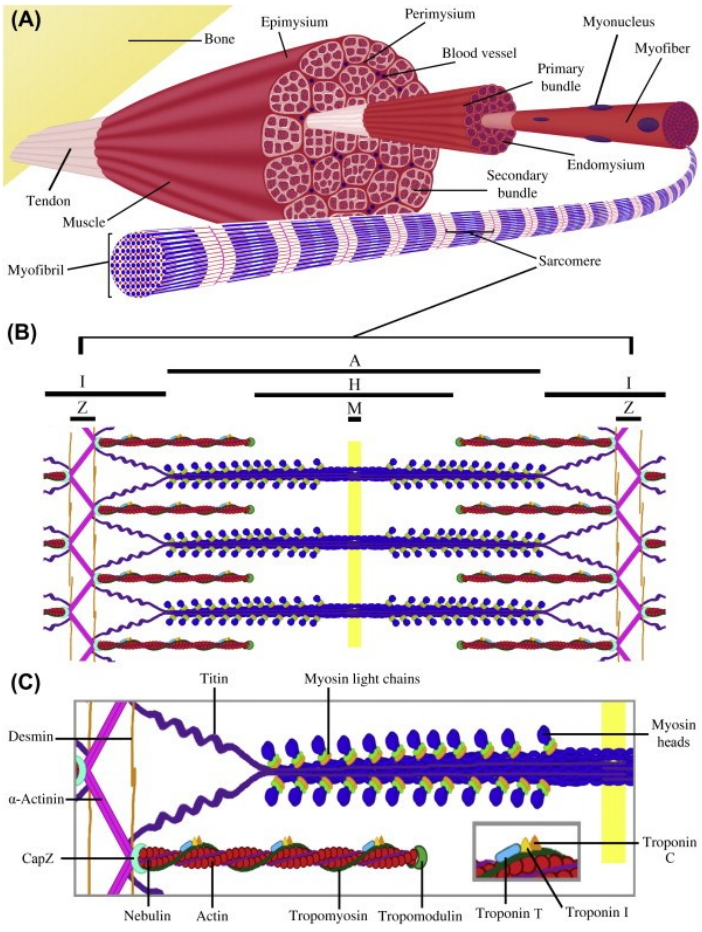

Figure 1.4: Skeletal muscle fiber anatomy [31].

The same can be said about the I band which is also centered by a region termed the **Z band** (Figure 1.4-B) or the **Z disc** in which actin filaments are found. As a matter of fact, each sarcomere extends from one Z disc to the other with a typical length of 2.2µm when at rest. This is also displayed in Figure 1.5. More specifically, actin filaments are double helical structures composed of nebulin, actin, tropomyosin, troponin I, T and C, and tropomodulin (Figure 1.4-C). α-Actinin and CapZ ensure the attachment of those thin filaments to the Z band. Tropomodulin, which encapsulates the tail of the thin filament nearest to the M band (Figure 1.4-B & C), plays the role of controlling the length of the actin filament. Meanwhile, bond to the surface of the tropomyosin is the troponin complex that holds Troponin I, T, and C (Figure 1.4-C) [31, 32]. Those play an essential regulatory role in the interaction between the myosin head and the actin filament. Finally, nebulin is a protein capable of binding to actin and can affect the length and contractile characteristics of the actin. As for the myosin, which is a protein dimer, it incorporates two heavy chains and two types of light chains (Figure 1.4-C) [30, 32]. A summary of the structural and organizational levels of a skeletal muscle fiber is presented in Figure 1.6.

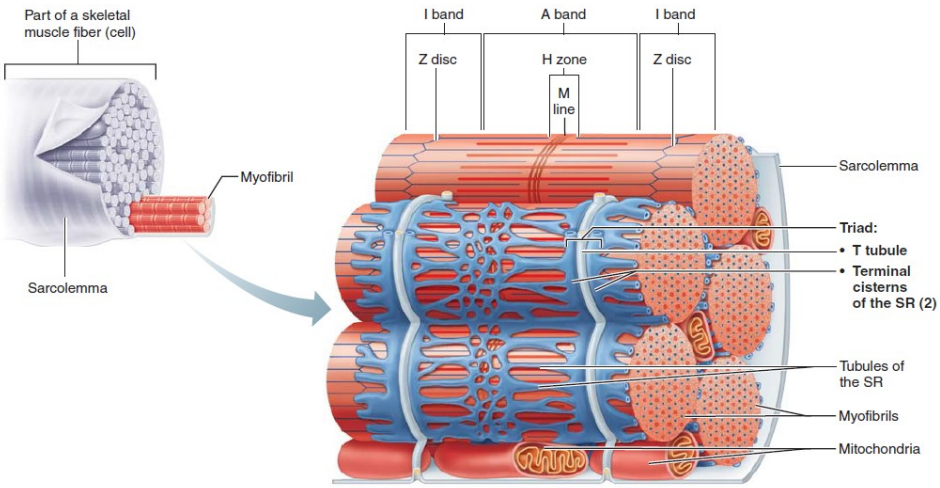

Figure 1.5: Muscle fiber structure [4].

STRUCTURE AND ORGANIZATIONAL LEVEL	DESCRIPTION	CONNECTIVE TISSUE WRAPPINGS
Muscle (organ) 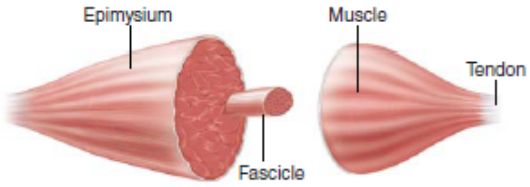	A muscle consists of hundreds to thousands of muscle cells, plus connective tissue wrappings, blood vessels, and nerve fibers.	Covered externally by the epimysium
Fascicle (a portion of the muscle) 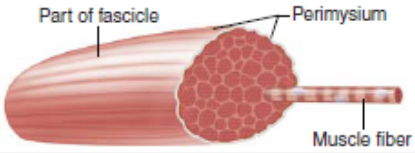	A fascicle is a discrete bundle of muscle cells, segregated from the rest of the muscle by a connective tissue sheath.	Surrounded by perimysium
Muscle fiber (cell) 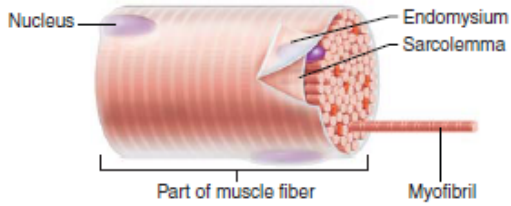	A muscle fiber is an elongated multinucleate cell; it has a banded (striated) appearance.	Surrounded by endomysium
Myofibril, or fibril (complex organelle composed of bundles of myofilaments) 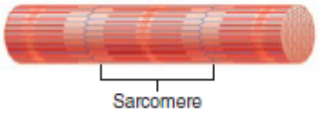	Myofibrils are rodlike contractile elements that occupy most of the muscle cell volume. Composed of sarcomeres arranged end to end, they appear banded, and bands of adjacent myofibrils are aligned.	—
Sarcomere (a segment of a myofibril) 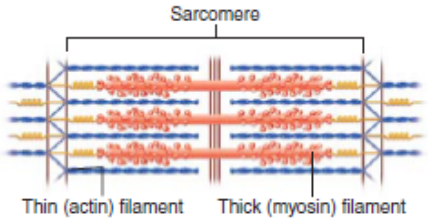	A sarcomere is the contractile unit, composed of myofilaments made up of contractile proteins.	—
Myofilament, or filament (extended macromolecular structure) 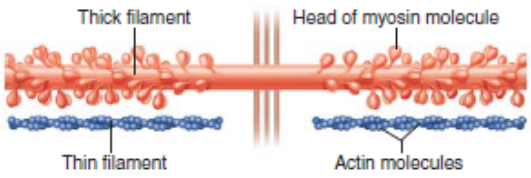	Contractile myofilaments are of two types—thick and thin. Thick filaments contain bundled myosin molecules; thin filaments contain actin molecules (plus other proteins). The sliding of the thin filaments past the thick filaments produces muscle shortening. Elastic filaments (not shown here) maintain the organization of the A band and provide elastic recoil when tension is released.	—

Figure 1.6: Structure and organizational levels of a skeletal muscle [4].

a) Types of fibers

There is a huge difference in various types of muscle fibers regarding contraction rate, metabolic properties, and way of functioning. Generally, it is acceptable to categorize the muscle fibers into two distinct types which are the slow type I fibers and the fast type II fibers [31, 33, 30]. More specifically, depending on biochemical characteristics, human skeletal muscle fibers are slow oxidative type I fibers, fast glycolytic type IIB fibers, or fast oxidative-glycolytic type IIA fibers, or intermediate type IIX fibers.

- Type I fibers (**slow-twitch**): those fibers, which have a small cross-sectional area compared to other fiber types, are characterized by being slow-twitching and rely on aerobic /oxidative phosphorylation to gain their Adenosine Triphosphate (ATP) in a slower manner than the other fibers [31]. Since those fibers are the smallest in size, they produce the least force during contraction. However, owing to their higher aerobic capacity and higher blood supply required for continuous activity, they have **high resistance to fatigue** and thus are most appropriate for contractions that require endurance. For instance, those fibers are dominant in activities that requires a sustained posture such as standing. Also, those fibers are known to be red fibers, which hold a lot of mitochondria and the protein myoglobin, giving the red color of the fibers [33].
- Type II fibers (**fast twitch**):
    - Type IIB (fast-twitch glycolytic): The largest density of actin and myosin proteins are found in this type of fibers, and therefore they are known to have the largest diameter and thus can produce the greatest force and are usually more found in superficial muscles. Those fibers are famous of having the fastest twitching with the greatest force but for a short duration of time. This is because those fibers

depend on anaerobic/glycolytic metabolism, which require a much lower energy during glucose oxidation (gluconeogenesis happens in the liver) and the energy is therefore consumed in a quicker manner enabling the fibers to produce very fast but brief spike of activity. Therefore, those fibers have high sensitivity to muscle fatigue (**low resistance to fatigue**) [31]. Due to a low level of myoglobin and a high concentration of glycolytic enzymes and glycogen stores (since those fibers rely on glycolysis to produce ATP), those fibers are known to be white fibers [33].

- Type IIA (fast twitch oxidative/glycolytic): Those fibers share a similar composition to type I fiber and thus are also considered as red fibers. Though those fibers have fast contractions and mainly use oxidative metabolism, it might shift to anaerobic/glycolytic metabolism and hence can fatigue quicker than type I fibers. However, this type is **more resistant to fatigue** that the other type II fibers [31].
- Type IIX: This type of fibers has properties **intermediate** between the two other type II fibers and hence possess mid characteristics between being fast resistant and fast fatiguable [33].

Accordingly, fibers can also be classified as fast fatigable (**FF type IIB**), fast fatigue resistant (**FR type IIA**), fast intermediate (**FI type IIX**), or slow fibers (**S type I**) [34].

b) The motor unit

The neural system controls the contraction of the skeletal muscles in a voluntary manner through what is known as an **α-motor neuron**. An α-motor neuron is a somatic motor neuron (or

a lower motor neuron which is situated inside the ventral horn of the spinal cord), that forms synapses with skeletal muscles.

When it comes to muscle contraction, the actuation of the muscle fibers does not happen individually but rather in groups. The main functional unit within the neuromuscular system, first recognized by Sherrington [7], is the **motor unit** (MU). It is composed of a single α-motor neuron, which in turn has its dendrites and axon, and the group of muscle fibers that this axon innervates at its ends, forming a synapse called a **neuromuscular junction** (NMJ). This is displayed in Figure 1.7. Only a single NMJ is formed for each muscle fiber, and it is usually positioned almost in the middle of the fiber length [4, 5].

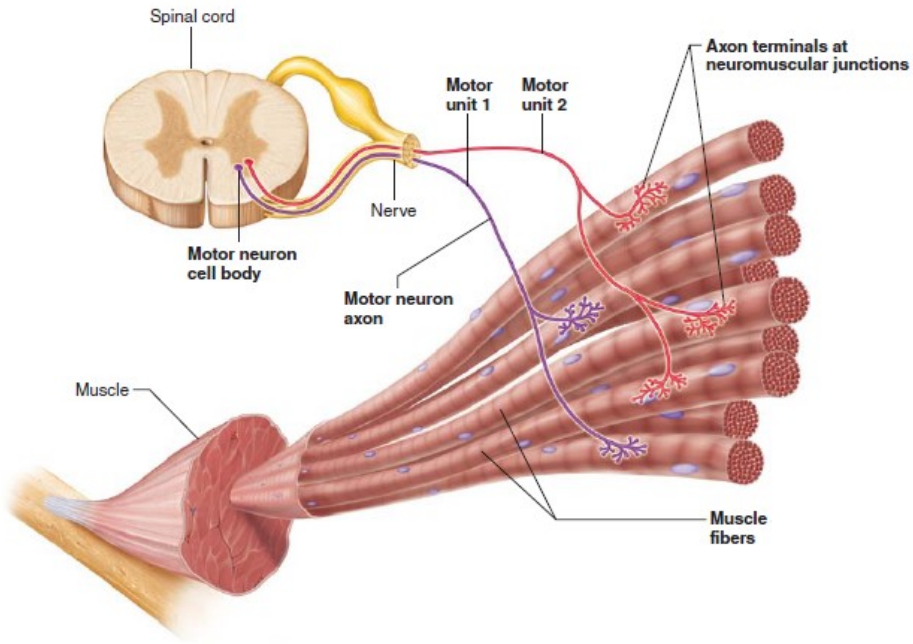

Figure 1.7: Schematic of MU taken from [4].

The kind of communication that happens between the axon terminals and the muscle is a chemical one through a neurotransmitter called **acetylcholine** (ACh), which is filled in the **synaptic vesicles** found in the **axon terminals**. The **motor end plate** is described as the

junctional folds of the sarcolemma of the muscle fiber directly facing the synaptic terminals of the axon of the neuron. Millions of ACh receptors are found in the large surface area provided by those folds.

Even though, only a short distance of 50–80 nm separates the axon terminals from the muscle fiber, those two never meet and are disconnected by the gap in between them called the **synaptic cleft**. Therefore, the NMJ encompasses the axon terminals, the synaptic cleft, and the junctional folds [4]. This is portrayed in Figure 1.8.

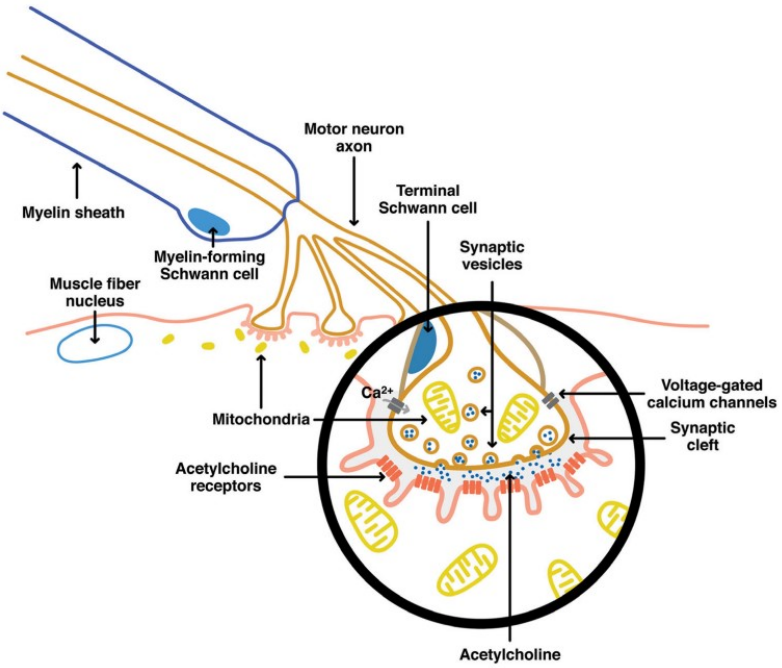

Figure 1.8: A depiction of the neuromuscular junction (NMJ), taken from [5].

The number of muscles fibers that can be innervated by a single motor neuron depends on the size and the function of the muscle. The estimated numbers of motor axons, muscle fibers, and the average number of innervations in different human skeletal muscle are summarized in Table 1.1 [35]. Indeed, the Biceps Brachii can hold up to 744 motor axons, 580,000 muscle fibers, with an average innervation number of 750.

Moreover, each muscle contains all the types of muscle fiber. However, each MU only contains a single type. As for the number of MUs within a muscle, this might fluctuate between around 100 MUs for small muscles such as those present in the hand, and around 1000 MUs for larger muscles such as those found in the legs [36]. For instance, a larger number of MUs is present in the biceps brachii (312) compared with the tibialis anterior (200) and vastus lateralis (146), which are all limb muscles [37].

Table 1.1: Estimated number of motor axons and muscle fibers in some of the human skeletal muscles [35].

Muscle	Motor axons	Muscle fibers	Average innervation number
Biceps Brachii	774	580,000	750
Brachioradialis	315/350	>129,000	>410
First dorsal interosseus	119	40,500	340
Medial gastrocnemius	579	1,120,000	1,934
Tibialis anterior	445	250,000	562

c) Neural control: Orderly recruitment and rate coding

The degree of neural activation (i.e. the MU recruitment scheme) and thus the amount of force that a muscle exerts is mainly controlled by two principles: how many motor units are employed and thus active, and this is known as spatial recruitment, and the motor unit discharging rate (rate coding) [38]. Those two events co-occur with varying levels depending on the amount of force and type of contraction.

- **Orderly Recruitment**: The recruitment of MUs follows the "size principle" introduced by Henneman [39], which imposes an orderly recruitment of MUs (they are not randomly recruited nor are all recruited at once). This means that MUs with a smaller size and weaker motor neuron-muscle fiber innervations (take more time for contraction to occur) get recruited before MUs of a larger size and more powerful motor neuron-fibers innervations (rapid contractions). Accordingly, the size principle guarantees that the MUs

are recruited in a progressive order from those that are slow to those that are fast, those that are weak to those that are stronger, and those that have less power to the more powerful introducing energetic optimization of the muscle contraction [6].

This is because smaller motor neurons are capable of firing before larger ones. The reason for this is that the membrane surface area of a small motor neuron is smaller and thus contains fewer ionic channels, making this membrane have a higher input resistance. Meanwhile, the inverse happens for larger motor neurons which own more ionic channels and thus have lower input resistances. Hence, having a high input resistance, a small motor neuron will only require a small level of synaptic current for the membrane potential of this motor neuron to amount to the threshold above which it will fire. On the other hand, a larger current will be required to bring the membrane potential of a larger motor neuron up to the firing threshold. Moreover, the recruitment threshold distribution of MUs was suggested to happen in an exponential manner (Figure 1.9(a)) [40, 41]. As shown in Figure 1.9(c), for higher percentages of MU recruitment in muscles (above 50% of MUs recruited) the contraction levels vary between 50% to 90% of the maximum voluntary contraction (MVC) force [38].

- **Rate Coding**: The control of the amount of force to be exerted by a muscle is also dictated by the rate code that motor neurons use. This rate code can be also described as the modulation of the rate at which action potentials are discharged from a motor neuron. This is the underlying principle describing the force-frequency relationship in MUs. Although the recruitment order of MUs (based on the size principle) is similar for different types of contractions, the same does not apply for rate coding. In fact, during slow ramp contractions, where the force is progressively increasing, the discharging rate

of a MU increases in a gradual manner increasing twitch (mechanical output) superposition. Meanwhile, during fast ballistic contractions, where the force production is the most rapid, the discharging rate of a MU is elevated and happens in an instantaneous manner before it declines afterwards. During slow ramp contractions, maximum discharging rates between 20–50 Hz are usually observed. On the other hand, during fast contractions, more elevated frequencies (greater than 100 Hz), though momentarily, can be attained [38, 42].

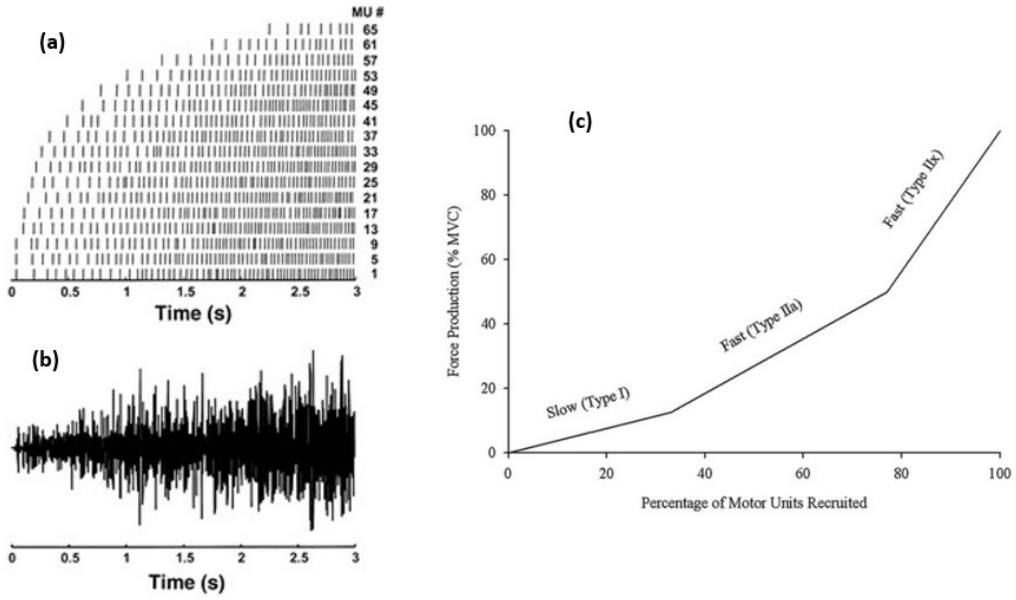

Figure 1.9: Example of: (a) MU recruitment pattern exhibiting the firing discharge of 65 MUs and (b) the generated single differential signal following the recruitment pattern, (c) the orderly recruitment of MUs (slow and fast) during the voluntary activation of a skeletal muscle. Edited from [40,43] .

As a sum up, the force that a muscle can produce over most of its operating range is manipulated by coexisting changes in MU recruitment and rate coding. How much each of the two processes contributes throughout this operating range is variable whatsoever. It was earlier shown that the most contributing process at low forces is the recruitment, whereas the rate coding is more influencing in higher muscle forces [44]. It is noteworthy to mention that the recruitment pattern

considered in the muscle model used in this thesis relies on the size principle to describe isometric contractions.

1.2.3 Physiology of skeletal muscle contraction: electrical and mechanical events

As mentioned previously, the communication between the neuron and the muscle happens chemically through the ACh. As a matter of fact, upon reaching the ends of the axon, the nerve action potential will cause the opening of voltage gated Ca^{2+} channels allowing the transfer of Ca^{2+} into the axon terminal. The presence of Ca^{2+} will in turn trigger the releasing of the ACh form their vesicles in the axon terminals. Those neurotransmitters will then travel across the synaptic cleft to settle on their receptors found on the junctional folds of the sarcolemma. Once ACh molecules bind to their receptors, a series of electrical incidents will be triggered [4]. On a side note, to prevent the non-stop muscle contraction in the absence of a nerve impulse, the ACh is disabled by an enzyme present in the synaptic cleft (**acetylcholinesterase**), which decomposes ACh into its basic units (acetic acid and choline). This will abort the contract causing influence of ACh. Before explaining how those electrical events occur, it is noteworthy to mention that the sarcolemma, like any cellular plasma membrane, has a definite polarity. This is due to the difference in the potential between its inside and its outside. In fact, at rest, the inside of this membrane is negative with a potential of around -90mV (this difference in potential exists due to the various concentrations of sodium (Na^+), potassium (K^+), and chloride (Cl^-) and other ions across the membrane) when compared to the outside [4]. Accordingly, the binding of ACh molecules to their receptors allows the opening of chemical ion channels. This will permit the influx of Na^+ to the inside on the muscle fiber. Also, K^+ are allowed to outflow to the outside of the muscle fiber. But since the amount of Na^+ ions entering in is much more than the amount of K^+ exiting the muscle fiber, a temporary change in the polarization inside of the sarcolemma will

occur, where it will become more positive. This is known as **depolarization** and is also termed the **end plate potential**. This is depicted in Figure 1.10(a) [8]. When this endplate potential extends to neighboring membrane regions, more sodium channels will tend to open allowing more influx of sodium ions. This will cause the further depolarization of the membrane voltage (to around 30mV) as shown in Figure 1.10(d). As soon as a certain membrane voltage threshold is targeted, what is known as an **action potential (AP)** originates as shown in Figure 1.10(b) [8]. This AP then propagates along the sarcolemma of the muscle fiber in both directions at a velocity between 2 and 6m/s with an amplitude of around 100mV [4]. The following described events constitute phase 1 of muscle contraction which is schematized in Figure 1.11. Keep in mind that the wave of depolarization is always followed by a wave of **repolarization** which is initiated first by the closure of the Na+ channels and the opening of the K^+ channels (Figure 1.10(c)) and second by the excessive outflow of K^+.

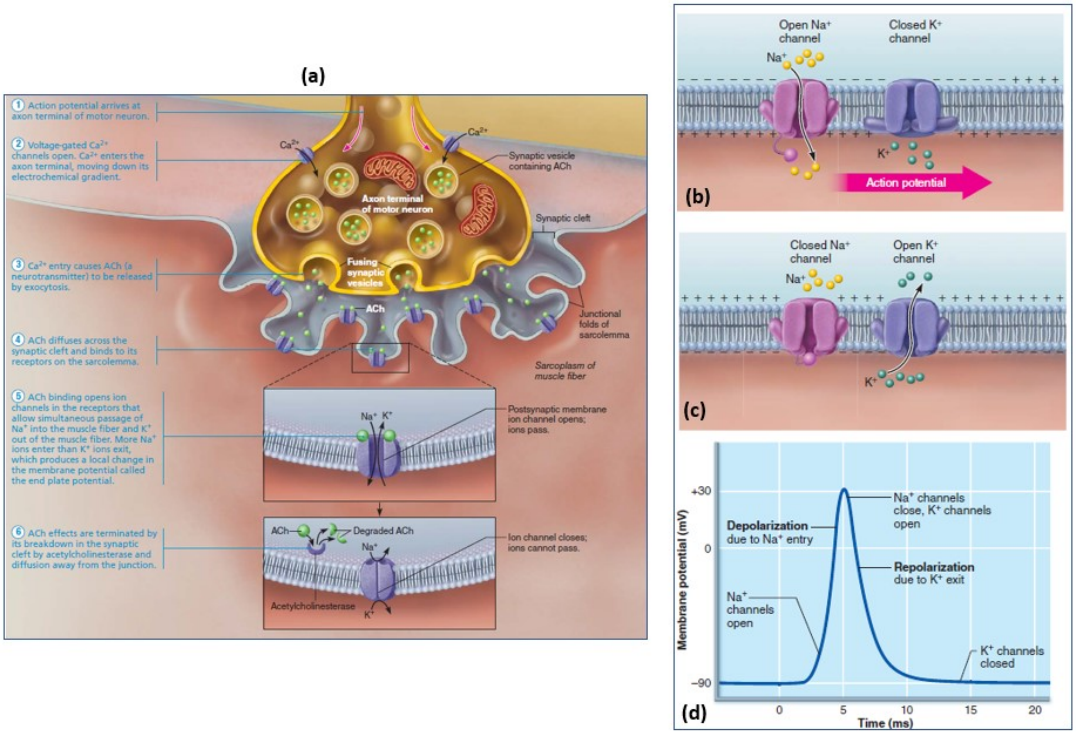

Figure 1.10: (a) The events at the neuromuscular junction, (b) the depolarization, (c) the repolarization, and (d) the action potential and associated ionic channels opening and closing [4].

This causes the return of the membrane potential to its resting status. For a certain period, during repolarization, the excitability of the muscle fiber membrane is reduced, and this membrane is said to be in a **refractory state**, hindering the muscle cell from being restimulated until repolarization is over [8].

Following this, phase 2 (Figure 1.11), which includes the excitation-contraction coupling, is initiated due to the propagation of the AP. A series of chemical and mechanical events occur during this phase and those are depicted in Figure 1.12.

First, upon the propagation of the AP, it penetrates down the T tubules in the sarcolemma. In those tubules, certain voltage-sensitive proteins exist. The arrival of the AP to those structures will cause a change in their shape. Accordingly, this will result in the opening of Ca^{2+} liberating channels in the SR and the Ca^{2+} will thus be released into the cytosol.

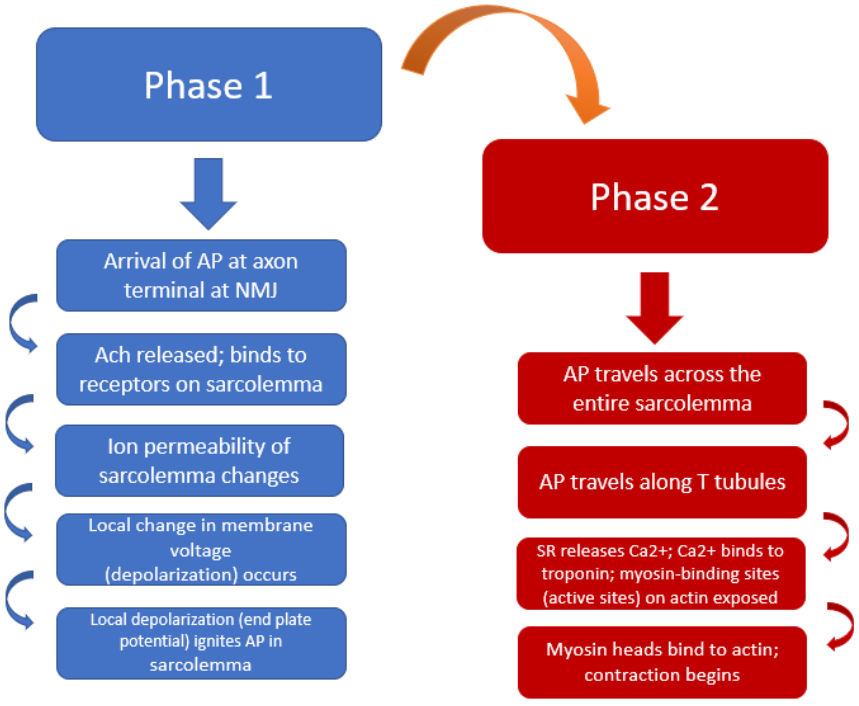

Figure 1.11: The two phases of events causing the contraction of muscle fiber. Recreated from [4].

Consequently, this will trigger a popular mechanical event know as **cross-bridge cycling** which will result in the muscle contraction. Initially, the myosin binding sites on the actin are blocked due to the presence of the tropomyosin molecules. When enough Ca^{2+} bind to troponin (on the actin part of myofibril), its shape will be altered, and it will force the tropomyosin to change location and move away from the binding sites of myosin (Figure 1.12).

Hence, the exposure of the myosin binding sites allows myosin to bind to the actin forming a cross bridge, which acts as a force-producing sites causing what it known as the sliding filament phenomenon. This will initiate the contraction cycle which will last as long troponin is not blocking the active sites on the actin [4].

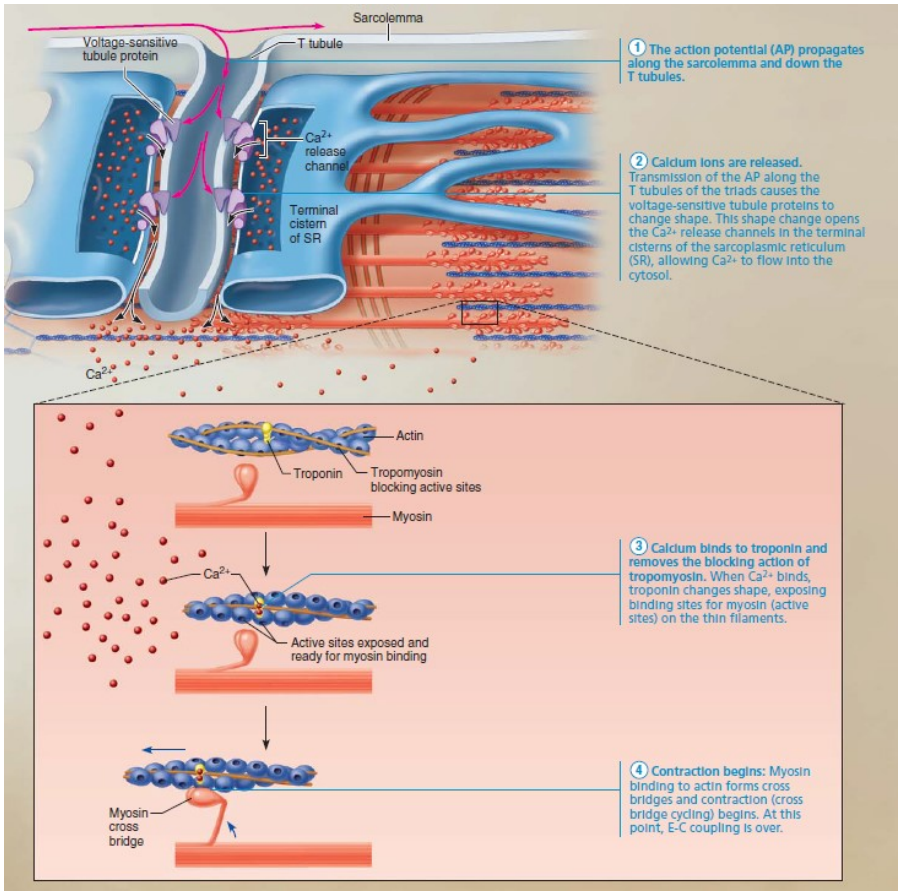

Figure 1.12: Events leading to the formation of a cross-bridge [4].

The steps of the contraction cycle are illustrated in Figure 1.13. Following the formation of the cross-bridge, **Adenosine diphosphate (ADP)** and **phosphate** will be released. This will produce the force needed by the myosin head to pull the actin filament towards the M line, forcing the overlapping of the thick and thin filaments. After that, the cross-bridge detachment takes place in the presence of **Adenosine triphosphate (ATP)**, which binds to their sites at the top of the myosin. In the presence of ATPase enzymes, the hydrolysis of the ATP to ADP will be facilitated. This will cause the breaking of the cross-bridge and the return of the myosin head to its initial position prior to the formation of the cross bridge. This cycle will repeat itself if enough calcium and ATP are still present.

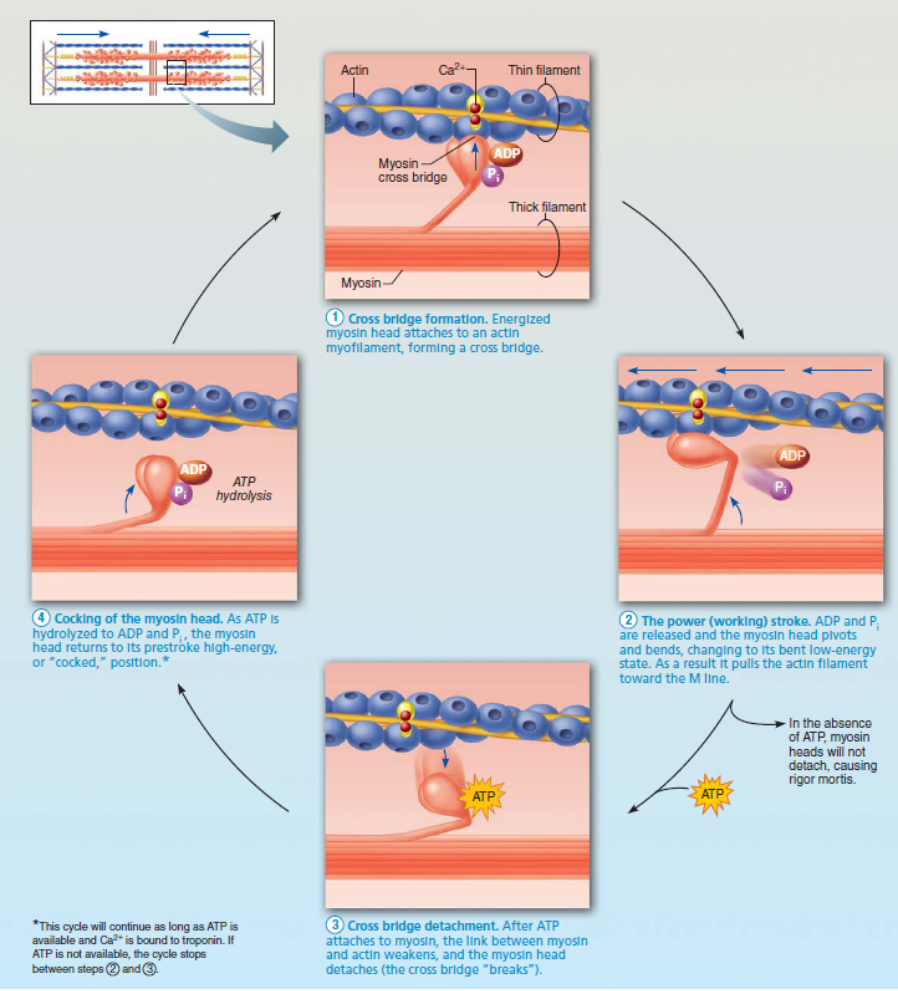

Figure 1.13: The cross-bridge cycle [4].

1.3 Spatial activation of MU and muscle diseases

Gaining a more detailed insight about the spatial activation of MUs is of a great interest and plays an essential role in numerous applications. Indeed, estimating the spatial activation of MUs during certain diseases, such as Duchenne muscular dystrophy, is crucial for usage in controlling robotic exoskeletons [12]. Moreover, spatial activation of MU is of a great interest during neuro-rehabilitation applications, where it was shown that certain alterations in muscle activation patterns in major leg muscles existed during walking with the assist of a robot. In fact, studies have shown that by limiting the degrees of freedom of the motion of the leg and pelvis with the assist of a robot, a change in the naturally happening muscle activation patterns will take place [13]. Moreover, normal muscle activity patterns in lower extremities were found to be altered post-stroke and thus affecting the gait of a person (hemiparetic gait) [14]. Furthermore, the analysis of the change in the spatial distribution during prolonged contraction may play a role in the controlling strategies of the neuromuscular system. In addition, information about the muscle status can be known from the spatial reorganization of muscle. For example, it was shown that in a masseter muscle, a unilateral painful stimulation can result in a spatial redistribution in such muscles [15]. Equally important, it has been shown that certain muscular diseases are associated with a change in the spatial activation of MUs. Thus, knowing the spatial activation of MUs in certain muscles will enable the diagnosis of those muscular diseases. Even for healthy muscles, a commonly occurring muscle performance degradation is related to **muscle fatigue**. It has been shown that localized muscle fatigue affects and changes the spatial activations patterns of muscles. Specifically, Falla et. al proved that, because of fatigue, the barycenter of the muscle activation patterns is shifting in certain upper and lower limb regions [45]. This mechanism will allow the muscle to have prolonged tolerance and hence varying the

load on the active muscle fibers thus preventing the over exhaustion of the muscle. Similarly, the recording of surface muscle signals in upper trapezius muscle was done by Farina et al. who noticed a transformation in the spatial distribution of the muscular activity as a mean for providing extended muscle contractions [46].

As a matter of fact, when it comes to mapping the muscular spatial activity, different medical imaging methods were involved. For instance, using **magnetic resonance imaging (MRI)**, Mariappan et al. were able to locate certain muscular regions in the hands and explored that muscle regions are grouped according to their function [47]. On the other hand, certain muscular characteristics were measured in a dynamic manner when Sofia et al. used the **ultrasound (US) imaging** [48]. It was found that depending on the amount of force generated due to the finger extension, certain muscle patterns were formed in the forearm extensor. Whatsoever, the MRI technique does not allow viewing the neuromuscular spatial activation in dynamic conditions, while the muscle is generating force for instance. Meanwhile, US imaging has the limitation of only being able to measure low muscular activity [46]. To come around this problem, the introduction of multi-channel surface electromyography (sEMG), which will be introduced in the next section, enabled the extraction of a vast deal of information regarding the spatial activation of muscles.

1.4 High density surface electromyography (HD-sEMG) and decomposition

An inherent characteristic of an electromyographic (EMG) signal is collectiveness. In other words, an EMG is considered as an interference signal which is composed of the superposition or algebraic summation of motor unit action potentials (MUAPs) trains generated from various active motor units (as portrayed in Figure 1.14) [49, 50].

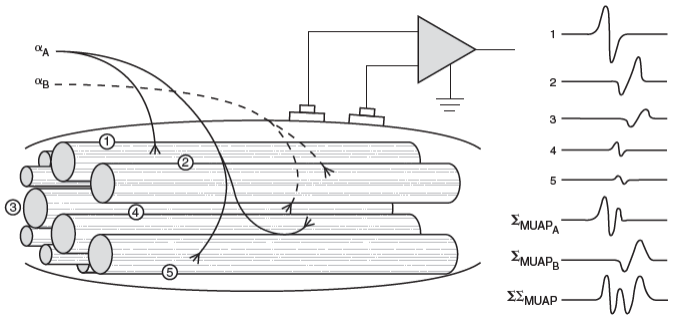

Figure 1.14: Superposition of MUAPs to form the surface EMG signal [8].

When it comes to the measurement of those signals there are two choices: either the invasive intramuscular (indwelling) EMG recording technique or the non-invasive surface EMG one. In the former, a needle or a fine-wire electrode is inserted into the muscle to study the muscular activity of only a few fibers thus providing a way to evaluate the MUs individually since only a few active fibers will be near the measuring electrodes. Meanwhile, in the latter method, a single pair of electrodes placed on the surface of the skin (bipolar EMG) are utilized to measure the muscular activity. This is known as single channel surface EMG. However, in this technique the number of active sites is numerous and thus the superposition of MUAPs will occur to a large extent making this technique earn the trait of low spatial selectivity. Moreover, since the electrodes are placed non-invasively on the surface of the skin, the volume conductor low pass filtering effects of the underlying tissues that the signal passes through to get to the electrode are inevitable. This makes it harder to distinguish between different MUAPs from different MUs [51, 52, 53, 54]. However, even though the invasive EMG measurement offers high selectivity, this technique has an obvious innate disadvantage which is due to the invasive nature of this technique (patient discomfort and pain, high possibility of infection and disease spread, etc. [53, 55]). Moreover, those methods endure the trouble of handling MUAPs that are superimposed in time, the thing that commonly occurs for high contractions force [56, 57]. To overcome the

limitations associated with surface and indwelling EMG signals, a recent high density (multi-channel) surface EMG (**HD-sEMG**) technology which employs multiple closely-packed electrode grids or arrays [58, 59] was introduced as shown in Figure 1.15.

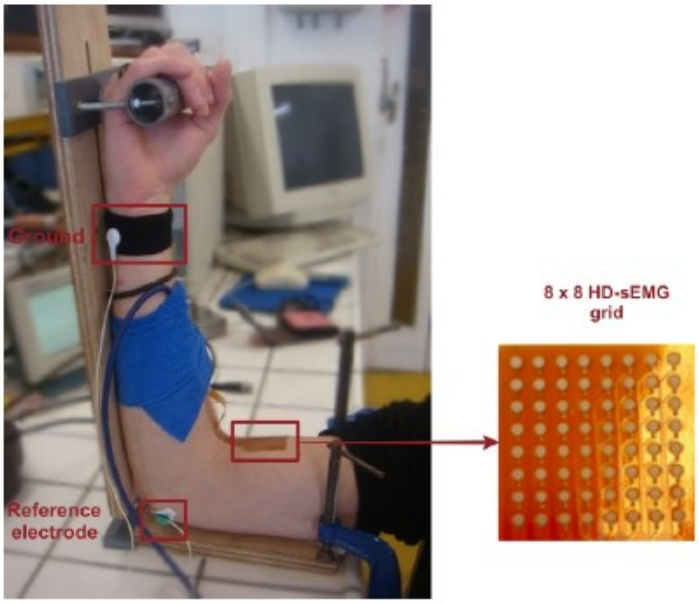

Figure 1.15: A HD-sEMG electrode grid positioned on the biceps brachii (BB) [60].

This technique allows to monitor both the time variation as well as the spatial information of the EMG signal, hence increasing the potential to explore further muscle traits by enhancing the resolution. In particular, the detection of single MU characteristics was made possible due to this emerging measurement method. This is owed to the introduction of the new spatiotemporal aspects of the MU. To date, this technique has been incorporated in several clinical applications such as fatigue studies, neurogenic changes, myopathies, etc. [61].

Researchers have tried to apply several algorithms on those HD-sEMG signals to further explore detailed information about the MU recruitment schemes. Among those algorithms, there is the **decomposition approach**. The EMG decomposition is a procedure which includes subdividing the EMG signal composed from multiple motor units into its constituents; the individual

contribution of each motor unit action potential (MUAP) train [52, 53, 51]. While decomposition can provide valuable information regarding the individual MU discharging times it is not capable to identify the exact spatial distribution of the MU that produced a definite MUAP [57, 58, 59, 62]. Hence, there was a need for a method which effectively enables the spatial localization of active regions of variable force levels within the muscle. However, a significant application for decomposition is that it can be used as a preprocessing screening technique that involves denoising or filtering the EMG signal (excluding the effect of muscle cross talk for instance) and extracting the individual contributing sources (a region of interest) prior to the application of the source localization techniques [63, 64, 65, 66].

1.5 The forward and inverse EMG problem

When it comes to electrophysiological signals, such as EMG signals, it is of great interest to investigate information regarding the origin of those signals. Such information includes the positioning and location of the active sources inside the muscle during a definite task, which is known as EMG **source localization**. This area of research has gained elevated attention due to the vast field of applications it offers. Those applications include, but not limited to, a better diagnosis of neuromuscular diseases, guidance in rehabilitation, and prosthetic control. Certain signal processing techniques, termed the **forward and inverse problem**, are applied on surface EMG (sEMG) signals for the purpose of the estimation of the location of active sources. This process includes obtaining the surface potentials resulting from the active sources within the muscles (**the forward problem**), and for this to be achieved a volume conductor muscle model for potential generation must be available. This is successively followed by the estimation of the location of the sources resulting from the surface muscle measurements (**the inverse problem**). The following approach is depicted in Figure 1.16.

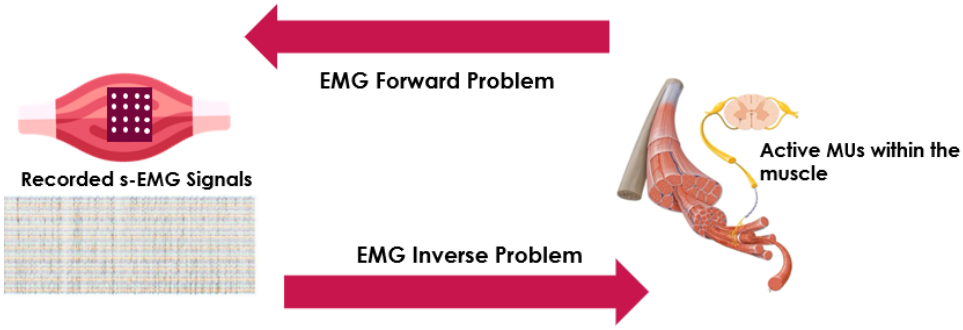

Figure 1.16: An illustration of the forward and inverse problem.

1.5.1 sEMG forward models

Compared to electroencephalography (EEG) and electrocardiography (ECG), the forward and inverse problems have been less tackled when dealing with surface EMG signals. Regardless of this fact, and since those three signals share a similar electrophysiological foundation, the studies that have been done on EEG and ECG signals can be helpful and can be applied when dealing with sEMG signals with the proper modification and fitting. The sEMG signal is produced because of the electrical activity of the activated muscle fibers when a contraction occurs. Hence, the depolarized zones of the muscle fibers, agglomerated as MUs, are considered to be the signal/current sources [67]. Those current sources are separated from the recording electrodes by biological tissue. This is what is known as volume conduction and could be described as the flow and conduction of the electrical signal across the biological tissue and measuring the signal at a distance from the sources. Current flow from bioelectric sources across a volume conductor produces small potential differences on the body surface [68]. The representation of the current sources varied from monopoles to dipoles and even to multipoles. For simplification, the choice of the primary current sources will be restricted to current dipoles, because more complex models can be formulated as sums or integrals of these basic sources. Moreover, more attention is given to dipole models than monopole or multipole models, since dipoles provide a stronger physical and physiological explanation of the nature of current sources

and thus can be considered as a discrete representation of those current densities [69]. A useful approach to the calculation of those electric potentials (solving the forward problem) is to relate them to the charge density that gives rise to them. This particular electric behavior of the volume conductor, i.e. the relationship between the potentials at the surface and the current sources within the volume conductor, is provided by Poisson's equation which is derived by the divergence operator [70]. First of all we would start by defining the current density ***J****(x,y,z)* as a vector field whose unit is A/m^2. Now let the divergence of ***J*** be termed $\boldsymbol{I_m}$ (A/m^3) which is the current source density (Equation 1.1):

$$\nabla \cdot J = I_m \tag{1.1}$$

The current density **J** is related to the electric field **E** (V/m) by Ohm's law (Equation 1.2):

$$J = \sigma E \tag{1.2}$$

where $\boldsymbol{\sigma}$ is the conductivity tensor (S/m). Additionally, in accordance with previous studies, the EMG models have been shown to satisfy the conditions of quasi-stationarity, which means that the inductive and capacitive effects of the volume conductor can be ignored, and the volume conductor is purely resistive. Accordingly, neglecting the magnetic induction in Faraday's law makes $(\nabla \times \boldsymbol{E} = 0)$ it possible to introduce the scalar potential field ϕ with volts as its unit and the electric field can then be related to the potential field as indicated in Equation 1.3:

$$E = -\nabla\phi \tag{1.3}$$

Now by combining Equations 1.1, 1.2, and 1.3 we can get the general form of Poisson's equation (Equation 1.4):

$$\nabla \cdot \big(\sigma \nabla(\phi)\big) = -I_m \tag{1.4}$$

The solution of Equation 1.4 allows us to obtain the potential at any point in space when $\boldsymbol{I}$ and $\boldsymbol{\sigma}$ are known. In addition, the potential needs to satisfy certain boundary conditions which describe the continuity of the potential at interfaces. There exist two boundary conditions which are termed the Neumann and Dirichlet boundary conditions [71].The sEMG forward problem consists of finding surface signals arising from myoelectric currents in the muscle. Throughout history, various muscle models have been adopted in order to simulate the potential distribution at the surface of the skin. Table 1.2 lists the evolution of those models and Figure 1.17 shows a number of those adopted models.

Table 1.2: A group of the volume conductor models used in solving the forward problem using sEMG signals.

Author	Description of Model
Heringa et al. [72]	Single cylinder consisting of a muscle layer
Gootzen (1989) [73, 74]	Eccentric bioelectric source in a finite, anisotropic cylindrical volume conductor consisting of two layers (muscle tissue & subcutaneous fat)
Roeleveld (1997) [75]	An anisotropic cylindrical volume conductor consisting of three layers; a layer of skin and a layer of subcutaneous fat around muscle tissue
Farina et. al (1999) [76]	Four- layer medium surrounded with air; nonhomogeneous (layered), anisotropic volume conductor model constituted by muscle (anisotropic), fat (isotropic), and skin (isotropic) layers
Blok (2002) [77]	Eccentric bioelectric source in a finite, cylindrical, and anisotropic volume conductor consisting of three layers, representing muscle, subcutaneous fat, and skin tissue.
Lowery (2002) [78]	4 components model (bone, muscle, fat, skin). Muscle was considered homogeneous and anisotropic while the fat and skin layers are isotropic.
Lowery (2004) [79]	4 components model (bone, muscle, fat, skin) based on MRI images.
Mesin & Farina (2006) [80]	2-layer model which is not space invariant; a planar layered volume conductor, comprised of fat and muscle layers with spherical inhomogeneities inside the fat layer.

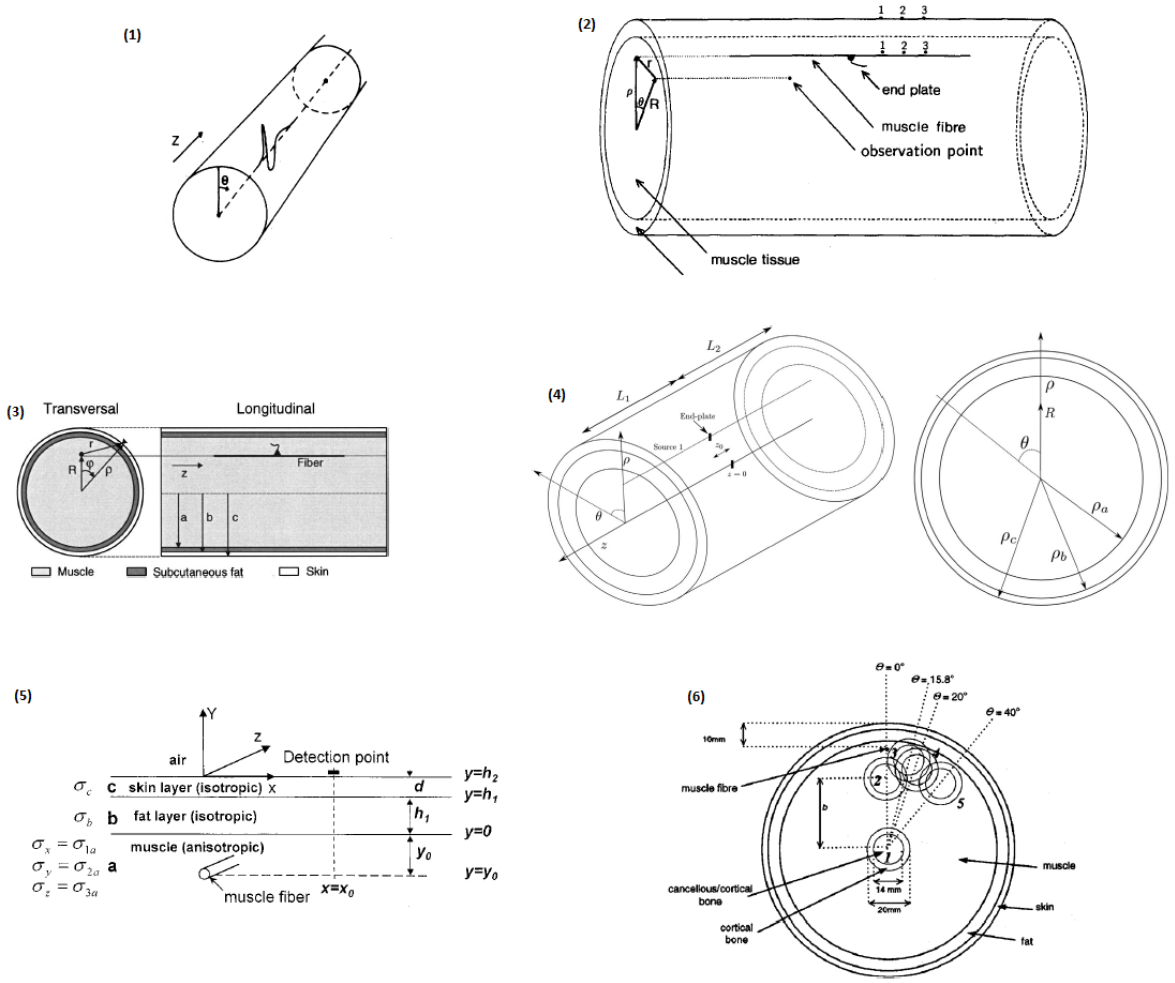

Figure 1.17: Various muscle volume conductor models adopted through history; (1) Heringa [72], (2) Gootzen [74], (3) Blok [77], (4) Carriou [23], (5) Farina [76], and (6) Lowery [78].

The majority of these models have been based on analytical solutions [73, 75, 77, 81, 82, 83, 84, 85]. Though analytical models are computationally more efficient (faster solutions), numerical solutions, such as the boundary element (BEM), finite difference (FDM) or finite element (FEM) methods, allow a better description for the complex geometry of the muscle [23]. Only a few of those models have been used in the literature [78, 79, 86]. In this thesis work, and for the purpose of gaining faster solutions, since it is one of the aims of this thesis work, our work will be done using an analytical model. A comparison between the BEM, FEM, and FDM numerical methods is included in Table 1.3.

Table 1.3: Comparison between some of the most famous numerical methods [72, 87, 88].

	BEM	**FEM**	**FDM**
Anisotropies	Inability to handle anisotropic media	Can deal with anisotropy	Can deal with anisotropy
Inhomogeneity	Cannot be managed	Can be managed	Can be managed
Computation time	Fast	Fast	More Computationally Expensive
Complexity	Not good in dealing with complex geometries.	Can deal with complex geometries.	Can deal with complex geometries.
Description of geometry	Geometry is represented using triangulated surfaces representing the domain boundaries.	Geometry is subdivided into non-overlapping tetrahedral or hexahedral elements with good approximation of the geometry while allowing boundaries to be modeled.	Composed of regular grids thus greatly simplifying mesh creation process.

1.5.2 EMG inverse methods: overdetermined vs. underdetermined methods

There are two main approaches to the inverse solution: non-parametric and parametric methods [89]. Non-parametric methods are also referred to as Distributed Source Models. Parametric Methods are also referred to as Equivalent Current Dipole Methods [69, 89, 90, 91]. In other words, parametric methods are used when we are dealing with what is known as overdetermined models, while non-parametric deal with underdetermined models (check the coming section for an explanation about the two types of models).

In this section, first, a review of the inverse problem applied on sEMG signals on both overdetermined and underdetermined models is demonstrated. In the next section, an explanation of the underlying models and methods is detailed.

a) Overdetermined discrete source models-parametric models

Equivalent current Dipole methods is a name given to a method when it is assumed the presence of only a small or limited number of current dipoles of unknown location and orientation [69, 90]. Thus, in this approach, the number of electrodes used is greater than the number of considered current sources; the system is thought to be *overdetermined*. Since the number of unknowns is less than the number of measurements on the sensors and the number of dipoles is known a priori, and since there exists a non-linear relationship between the measurements on the sensors and the dipole locations, the methods that are used to solve the inverse problem are referred to as *parametric methods* [89, 90, 91].

The most popular approach in the parametric methods is the least square approach (which is described in the coming section when deriving the minimum norm solution) which revolves around minimizing the squared error between the simulated and the actual measured potentials [91]. Other methods such as the beam forming approaches, the multiple classification algorithm (MUSIC), and RAP-MUSIC (recursive MUSIC) are some of the most popular methods for solving overdetermined problems [89, 90, 92]. However, since it is not feasible to know the current sources a priori, and since an assumption of small, fixed number is not realistic, the focus will be on the undetermined solutions.

b) Underdetermined distributed source models

Since assuming that only a discrete small numbers of sources is active when formulating the inverse problem is not close to reality, the *distributed source models* have received increased attention [22, 92]. In this type of models, no prior assumption regarding the number of sources is made and thus all possible source locations are assumed simultaneously. Consequently, the 3D volume is subdivided into many voxels or grid points and each one of those voxels is considered

to contain a separate dipole current source. Thus in this model, the number of voxels or current sources is much greater that the number of electrodes or measurement points at the surface; this is what is called an *underdetermined problem* [69, 90, 91, 93]. However, though their number is very high, but the dipole locations are fixed so this problem is a linear underdetermined problem.

The goal is then to match a configuration of values in the voxels along the 3D grid with the recorded surface potentials at the sensors. Due to the fact that in an underdetermined problem many different solutions could fit the same data, the inverse problem is known to be ill posed [22, 92, 94] and thus it is essential to apply regularization (*non-parametric methods*) so that the solution becomes stable and distinctive since by doing so variations in the data will not result in vast variations in the solution [95].

If we want to mathematically describe the model under study, a linear relationship exists between the distributed dipole sources (voxel sources) and the surface measurements, which are recorded from the electrodes (surface potentials) as follows:

$$b(t) = A * L(t) + e \tag{1.5}$$

where $\boldsymbol{b}$ is a n×1 vector which expresses the measurements of the surface signals from the electrodes (surface potentials) and n is the total number of electrodes or the total number of the measurement sites. $\boldsymbol{L(t)}$ is a p×1 vector called the voxel vector source which contains the source vectors or the current densities at each voxel or at each point in the grid (p is the total number of voxels or sources). $\boldsymbol{A}$ is a n×m matrix and is often referred to as the lead field matrix. It gives an idea about the current flow at a definite electrode through each dipole position (it expresses the sensor array sensitivity for a source located at a definite voxel and directed in the x, y, and z directions) [25, 89, 90, 92, 96]. In general, a noise matrix is added to the sensor data.

Now, the inverse problem is to find an estimated current density $\hat{\boldsymbol{L}}$ of the dipole given the surface recording at the different sensor locations $\boldsymbol{b}$ and the lead field matrix $\boldsymbol{A}$ which is calculated in the forward problem using an analytical model or numerical computations [89, 96].

Minimum norm estimation method (Non-Parametric Methods of Source Localization)

In 1884, Hamalainen and Illmonemi proposed the minimum norm as a solution for the inverse problem of distributed source models with no use of any a priori information [92]. The minimum norm approach is actually a special case of the Bayesian formulation with the assumption that the posterior distribution of $\boldsymbol{l}$ to be a Gaussian distribution [69, 89, 90].

For the derivation of the minimum norm solution, we start with the maximum likelihood principle (note that in the discussion below the time notation is removed for the sake of simplicity). It is assumed that the noise has a Gaussian distribution (zero mean and same variance), and it is given by Equation 1.6:

$$p(e) = \frac{1}{(2\pi\sigma^2)^{M/2}} exp\left[-\frac{1}{2\pi\sigma^2}\|e\|^2\right] \tag{1.6}$$

Accordingly, due to the linearity of the system as implicated in Equation 1.5 then the probability distribution of the output data $\boldsymbol{b}$ on the sensor can be derived as indicated in Equation 1.7:

$$p(b) = \frac{1}{(2\pi\sigma^2)^{M/2}} exp\left[-\frac{1}{2\pi\sigma^2}\|b - Al\|^2\right] \tag{1.7}$$

Now we can say that the likelihood function is $\boldsymbol{p(b)}$ and that it is a function of the unknown current densities $\boldsymbol{l}$. To find an estimate of the current densities $\boldsymbol{l}$, the output $\boldsymbol{b}$ is considered the result of the most likely events. So what is required is to find $\boldsymbol{l}$ as such to maximize the likelihood function $\boldsymbol{p(b)}$ of having the observed data $\boldsymbol{b}$ on the sensor output [96]. Therefore, the maximum likelihood estimate $\hat{\boldsymbol{l}}$ is yielded as described in Equation 1.8:

$$\hat{l} = arg\,\max_{l}\ log\ p(b) \tag{1.8}$$

where ***log p(b)*** is the log-likelihood function and using Equation 1.7 the log of ***p(b)*** will become (***S*** is the remaining terms in the equation that are independent of ***l***):

$$log\,p(b) = -\frac{1}{2\pi\sigma^2}\|b - Al\|^2 + S \tag{1.9}$$

From Equation 1.9 we can infer that the ***l*** required to maximize log ***p(b)*** is the ***l*** which is needed to minimize a function ***F(l)*** which is defined as follows [89, 90, 96]:

$$F(l) = \|b - Al\|^2 \tag{1.10}$$

Consequently, the maximum likelihood estimate $\hat{\boldsymbol{l}}$ is then yielded by the "least square" minimization of the function ***F(l)*** (minimize the squared error between the output data ***b*** and the lead fields ***A*** which are computed from the forward model [91]). This is known as the least squared method:

$$\hat{l} = arg\,\min_{l}\ \ F(l)\ \text{ with }\ \ F(l) = \|b - Al\|^2 \tag{1.11}$$

However, the least square method alone is not adequate when the system we are dealing with is ill-posed (p>>>n). The reason behind this is that an infinite number of ***l*** will minimize the function ***F(l)*** or make it equal to zero.

For the purpose of solving this ill-posed problem, and to give preference to a particular solution, we need to derive the minimum norm estimate [96]. This is done by including a certain constraint or regularization term in the minimization. Consequently, we need to find the solution with the smallest norm of the solution vector ***l*** to solve the optimization equation.

$$\hat{l} = arg\,\min_{l} \|l\|^2 \qquad \textit{subject to} \qquad \|b - Al\|^2 = d \tag{1.12}$$

In the MNE method, the L_2 norm or the Euclidean norm ($\|\,.\,\|^2$ is the L_2 norm, and $\boldsymbol{d}$ is a constant) is usually used to regularize this estimation. Since in Equation 1.12 we have an equality-constraint, then by the aid of the Lagrange multiplier $\boldsymbol{\lambda}$, whose role is to change a constrained optimization problem into an un-constrained one, we can say that the solution of Equation 1.13 is referred to as the L2- regularized minimum norm solution.

$$\hat{l}_{MNE} = A^T(AA^T + \alpha I)^{-1}b \tag{1.13}$$

where $\boldsymbol{\alpha} = \frac{\mathbf{1}}{\boldsymbol{\lambda}}$ and $\boldsymbol{I}$ is an identity matrix. Now from Equation 1.13 we can say that this method chooses among all the possible solutions the 3D current distribution that has the lowest energy or the smallest L_2 norm [69, 91, 95]. This is also known as the Tikhnonov regularization where $\boldsymbol{\alpha I}$ is said to be the Tikhonov matrix Γ (in the L_2 regularization which gives preference to smaller norms the Tikhonov matrix Γ is chosen to be a multiple of the identity matrix $\Gamma = \boldsymbol{\alpha I}$).

The minimum norm method is more effective with superficial sources which are characterized, due to their closeness to the sensors, by a minimum energy but strongest fields (due to their proximity, those require less energy to reach the surface but have the highest amplitudes). Hence this technique has more difficulty to detect deep sources although it is known to provide satisfying results in terms of resolution [92].

A main drawback of the MN approach is that the resulting solutions tend to be overly smooth and widespread beyond the extent of the underlying sources [69]. To overcome the depth limitation of this method and to improve the performance of the minimum norm, variations of the minimum norm method were introduced.

Weighted minimum norm (WMN) Solution

The Weighted minimum norm method mitigates the issue of favoring small and superficial sources by using a weighting matrix ***W*** (depth weighting).

$$\hat{l}_{wMNE} = (W^T W)^{-1} A^T (A(W^T W)^{-1} A^T + \alpha I)^{-1} b \quad (1.14)$$

Several forms of the weighting matrix can be taken [97] but the simplest one as introduced by Lawson & Hanson in 1974 [98] is constructed on the basis of the norm of the columns of the lead field matrix ***A*** [69, 89, 91].

In this case ***W*** is a p×p diagonal weighting matrix with non-zero entries; ***W***= $(1/\|g_1\|, 1/\|g_2\|, 1/\|g_3\|, \ldots, 1/\|g_p\|)$, where $\|g_i\|$ is the Euclidian norm of the i'th column of ***A***. By doing so, deep sources are taken into consideration now and superficial sources are favored when ***W*** is chosen to be the identity matrix (***W=I***).

Low-resolution Electromagnetic Tomography (LORETA)

Presented by Pascual-Marqui in 1994 [92], the LORETA method it incorporates the second-order spatial derivative Laplacian operator ***B*** with the lead field normalization.

This method minimizes the Laplacian of the weighted sources giving the same chance for superficial as well as deep sources to be reconstructed.

$$\hat{l}_{LOR} = (B\Delta^T \Delta B)^{-1} A^T (A(B\Delta^T \Delta B)^{-1} A^T + \alpha I)^{-1} b \quad (1.15)$$

In Equation 1.15, ***B*** is the Laplacian, Δ is the delta operator, and ***A*** is the lead field matrix. By doing this, we ensure the maximum smoothness of the solution; the solution which has a smooth spatial distribution is yielded.

However, though this method gives smooth and enhanced localization for deeper sources with decreased localization errors, LORETA has the disadvantage of producing low spatial resolution (not appropriate for the estimation of focal sources) and blurred or over-smoothed solutions [69, 89, 91, 97].

Standardized LORETA (sLORETA)

Even though this method might seem like an adjustment of LORETA, the two methods are not the same since this method does not use the Laplacian operator. In fact, sLORETA is founded on the standardization of the current densities.

This method outstands in the sense that it yields exactly zero localization errors in a noise free simulation and the least localization error in noisy simulations regardless from the fact that the results are blurry [89].

If the estimates of the current densities $\hat{l}$ are given by the minimum norm approach, the variance, which is supposed to be because of both the variance of the actual signal S_l and the variance of the noisy measured signals $\mathbf{S_b^{noise}} = \boldsymbol{\alpha}\mathbf{I}$, is standardized. Taking $\boldsymbol{T} = \boldsymbol{A^T}[\boldsymbol{AA^T} + \boldsymbol{\alpha I}]^{-1}$, then the electric potential variance $\boldsymbol{S_b} = \boldsymbol{AS_lA^T} + \boldsymbol{S_b^{noise}}$, and the variance of the estimated current densities can be expressed as $\boldsymbol{S_{\hat{l}}} = \boldsymbol{TS_bT^T} = \boldsymbol{A^T}[\boldsymbol{AA^T} + \boldsymbol{\alpha I}]^{-1}\boldsymbol{A}$.

Then sLORETA provides the estimates of the standardized current densities [92] by:

$$\hat{l}_h^T\{[S_{\hat{l}}]_{hh}\}^{-1}\hat{l}_z^T \tag{1.16}$$

where $\boldsymbol{\hat{l}_z^T}$ is the current density estimate at the hth voxel offered by the minimum norm estimate and $[\boldsymbol{S_{\hat{l}}}]_{zz}$ is the hth diagonal block of the matrix $\boldsymbol{S_{\hat{l}}}$.

FOCUSS (Focal underdetermined system solution)

Proposed by Gorodnitsky el al. in 1995 [91], this technique which iteratively gives an updated form of the weighting matrix from the result or solution of the previous iteration can be referred to as the "iteratively reweighted minimum norm approach" [89, 90, 91, 92]. Consequently, this method which has the nature of being recursive, can give focal resolution to the minimum norm estimators and for this reason FOCUSS is famous for giving solutions with high resolution (unlike LORETA). This algorithm is initiated by giving an estimate l(0) using the weighted minimum norm solution $\hat{\boldsymbol{l}}_{\boldsymbol{wMNE}}$ [92]. In each of the following steps afterwards, a new separate matrix is formed and the solution is updated with the new weighting matrix [89] using:

$$\hat{l}_{FOCUSSi} = W_i W^T A^T (A W_i W^T A^T + \alpha I)^{-1} b \tag{1.17}$$

The weight matrix in the next iteration $\boldsymbol{W_i}$ can be calculated by multiplying the weighting matrix from the previous step $\boldsymbol{W_{i-1}}$ by $\boldsymbol{w_i}$ where $\boldsymbol{w_i}$ can be constructed by taking its "diagonal elements" to be the solution of the previous iteration (diag(l_{i-1})) [92, 97]. This can be noticed from the matrix below where its diagonal elements correspond to the current elements. This will give, as stated earlier, the updated form of the weighting matrix from the solution of the previous iteration.

$$w_i = \begin{matrix} l_{1i-1} & \dots & 0 \\ \dots & \dots & \dots \\ 0 & \dots & l_{pi-1} \end{matrix} \tag{1.18}$$

where i is used to index the number of iterations, $\boldsymbol{l_{ji-1}}$ denotes the j_{th} element (j=1,2…, p) of the vector $\boldsymbol{l}$ at the (i-1) iteration. Compared to MNE, the accuracy of localization is enhanced in this method. However, deeper sources are not treated fairly. To solve this problem, FOCUSS was combined with LORETA (since it provides depth localization) instead of MNE. This is the same

as the method just explained above, but the initiation is done with $\hat{\boldsymbol{I}}_{\boldsymbol{LOR}}$ and then iteration of the weighting matrix.

However, this hybrid approach was found to have increased computational complexity as well as the probability of loss of data due to its iterative nature [89, 92]. A comparison between the different inverse methods is listed in Table 1.4. In this thesis work, only the non-iterative inverse methods will be put under test, since those methods are not time consuming and since time is a priority in this work.

Table 1.4: Comparison of the explained inverse problem methods [89,92].

Method	**Characteristics**
Minimum Norm Solution	Gives preliminary current density estimations with good resolutions but favors only superficial sources and denies deeper ones.
Weighted Minimum Norm Solution	Exhibits high localization ability for deeper sources depending on the chosen weight.
LORETA	Provides enhanced localization of deep sources but results in a low resolution and blurry localization.
FOCUSS	Offers high resolution localization but does not address depth and is computationally expensive due to iterations.
FOCUSS with LORETA	Compensates for the loss of depth with keeping a high resolution but has high computational needs.
sLORETA	Provides an exact zero error in localization but results are blurry.

Before starting with the inverse problem, with a focus to spatial localization, and applied on sEMG signals, it is worth to mention that one can find in the literature numerous examples about

the application of the inverse problem and source localization on other electrophysiological signals; only a few will be mentioned. Among those is the study done by Diab et al. [99], where the MNE inverse problem was applied on Electrohysterogram (EHG) signals and solved numerically using a BEM in an attempt to try to localize the active sources during labor as shown in Figure 1.18.

Another more advanced work was performed on EHG signal by Zahran et al. who compared six source localization methods using a BEM uterine model [100]. As for the EEG signals, numerous works can be found in the literature. As an example, Hassan et al. were advanced in this field were they applied a comparative analysis between four popular inverse techniques as shown in Figure 1.19 [101] to localize EEG sources using a BEM brain model.

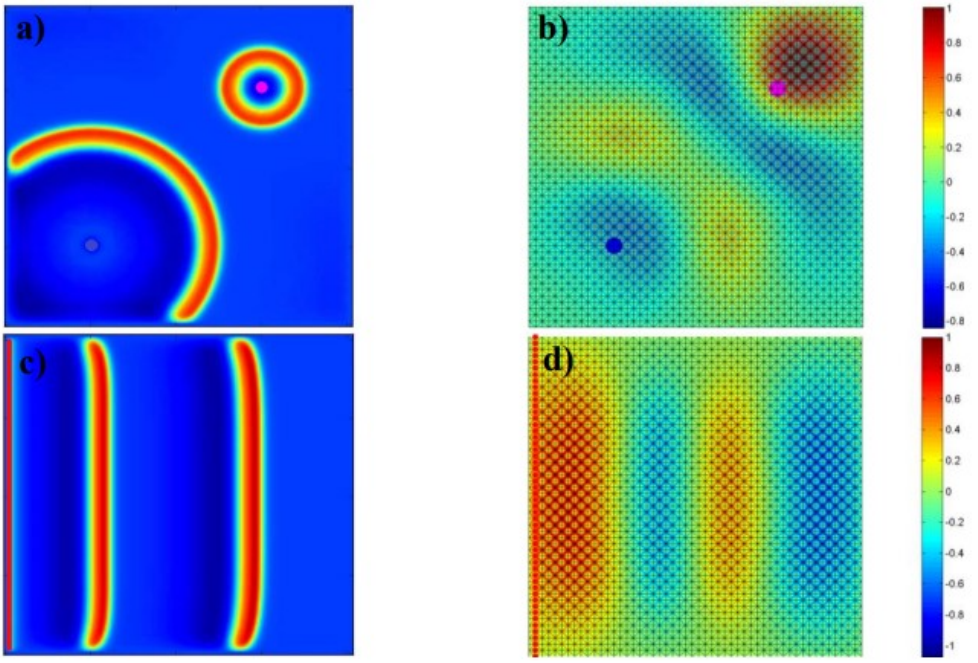

Figure 1.18: Simulation of two asynchronous sources (a) and vertical bars (c) by the electrophysiological multiscale model, and their estimated localization (b) and (d) respectively using the implemented forward/inverse tool. The blue and magenta disk in (a-b) and the red bar in (c-d) represent the position of the original source [99].

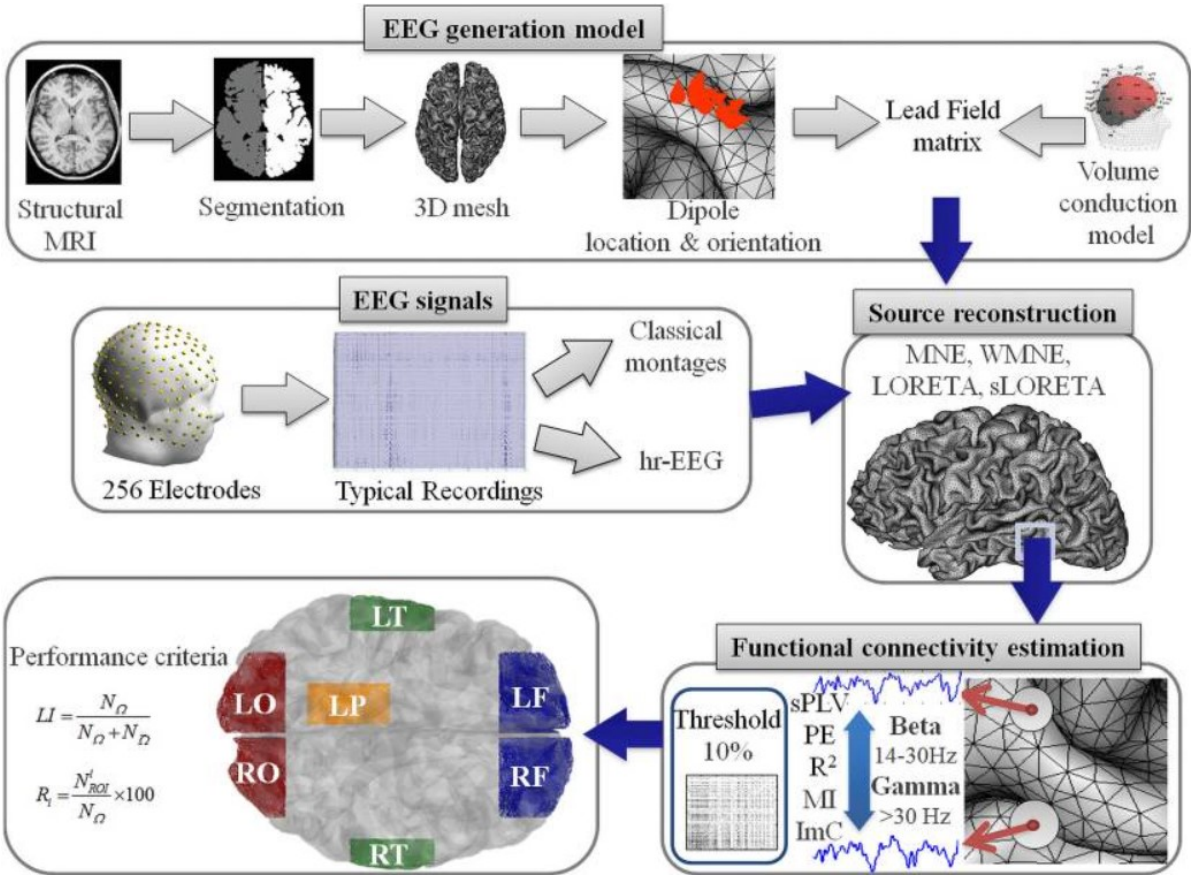

Figure 1.19: EEG source localization comparative study using : MNE: Minimum norm estimate, wMNE: Weighted Minimum norm estimate, LORETA: Low resolution Brain Electromagnetic Tomography, sLORETA Standardized Low resolution Brain Electromagnetic Tomography [101].

To our knowledge, the majority of the research in the field of the inverse problem of sEMG was done on an overdetermined discrete source model [102, 103, 104, 105, 106, 107, 108, 109, 110].

This later paved the way to the more realistic undetermined source models. As a matter of fact, recently, the focus is on solving the inverse problem of underdetermined distributed source models [20, 22, 64, 93, 95, 111, 112]. Table 1.5 includes a summary of the review on the application of source localization methods on sEMG signals on both overdetermined and underdetermined models.

Table 1.5: Summary of different techniques for solution of sEMG inverse problem.

Overdetermined Inverse Problem		**Underdetermined Inverse Problem**	
Author	**Description of Method**	**Author**	**Description of Method**
Gydikov et al. (1972) [102]	-Localization of a single motor unit using a simple volume conductor model	Van Den Doel et al. (2008, 2011) [95]	**CMG** (computed myography): -FEM model -Minimizing the least squares with a Tikhonov regularizer
Kosarov et al. (1974) [103]	-An extension of Gydikov (1972) with improvements (automatically determining the damping constants in the volume conductor model)	Zhang et al. (2010) [64]	**MAI** (Muscle Activity Imaging): - FEM model -Weighted minimum norm estimation algorithm
Monster & Chan (1980) [104]	-The decay of a volume conducted muscle fiber potential can be described by a power function. - Traingulating the peak to-peak amplitude of a spike to localize the origin of a single EMG spike	Wang et al. (2012) [111]	**MAI** based on Extended Kalman Filter: - FEM model -Extended Kalman Filters together with a weighted minimum norm regularizer
Jesinger & Stonick (1994) [105]	-FEM model - Localization of single current-dipole sources	Liu et al. (2014) [112]	Validation of **MAI**
Stonick et al. (1996) [107]	-FEM model -Localization of multiple current-dipole sources	Urbanek et al. (2016) [93]	**iEMG** (Imaging electromyography): -Minimum norm regulizer that smoothes only locally
Roeleveld et al. (1997) [108]	- The use of the gradient method to minimize the differences between synthetic signals and the inverse model results		
Saitou et al. (1999) [109]	- An inverse analysis is performed by exploring the depth and intensity of current sources that would make the sum of squares		

	difference between measured and calculated surface EMG potentials minimum		
Chauvet et al. (2001) [110]	-Minimization of the difference between calculated potential and observed potential by successive iterations		
Mesin (2015) [20]	Real time localization: -Minimizing the least squares with a Tikhonov regularizer		

1.5.3 Real time source localization

There has been an increased concern in establishing human-machine interfaces that are used to interpret the neural signals that participate in controlling prosthetic limbs, guiding rehabilitation processes, and assistive devices. Since MUAPs are produced prior to the generation of force by the muscle, inciting an electromechanical delay, those muscle signals can be analyzed and anticipate the motor purpose which then can be converted into an action ahead of the real movement. To fulfill this purpose, the MU spatial localization must undergo fast processing. What is meant by fast is a duration which is typically less than the electromechanical delay that is noticed at some stage in voluntary motion (which is around 100 ± 50 ms) [16]. This can be described as the **real time** processing of signals. Certain neural network techniques [16] have been proposed and applied on sEMG signals to enable the decomposition of those signals' temporal MU activation (MU firings) in real time. However, when it comes to giving spatial information about the distribution of MUs within the muscles in real time, rarely was this subject tackled. The only work found in the literature was performed by Mesin in 2015 [20] who solved

the over-determined problem of sEMG source localization to obtain the average estimation of the depth of MUs and not the depth of a single MU. Therefore, to our modest knowledge, there is a lack of a **real time source localization** technique that is capable of **accurate** spatial and temporal localization of individual active MUs within a muscle during a contraction.

1.6 Problematic and thesis objectives

One major issue in studying the musculoskeletal system is how regions within the muscle are tuned by the neural drive to accomplish several activation strategies for several motions. The objective of the current thesis project is to identify the parameters related to the motor unit (MU) recruitment scheme or the muscle region spatial activation strategies by applying inverse methods on the electromyographical data recorded from HD-sEMG grid. These approaches bear on complex formalism linked to inverse problem. The attained result is the characterization of specific MU recruitment/region activation strategies for application to fatigue monitoring and muscle aging analysis, and possible prosthetic control improvement.

Indeed, most of the work mentioned in the literature dictates a very high computational cost, using numerical approaches, the thing that prevents its usage in valuable applications that require low computational time and require fast signal processing. Among dedicated applications are the control of prosthesis and rehabilitation guidance [17, 18], where any time delays in discovering the activated regions would affect the application severely; real time or fast localization is required. Hence, the choice of both the representing source model and the technique of reconstruction must take into consideration the time factor.

Therefore, this work is devoted to providing an algorithm that enables the **accurate localization** of MUs within an analytical multi-layered cylindrical volume conductor model, to be used in

real-time sEMG applications. To accomplish this aim we will propose an innovative work which will progress in the following manner as shown in Figure 1.20:

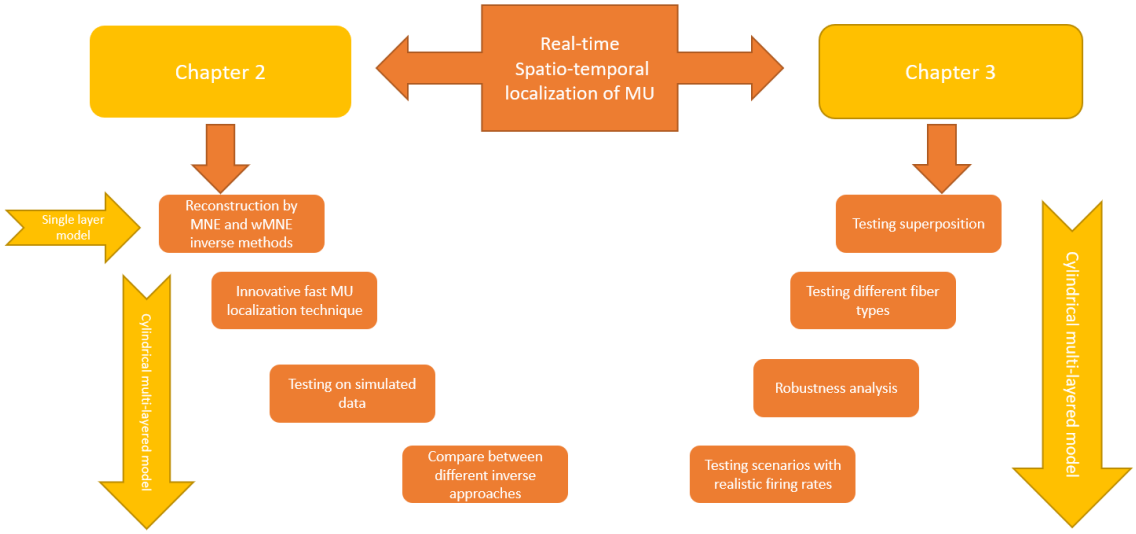

Figure 1.20: Methodology of the thesis work.

After describing the anatomical and physiological thesis context, the related methods, and the problematic and motivation behind this work, the first part of the second chapter will be initiated by a preliminary study on a simplified muscle model proposed by Dimitrov and Dimitrova [81]. This model is a simple (not realistic and composed of only a single muscle layer) but fast analytical model. It will be used in the second chapter to initially test the proposed inverse algorithms (the minimum norm and weighted minimum norm estimation), regardless of the complexity of the model. The reason why those two specific inverse methods are going to be used is that they are classical methods and do not involve iterations (thus requiring less time and are less computationally complex than other methods). One of the methods is known to be better for superficial MUs and the other for deeper ones. Therefore, this depth sensitivity will be assessed. To further investigate the actual spatial localization of the MU distribution, further analysis of the inverse problem is to be done in the last part of this chapter. The end work on the

first model will open a door for an innovative technique for predicting the spatial position of a MU within the muscle geometry based on a fitting curve created from data extracted from the inverse solution of a set of pre-defined MUs within known characteristics and locations.

The second part of the second chapter is dictated for the explanation of a more complex realistic multi-layered cylindrical model [23]. This model is an analytical model which allows the reduction of the computational time, unlike heavy numerical models. Yet, it offers accurate and realistic results. Using this model, an innovative inverse problem approach is tested. An inverse problem approach, based on the MNE method, which is tailored by using a limited number of MUs of known locations and characteristics and extracting certain information from the inverse solution (in which those MUs participated). The reason why we want the number to be limited is because as we increase the number of MUs participating in the inverse solution calculation, the processing and localization time will also increase. Therefore, we should create a tradeoff between the appropriate number of MUs capable of providing enough information for accurate source localization and between the time it takes to do so. This information is used to create a 3D fitting curve. Using this curve, if we have a random MU with an unknown location, just by knowing the surface EMG signal produced from this MU and by following the fast and simple processing steps proposed in our algorithm, we are capable of accurately and rapidly localizing MUs. In addition, a modification is done to the algorithm for it to detect deeper MUs while using MNE (no need to use two different inverse problems in this blind technique). This method will allow to accurately (root mean square error of less than 1% for the angular and depth location) localize as low as a single MU within a region in a rapid time if a computer with proper processing capabilities is used (unlike other work that localize regions of MUs [20, 64, 113]).

Following that, other inverse problem methods will be used, for comparison purpose, to evaluate classical MNE method efficiency.

This will pave way to the third chapter that aims to evaluate the robustness of the methods used. This chapter will include testing more complex muscle configurations during the localization process and checking if the proposed algorithm is capable to localize superimposed MUs firing at the same time or with small delays in between. Also, the algorithm will then be tested on a different type of MUs (like slow-twitch fiber MUs since previous tests were to be done on fast-fatigue MUs) and the results will be compared to check if the algorithm will be able to even differentiate between different MU types. Another crucial testing to be done on the algorithm is to check its sensitivity to definite instrumental or physiological changes. For this purpose, a robustness analysis will be performed in this chapter also. Finally, since the limitation that we have is the inability to validate the algorithm proposed, due to the lack of an imaging technique that allows the dynamic imaging of MUs in action at different force levels, we will try to validate by simulation. This will be done by simulating MUs at definite locations and in specific firing rates. Then the proposed algorithm will be tested to check whether it can predict the locations, thus being able to participate in specific muscle applications. It is noteworthy to re-mention that the study presented in this thesis can be considered as preliminary work to benchmark an algorithm and the main purpose of this work is to calibrate and test the algorithm before applying it to real data whenever made possible.

Chapter 2

Method Implementation

Contents

2.1 Introduction

As mentioned earlier, for the sake of computing the electromyogram (EMG) inverse problem, it is necessary to record a set of EMG measurements at the muscle surface and to use a forward model that relates those measurements to muscular electrical sources within the considered geometry [114]. Accordingly, an appropriate forward model to evaluate inverse algorithms should be capable of producing Motor Unit Action Potentials (MUAPs) which are realistic enough. Various volume conductor muscle models have been adopted to simulate the potential distribution at the surface of the skin from the activation of underlying myoelectric sources. Those models are either described analytically [73, 75, 77, 81, 82, 83, 84, 85] or numerically [23, 78, 79, 86]. Analytical models are superior over numerical ones in terms of reduction of the computational time, while the latter are used when more complex geometries are required [85]. As for the proposed methods for solving the EMG inverse problem, numerous methods have been proposed and tested [22, 64, 95, 111, 112]. However, most of those methods dictate a very high computational cost, preventing their usage in valuable applications that require low computational time. Among such methods are the control of prosthesis and rehabilitation guidance, where any time delays in discovering the activated regions would affect the application severely; real time or fast localization is required [20]. Hence, the choice of both the representing source model and the inverse problem technique must take into consideration the time factor. The main objective of the proposed methods discussed in this chapter is to provide an algorithm that enables the accurate spatial localization of MUs, combined with HD-sEMG technique, to be used in real-time EMG applications.

The aim of this chapter is to describe the inverse approaches used for localizing HD-sEMG sources as well as the models used to simulate the HD-sEMG signals. The first section describes

the preliminary study used to tune the methods and get initial feedback about the proposed inverse problem algorithms, and the model used to do so. As for the second section, a more realistic model is described, and an innovative inverse problem approach is proposed. Obtained results are then discussed.

2.2 Preliminary Study: Tuning the inverse problem algorithms

In this section, a simplified and fast single layer muscle model was employed. The purpose here is the preliminary testing of the proposed inverse algorithms regardless of the complexity of the model. Two different inverse problem formalisms, the MNE and wMNE [89] are tested and their results are presented.

2.2.1 Description of the planar generation model

In this subsection, the planar model which is going to be used in the preliminary studies, which was established by Dimitrova and Dimitrov [115], is going to be explained. Since a muscle fiber is considered as the most basic functional block of a muscle, it is reasonable to start the modelling at that level. When attempting to model the excitation source within a single muscle fiber, the concept of a dipole or a double layer source, which was first established by Wilson et al. [116] and successively advanced by Plonsey [117], seems the most convenient [118]. Hence, in the model used, the excitation sources within the fibers were modelled as lumped dipoles propagating along the axis of the fiber. Moreover, since a muscle fiber of a finite length can be viewed as a linear and time shift-invariant system, the single fiber action potential (SFAP) was calculated in a convolutional manner; only a convolution between an input signal and an impulse response (IR). The input signal is the first or second temporal derivative of the intracellular action potential (IAP), whereas IR is the potential produced at the recording electrode (supposed to be a point) by two dipoles propagating in opposite directions from the end

plates (neuromuscular junction) to the fiber ends. This is displayed in Figure 2.1, which shows a pictorial description of the innervation of a number of skeletal muscle fibers of finite length by a motor neuron (forming different neuromuscular junctions) and the propagation of a pair of dipoles (black rectangles) in opposite directions along the fiber ends at a constant velocity v, P_1 and P_2 are the two surface electrodes, x is the fiber axis, y_0 ,y_1, y_2 and y_3 are the distances from: the muscle fiber axis, the end plate region, and from the fibers' ends to the recording electrode P_1 (respectively).

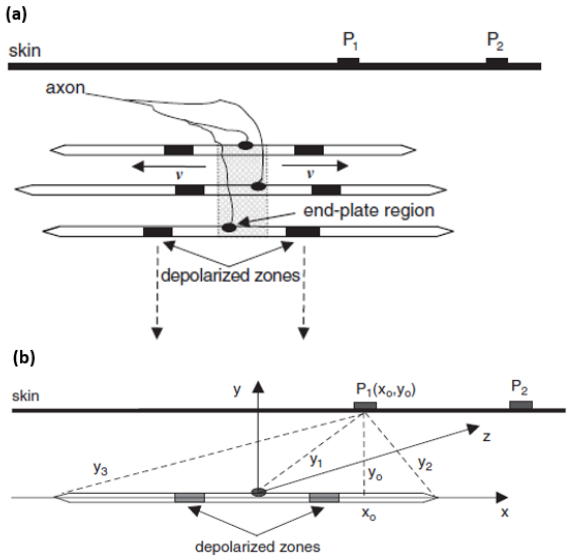

Figure 2.1: (a) A pictorial presentation of a the innervation of finite length muscle fibers by an axon, (b) distances from a muscle fiber to the recording electrode [67].

Consequently, considering that the MU is composed of fibers of finite length and of the same type and the membrane parameters are similar for the entire fibers, regardless of the fiber diameter which can be varied, then the input signal is similar for all the various number of fibers. Thus, the MU can be thought of as a linear time-shift invariant system whose common IR (CIR) is calculated as the summation of the IR of the muscle fibers in the MU. Therefore, the CIR is the sum of potentials that are developed from of the overall number of couples of propagating dipoles recorded at an electrode or a recording point. Accordingly, the calculation of the output

signal, which is the motor unit potential (MUP), comes down to the single convolution between the first temporal derivative of the IAP and the CIR. It is noteworthy to mention that the IR of the MU contains the geometrical information of the muscle fibers such as the finite length, diameter of fibers, the position of the endplate on the fiber axis (longitudinal position x), the location (y and z) of the muscle fibers in the MU region, and the propagation velocity of the excitation waves in a planar configuration. A detailed description of the mathematical equations used can be found in [115].

2.2.2 Precision and robustness evaluation of the tested methods (wMNE & MNE)

The MNE and wMNE inverse problems algorithms, described in the first chapter, will be applied on simulated signals produced by the planar model. First, a reminder of the algorithm used and the parameters involving in it will be depicted. Second, depth weighting which will be used in the wMNE method will be experimented. Then, both methods will be used to reconstruct the sEMG signals after using each of the two methods, and results of how close the original signal is to the reconstructed will be evaluated. Following that, the number of electrodes will be expanded to 16 electrodes and the inverse solutions content will be further analyzed and related to the position of MUs using a fitting approach.

2.2.2.1 Methodology

It is noteworthy to re-mention that, in our tests, an adapted lead field matrix especially fitted for muscles is adopted and will be explained (which we will call the basis waveform matrix or the dictionary). Indeed, a linear relationship is supposed between the potentials measured from the surface of the skin (surface EMG) and the underlying sources that resulted in those measurements. This relationship is shown in Equation 2.1 where $\boldsymbol{b}$ (n×t) is the matrix of the sEMG signals measured at n electrodes and at t time samples, $\boldsymbol{L}$ (p×t) is the unknown matrix of

amplitudes of the MUs along the time, and $\boldsymbol{A}$ (n×p) is the basis waveform matrix (dictionary) whose elements, $a_N(x, t-\tau_{N\tau})$, are yielded from the activation of separate MUs at a definite delay measured from a specific electrode (where p is the number of MUs, $N\tau$ is the number of considered delays, x is the space variable indicating the position of the electrode, and t is the time variable). Please note that these variable names will be used from now on. If the number of columns is increased in matrix $\boldsymbol{A}$, this means that more MUs are used in its construction and/or more time delays are taken. As for its rows, they grow larger as the electrodes used are greater in number. For instance, $\mathbf{a_1(3, t-\tau_2)}$ is the value in matrix $\boldsymbol{A}$, that represents the individual waveform measured from electrode 3 at the activation of MU1 at the second time-delay as demonstrated in Equation 2.2.

$$b = AL \tag{2.1}$$

$$A = \begin{bmatrix} a_1(1,t-\tau_1) & a_1(1,t-\tau_2) & \cdots & a_1(1,t-\tau_{N\tau}) & \cdots\cdots & a_2(1,t-\tau_1) & \cdots & a_2(1,t-\tau_{N\tau}) & \cdots\cdots & a_p(1,t-\tau_1) & a_p(1,t-\tau_{N\tau}) \\ a_1(2,t-\tau_1) & a_1(2,t-\tau_2) & \cdots & a_1(2,t-\tau_{N\tau}) & \cdots\cdots & a_2(2,t-\tau_1) & \cdots & a_2(2,t-\tau_{N\tau}) & & & \\ a_1(3,t-\tau_1) & a_1(3,t-\tau_2) & \cdots & a_1(3,t-\tau_{N\tau}) & & & & & & & \\ \vdots & & & & & & & & & & \\ a_1(n,t-\tau_1) & & & & & & & & & & a_p(n,t-\tau_{N\tau}) \end{bmatrix} \tag{2.2}$$

Additionally, as it is indicated in Equation 2.3, the expansion of the number of rows of $\boldsymbol{b}$ happens with an increase in the number of electrodes. Also, each row in the matrix $\boldsymbol{b}$ represents the surface EMG signal measured at a certain recording electrode when all the MUs were activated according to a certain activation pattern.

$$b = \begin{bmatrix} b(1,t) \\ b(2,t) \\ b(3,t) \\ b(4,t) \\ \vdots \\ b(n,t) \end{bmatrix} \qquad L = \begin{bmatrix} L_{1,1}(t) \\ L_{1,2}(t) \\ \vdots \\ L_{2,1}(t) \\ L_{2,2}(t) \\ \vdots \\ \vdots \\ L_{p,\tau}(t) \end{bmatrix}$$

(2.3)

As for ***L***, it is calculated using the inverse solution methods after constructing ***b*** and ***A***. Its rows will increase depending on the number of MUs and the taken time delays as depicted in Equation 2.3.

2.2.2.2 Proof of concept: column norm normalization and depth weighting

In the following section, the weighting approach [119] in the wMNE method [120] is discussed. The objective of this part is to check how the calculation of the gain (Figure 2.2), will vary as the depth of the MUs will vary. In theory, the gain (amplitude) of a dipole is inversely proportional to its distance from the sensors. In electromyography, this is known as the deep effect on propagating potentials in the tissues. Accordingly, dipoles close to the sensor and hence with a large gain will be depressed in the solution of the inverse problem since their activations are not convenient from the point of view of the functional cost. This solution is biased towards dipoles with smaller gains, namely, the ones farthest from the sensors. Hence, the smaller the gain the farther the source is from the electrode and the larger the gain the closer it is to the sensor.

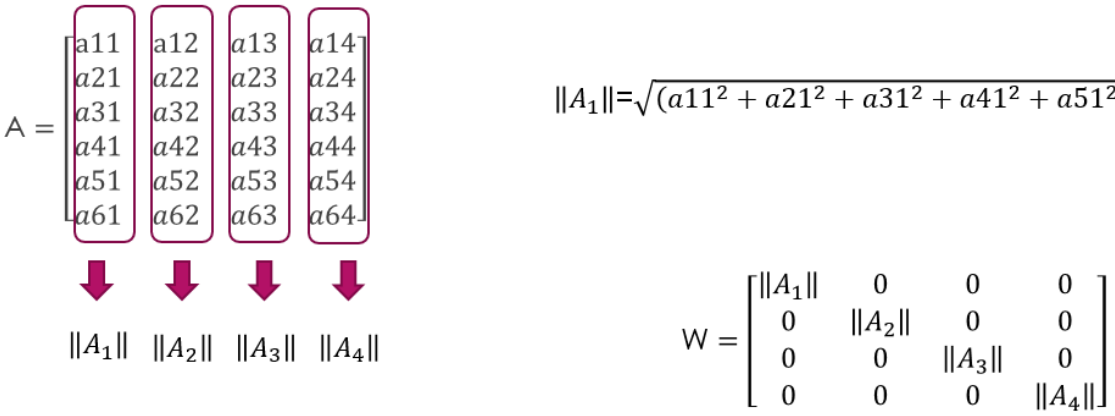

Figure 2.2: An example of how to perform column norm normalization and use it in the computing in the weighting matrix.

To verify the bias occurrence, the depth of two MUs was varied, and calculation of the gain was done for those two MUs each time they are placed on one of four different levels or depths as shown in Figure 2.3.

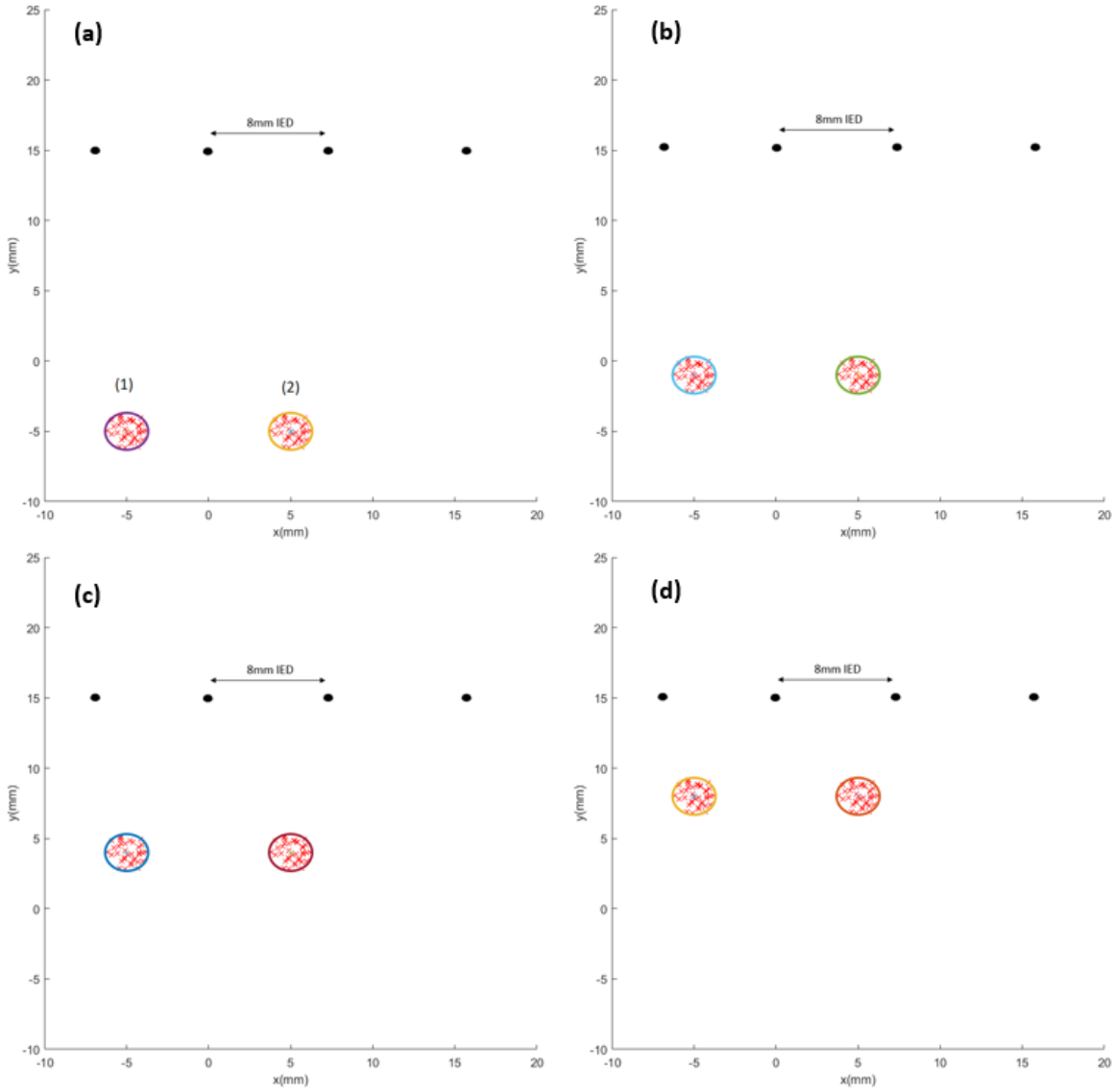

Figure 2.3: The 4 different depths used for each of the two MUs in this simulation. (a) motor units at depth of 20mm (b) motor units at depth of 17mm, (c) motor units at depth of 11mm, & (d) motor units at depth of 7mm.

For each of the levels, all the elements of the basis waveform matrix $\boldsymbol{A}$ were simulated as measured by the set of the same four electrodes as shown in Figure 2.3. In this figure, the x-axis represents the transverse displacement, and the y-axis represents the depth within the muscle

radius. The same physiological model parameters were adopted for the entire simulations. The only thing that was changed was the depth of the motor units. Within a muscle thickness of 10mm, the MUs were located at varying depths.

For example, for the deepest level, the basis waveform matrix and corresponding simulated elements is shown in the matrix in Equation 2.4 and the positioning of the MUs is shown in Figure 2.4. For instance, a_{11} is the signal simulated when MU1 was only present and measured from electrode 1, meanwhile, a_{12} is the simulated signal as measured from the same electrode but when the 2nd MU was only present. Each of those elements were simulated in each of the four scenarios (varying depth).

$$A_{deep} = \begin{bmatrix} a11 & a12 \\ a21 & a22 \\ a31 & a32 \\ a41 & a42 \end{bmatrix} \tag{2.4}$$

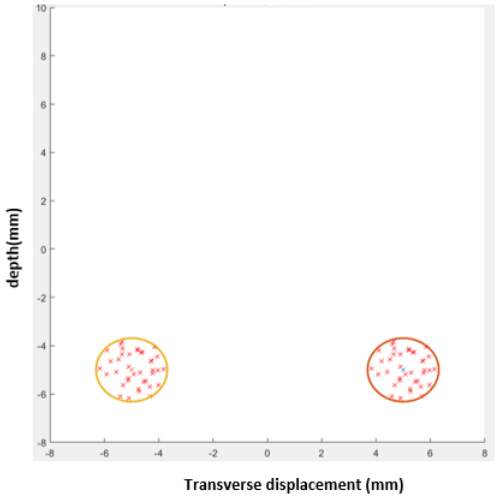

Figure 2.4: Positioning of the sources in the deepest level at 20mm below the recording electrodes.

As mentioned in Chapter 1, to compensate the bias for superficial sources, various weighting strategies have been suggested, among those a weighting technique normalizing the columns of the basis waveform matrix was the most common. This weighting was integrated in the

calculation of the inverse solution as shown in Equation 1.14 in Chapter 1. In fact, each column of $\boldsymbol{A}$ holds the profile of a definite MU, i.e., the signal resulting at the electrodes when this MU is activated. Therefore, the column norm of a superficial MU is greater than the column norm of a MU, farther away from the electrodes. Regarding the calculation of the column norm, for each of the MUs at each of the different levels, the results for level 1 (superficial) was around 200, for level 2 (middle) was around 100, for level 3 (less deep) was around 55, and for level 4 (deepest) was around 40. The column norm for each of the MUs at the four different levels is illustrated in Figure 2.5.

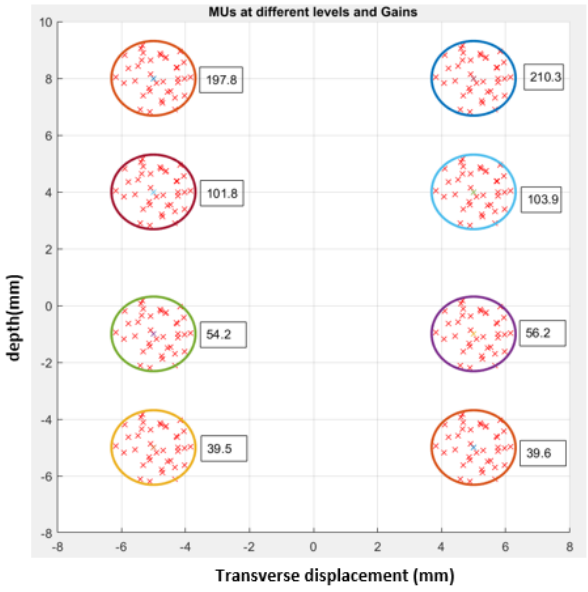

Figure 2.5: A plot of the overall MUs (drawn as circles with crosses inside them indicating the fibers) adopted in the calculation of the column norm of the basis waveforms (numerical value inside a rectangle) when the MUs are at different depths.

From the simulation of each of the MUs in each of the cases (different depth), it was noticed that, first, the amplitude of the signals decreases as the depth increases. For instance, the maximum amplitude for the signal from the deepest level was around 0.25 mV. Meanwhile, the maximum amplitude for the signal from the most shallow or superficial level was around 0.5 mV. As for the column norm calculation, the result proved the depth effect on the column norms.

2.2.2.3 Comparison between MNE and wMNE

In this section, the aim is to prove that the region error when using the wMNE solution is lower than the region error when using the MNE solution since the latter is not depth sensitive. What is meant by the region error is the error between the actual simulated and the reconstructed signals recorded when only specific MUs (either superficial or deep) were activated in a definite region at a time. Regions will be divided to those containing only superficial MUs and those containing only deep MUs. For this to be established, a definite activation pattern was tested in this section and the mean square error per region for each of the two methods was calculated (this will be demonstrated ahead). After that, the same approach was repeated but with the use of a larger electrode grid. Some of the key model parameter values are shown in Table 2.1.

Table 2.1 : Adopted model (Dimitrova & Dimitrov) parameters.

Parameter	Value
Longitudinal muscle conductivity	40×10^{-2} S/m
Transverse conductivity	9×10^{-2} S/m
Conduction velocity	4m/s
Muscle radius	20 mm
MU radius	3 mm
Number of fibers per MU & length of fiber	41/120mm
Distance of endplate to proximal & distal fibre ends	65 & 55 mm

Indeed, in the performed simulations, each MU is going to be considered as a muscle source. As a beginning, for the purpose of testing the two proposed inverse problem algorithms, two MUs were located in the muscle volume conductor model (Figure 2.6), with the first MU situated at a superficial location and the second MU position at a deeper location.

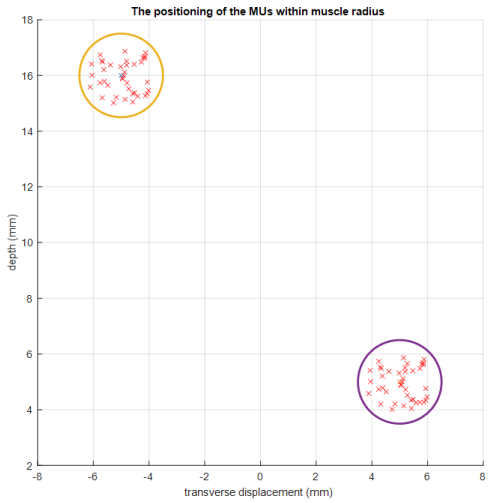

Figure 2.6: A 2D plot of the localization of the two MUs within volume conductor model.

Furthermore, the same electrode configuration (shown in Figure 2.3) was used here and the inter electrode distance (IED) was fixed to 8mm. A 30dB signal to noise ratio (SNR) of a Gaussian type was superimposed to the signals.

Moreover, two time-delays were taken when constructing the basis waveform matrix $\boldsymbol{A}$. A sampling frequency of 2kHz was adopted and signals were simulated for a total of 250ms. A time-delay (τ) of 0ms and 50ms were also considered.

As for $\boldsymbol{b}$, we will consider two different activation criteria. In first activation criterion, only the superficial MU was activated at only one time delay, while keeping the deep MU non-activated for both delays. Even though there are only two MUs, however two time-delays are considered. Therefore, each MU might be activated at one of the time delays. Accordingly, a binary-like pattern of (1 0 0 0) is going to be imposed, where 1 indicates activation and 0 non-activation. For this activation pattern for instance, MU1 is active, and the first time-delay is considered only during the formulation on $\boldsymbol{b}$ (hence taking a value of 1), and the rest takes a value of 0.

For this criterion, the aim is to evaluate the performance of superficial MUs separately. The opposite was made for the second criterion; the deep MU was activated at a single time delay,

while the superficial MU was inactivated at both delays. So, a binary-like pattern of (0 0 0 1) is going to be executed. Therefore, we are examining the influence of the deep MU in this step. As an example, the construction of ***b*** while imposing each of the two activation patterns resulted in the formation of a surface EMG signal at electrode 1 (for each of the patterns) as shown in Figures 2.7 and 2.8 respectively.

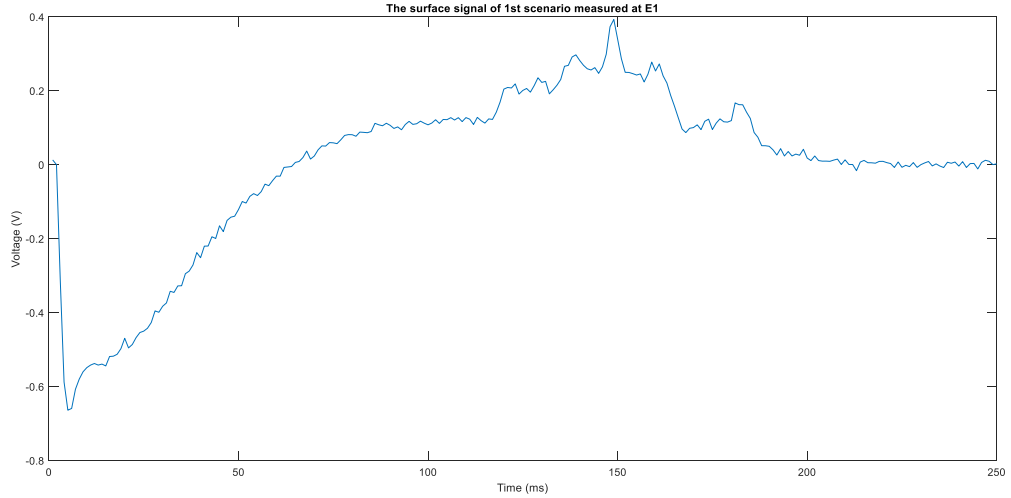

Figure 2.7: The signal recorded at electrode 1 when applying activation pattern 1.

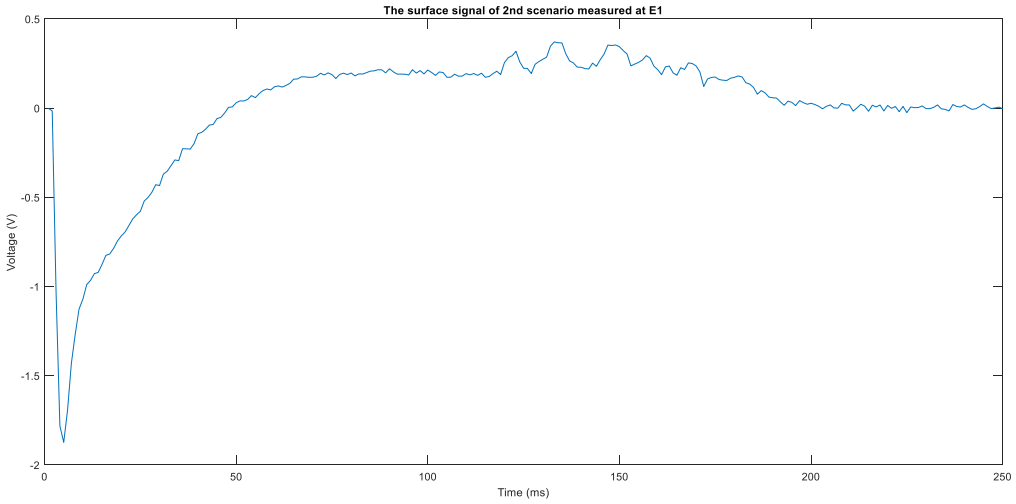

Figure 2.8: The signal recorded at electrode 1 when applying activation pattern 2.

Subsequently, matrix ***A*** will have a size of (4×4), 4 rows representing the electrodes and 4 columns composed of the 2 MUs multiplied by the two time-delays (τ1 and τ2). To evaluate the

efficiency of the proposed inverse methods, the simulated and reconstructed signals are compared by computing the mean square error (MSE). The MSE is described as the average squared difference between the simulated signal and the reconstructed one [121]. Therefore, the MSE between the simulated and reconstructed signals will be calculated for the MNE and wMNE inverse methods. After applying the proposed activation method during the creation of $\boldsymbol{A}$ and $\boldsymbol{b}$, the minimum norm estimation (MNE) and the weighted minimum norm estimation (wMNE) are used to calculate $\boldsymbol{L}$. Afterward, a reconstructed signal $\widehat{\boldsymbol{b}}$ is achieved by multiplying the inverse solution $\boldsymbol{L}$ to the basis waveforms in $\boldsymbol{A}$. The simulated and reconstructed signals (non-normalized) are then compared first visually by producing a plot of each of the two signals and then numerically by calculating the MSE. Note that the MSE is calculated for each MU and each electrode separately. Table 2.2 shows the results of the calculated MSE for the two activation criteria (Only the results of MU2 were displayed here for every electrode since similar results were noticed for MU1).

Table 2.2: The MSE (per MU) between the simulated and reconstructed signals for the two activation patterns.

		MSE (MNE)	**MSE (wMNE)**
Superficial MU Activation	**Electrode 1/MU2 τ1**	0.0278	0.1286
	Electrode 2/ MU2 τ1	0.0445	0.1461
	Electrode 3/ MU2 τ1	0.0131	0.1143
	Electrode 4/ MU2 τ1	0.0151	0.1153
Deep MU Activation	**Electrode 1/MU2 τ1**	0.1396	0.0260
	Electrode 2/MU2 τ1	0.1443	0.0348
	Electrode 3/MU2 τ1	0.1123	0.0120
	Electrode 4/MU2 τ1	0.1147	0.0122

For the first activation pattern, the MSE varied between 0.0131 and 0.0278 for the MNE technique. Meanwhile, it fluctuated between 0.1143 and 0.1286 when using the wMNE. Thus, during the activation of the superficial MU only, the MNE method outperformed the wMNE as it

is indicated by the lower MSE. In contrast, when the deep MU was only activated, the MSE was higher for the MNE method where it varied between 0.1123 and 0.1443.

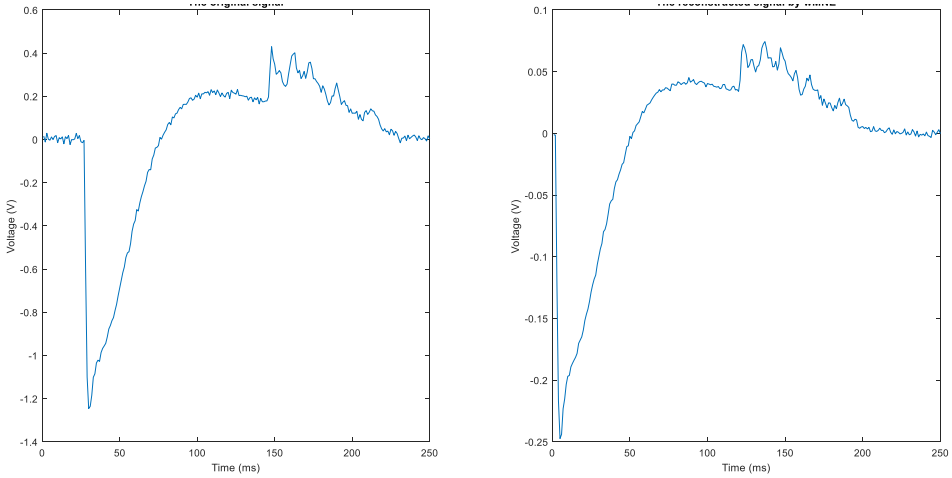

Figure 2.9: A plot of the actual simulated (left) and reconstructed (right) signals using the MNE method for the 2nd activation pattern.

The wMNE gave a lower MSE ranging between 0.0120 and 0.0348 making the wMNE superior to MNE when deep MUs are included. Figures 2.9 and 2.10 display the simulated (to the left) and reconstructed (to the right) signals (as viewed from a single electrode) produced using the MNE and the wMNE methods respectively.

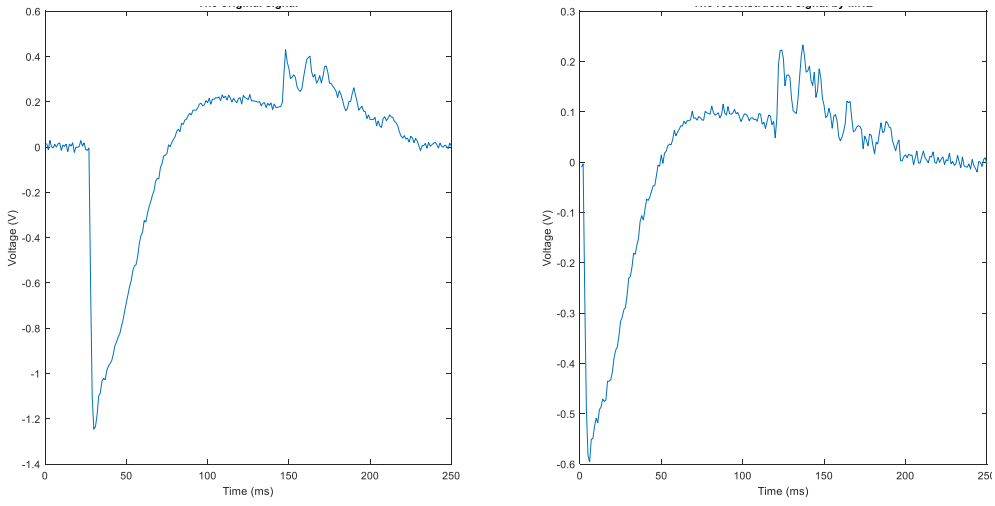

Figure 2.10: A plot of the actual simulated (left) and reconstructed (right) signals using the wMNE method for the 2nd activation pattern.

Also, the same plots were produced but now for the signals produced when imposing the 1st activation pattern (this time the plot was for signals measured at electrode 2) and shown in Figure 2.11 for the MNE method and in Figure 2.12 for the wMNE method.

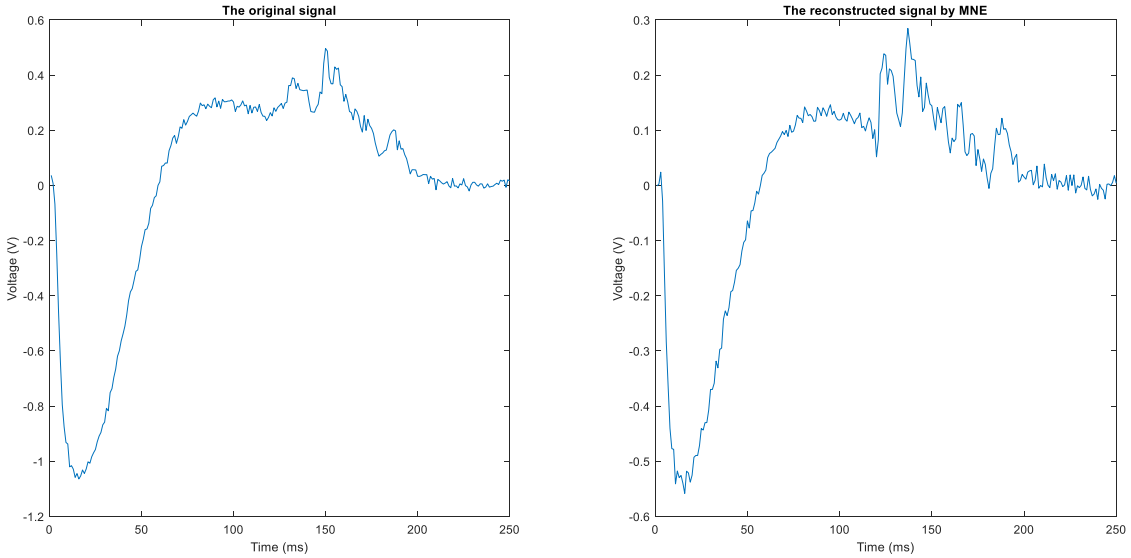

Figure 2.11: A plot of the simulated (left) and reconstructed (right) signals using the MNE method for the 1st activation pattern.

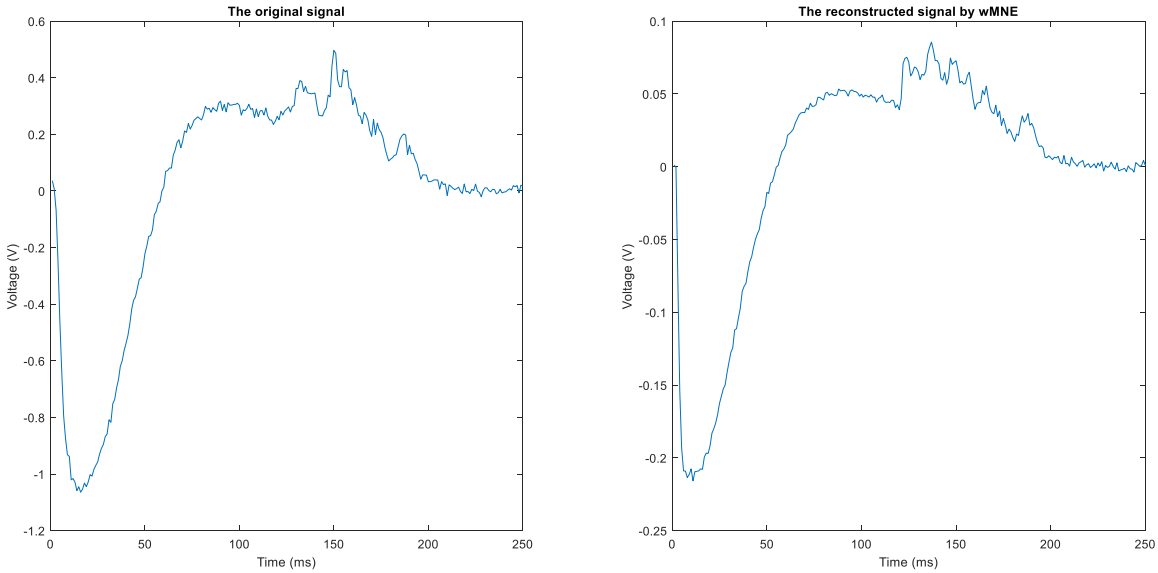

Figure 2.12: A plot of the simulated (left) and reconstructed (right) signals using the wMNE method for the 1st activation pattern.

Accordingly, it can be concluded that the MUs in the original and reconstructed signals have close positions because they are resulting in the production of similar signals as reflected by the low MSE they produce.

Hence, this confirms the good performance of the applied algorithms [122]. However, we are not yet capable of predicting the positions of those MUs yet. What is available until now is an indirect method of assessing the position. After that, the simulation was advanced by increasing the number of electrodes where a 4×4 (16 electrodes) grid was used. Additionally, the R squared (R^2) value was used to compare the methods [123]. Three deep MUs were placed in this simulation as shown in Figure 2.13.

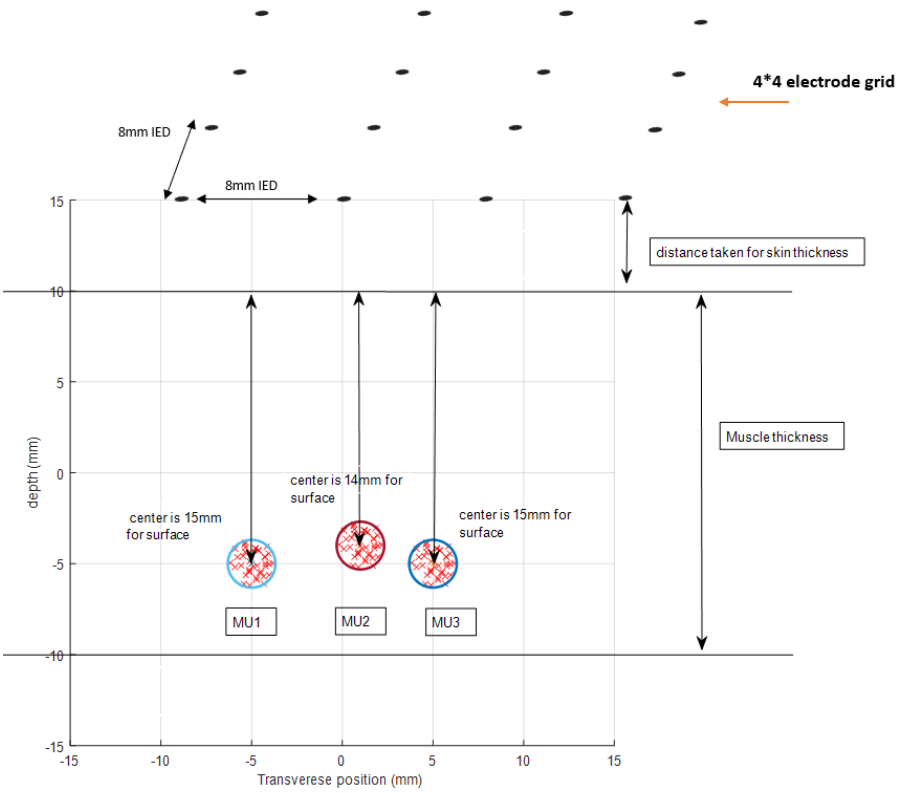

Figure 2.13: 3 deep MUs in the 4×4 electrode grid simulation.

The correlation coefficient R^2 was calculated for each of the 3 MUs (each time by zeroing the effect of the other 2 MUs) as measured by each of the 16 electrodes. However, since all

exhibited similar results, only the result for MU1 will be displayed in Table 2.3. The results shown in Table 2.3 show the superiority of the wMNE method over the MNE method in the presence of only deep sources even when the model parameters were extended.

This is shown by an increased R^2 value percentage for the wMNE in all of the electrodes (a value of 100% indicating perfect similarity).

Table 2.3: A summary of the R squared percentage results for MU1.

3 deep sources (MU2 & MU3 are zeroed and MU1 is studied)	**R squared (%) MNE**	**R squared (%) wMNE**
MU1/ E1	31%	59%
MU1/ E2	44%	86%
MU1/ E3	37%	79%
MU1/ E4	8%	72%
MU1/ E5	44%	85%
MU1/ E6	43%	89%
MU1/ E7	23%	72%
MU1/ E8	0.5%	19%
MU1/ E9	40%	79%
MU1/ E10	24%	77%
MU1/ E11	1%	16%
MU1/ E12	65%	68%
MU1/ E13	16%	73%
MU1/ E14	30%	53%
MU1/ E15	4%	32%
MU1/ E16	33%	39%

By trying such scenarios, we were able to prove the superiority of one of the two methods over the other depending on the positioning of the MUs.

2.2.2.4 An insight to source localization by a fitting equation

Until now, the previous work done uses the inverse solutions to reconstruct the signals and compare them to the original signals in an approach to assess the efficiency of the inverse methods. In this section, however, an analysis of the inverse solution is presented from which a methodology for predicting the positioning of MUs is extracted. Before discussing the steps followed to do so, note that in this section the sampling frequency was taken as 2kHz, a 4×4 electrode grid with 8mm IDE was used, and a noise of 20dB [7] was added to each of ***A*** and ***b***.

Let us start first by recalling the steps needed to solve the inverse problem before introducing the new steps. For instance, let us consider the example of the 3 MUs present in Figure 2.13. Suppose that each of those 3 MUs will fire at a separate time during 5 seconds of simulation time. Accordingly, the overall interference signal ***b*** will be as that seen in Figure 2.14 (as seen from one of the 16 electrodes).

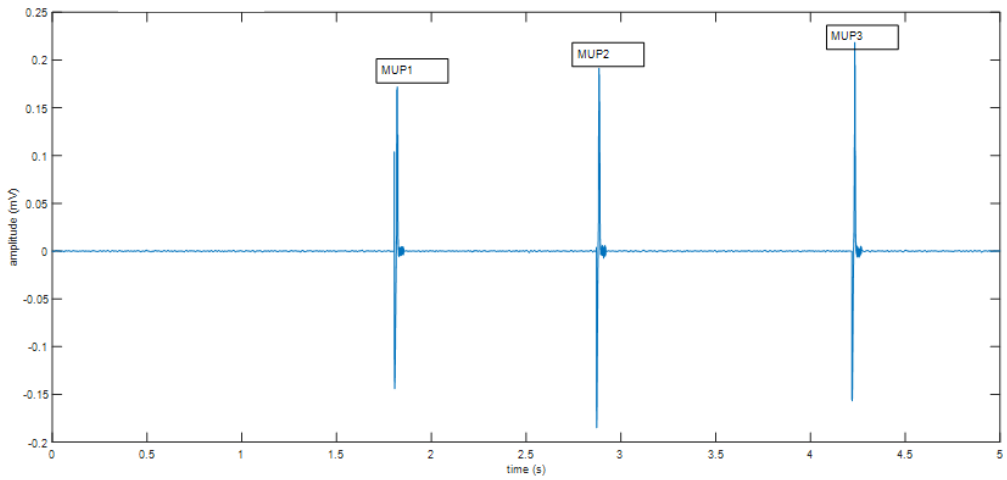

Figure 2.14: Overall surface signal ***b*** (recorded from electrode 1).

The second requirement to solve the inverse solution is the creation of the basis waveform matrix ***A***. This matrix is going to contain sub-matrices that represent the individual contribution of each of the MUs contributing to the formation of ***b***. Let us elaborate on how ***A*** is formulated. Suppose

that MU1 is activated and its MUAP is recorded by the 4×4 electrode grid for only a short period of time (usually the typical duration of a MUAP). However, for illustration purpose, the duration of each MUAP will be taken a bit longer than usual and will be around 125ms (approximately 125ms multiplied by the frequency of 2kHz will give 251-time samples). Accordingly, each submatrix in $\boldsymbol{A}$ is going to have number of columns equal to the activation time (251 columns), and number of rows equal to the number of recording electrodes (16 rows). This will be repeated for the 3 MUs that we are considering in this example. This will produce an overall matrix $\boldsymbol{A}$ with number of columns equal to 753 (251 multiplied by 3) and number of rows equal to 16. Therefore, we can expand the matrix $\boldsymbol{A}$ column wise by adding more MUs (the number of MUs will be given the symbol p) and we can increase the number of rows by increasing the number of recording electrodes (which will be given the symbol n). $\boldsymbol{A}$ and $\boldsymbol{b}$ are related to the inverse solution $\boldsymbol{L}$ by the linear system shown previously in Equation 2.1 ($\boldsymbol{L}$ is governed by the minimum norm estimation for this section). Consequently, the number of rows of $\boldsymbol{L}$ will be the same as the number of columns of $\boldsymbol{A}$ (and will be holding information about each individual MU) and the number of columns will depend on the duration of signal $\boldsymbol{b}$. Now that the construction of each of the matrices is clarified, we can move to the explanation of the adopted method. To begin with, suppose a vertical alignment of 4 MUs which are positioned at varying depths as shown in Figure 2.15. For such an alignment, $\boldsymbol{b}$ will have a size of 16×8000 (since it is measured by the electrode grid for 4 seconds at a frequency of 2kHz), $\boldsymbol{A}$ will have a size of 16×1004 (4 MUs each firing for a duration of around 125ms at a 2kHz frequency), and the inverse solution $\boldsymbol{L}$ (if the entire $\boldsymbol{b}$ was taken) will have a size of 1004×8000. Each of the 4 MUs will fire during a different time of the 4 seconds as shown in Figure 2.16 (MU1, which is the most superficial, starting first and then MU2, MU3, and MU4 respectively). However, for the purpose of

computational time reduction, a moving window of a smaller size will be travelling throughout ***b*** during the calculation of the inverse solution. For this example, the window size will be taken as 1000 (0.5 seconds) as shown in Figure 2.16. Accordingly, each ***L*** will have a size of 1004×1000.

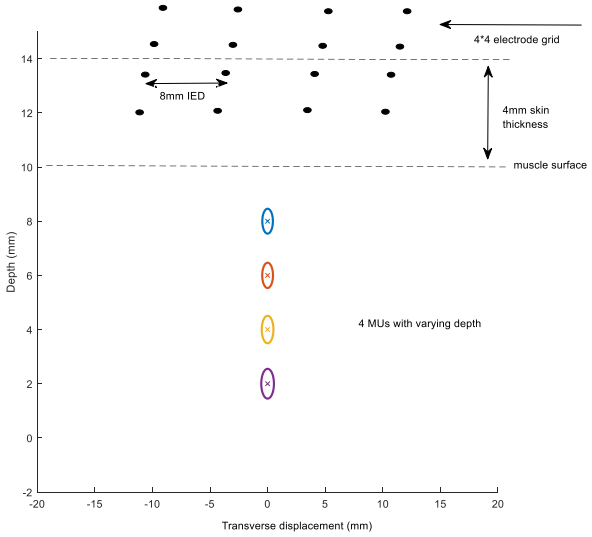

Figure 2.15: Alignment of MUs with respect to electrode grid.

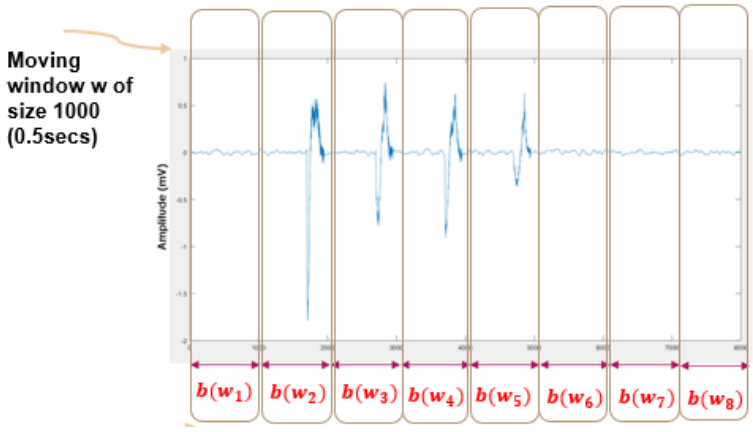

Figure 2.16: The interference surface EMG signal **b**.

Based on what was previously explained, for a window length ***w*** of 1000, we are going to have 8 inverse solutions ***L***. Each one of the 8 yielded ***L*** is then going to have a size of 1004*1000 (not all ***L***s will contain useful information; some will only contain noise, and useful information will be in those where the moving window coincides with the firing of one of the MUs). Moreover, each 251 rows in each of the 8 yielded ***L***s will represent the activity coefficient of a definite MU.

As an example, the first part of $\boldsymbol{L}$ (the rows from 1-251) will encompass the activity coefficient of the first MU. Following the computation of the windowed inverse solutions ($\boldsymbol{Lw_{1\text{-}8}}$), the yielded solution for each window used to produce a 3D plot where the columns of $\boldsymbol{L}$ are displayed on the X-axis (size of 1000) and the rows of $\boldsymbol{L}$ are displayed on the Y-axis (size of 1004). Furthermore, at each X-Y coordinate an amplitude is recorded representing the Z-axis. A color bar indicating the degree of the intensity is placed at the right of each plot. Note that the Z-axis amplitudes were normalized (just for the purpose of a better display of the results, the same procedure can be applied without normalization) and will vary between 0-1 (before chopping the signal into windows the inverse solution with the entire un-chopped signal is calculated and the maximum value is extracted for normalization).

As it was shown in Figure 2.16, when using $\boldsymbol{bw_1}$ to get $\boldsymbol{Lw_1}$, that part of $\boldsymbol{b}$ only contained noise and did not contain any MUAP. Consequently, one would expect after calculating the inverse solution and plotting $\boldsymbol{Lw_1}$ to have a minimum intensity in the entire rows of $\boldsymbol{Lw_1}$. Therefore, when the part of $\boldsymbol{b}$ used in the calculation of the inverse solution is not including the firing of any MU, a minimum amplitude (almost zero indicating the presence of noise only) will be noticed; this was noticed when calculating $\boldsymbol{Lw_1}$, $\boldsymbol{Lw_6}$, $\boldsymbol{Lw_7}$, and $\boldsymbol{Lw_8}$ which showed a zero map.

On the contrary, if the window passing through $\boldsymbol{b}$ includes the activation and firing of a definite MU, it is normal to expect that the $\boldsymbol{L}$ yielded using this $\boldsymbol{b}$ will have a high activity coefficient in the location where this MU is naturally present. As a matter of fact, this was observed when plotting $\boldsymbol{Lw_2}$, $\boldsymbol{Lw_3}$, $\boldsymbol{Lw_4}$, and $\boldsymbol{Lw_5}$. As a demonstration, the content of $\boldsymbol{Lw_2}$ will be shown in a 3D plot and the rest of the results will be summarized in Table 2.4. For the calculation of $\boldsymbol{Lw_2}$, $\boldsymbol{bw_2}$ is used (Figure 2.17). Therefore, a maximum peak should be observed in the part of $\boldsymbol{Lw_2}$ corresponding to MU1 which is the most superficial (rows 1-251). This is confirmed in Figure

2.18, where a maximum amplitude is detected at Y=9 in $\boldsymbol{Lw_2}$. This result asserts the efficiency of the adopted inverse algorithm. The peak at Y=9 registered the highest value with a normalized amplitude of 1, which is guessed since it is the most superficial MU.

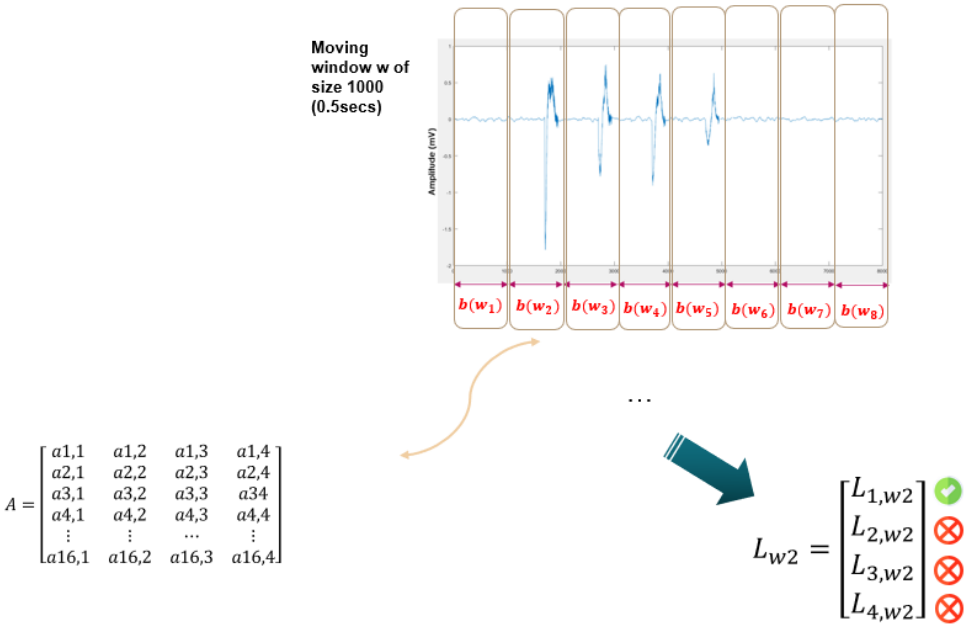

Figure 2.17: An illustration of the calculation of $\boldsymbol{Lw_2}$.

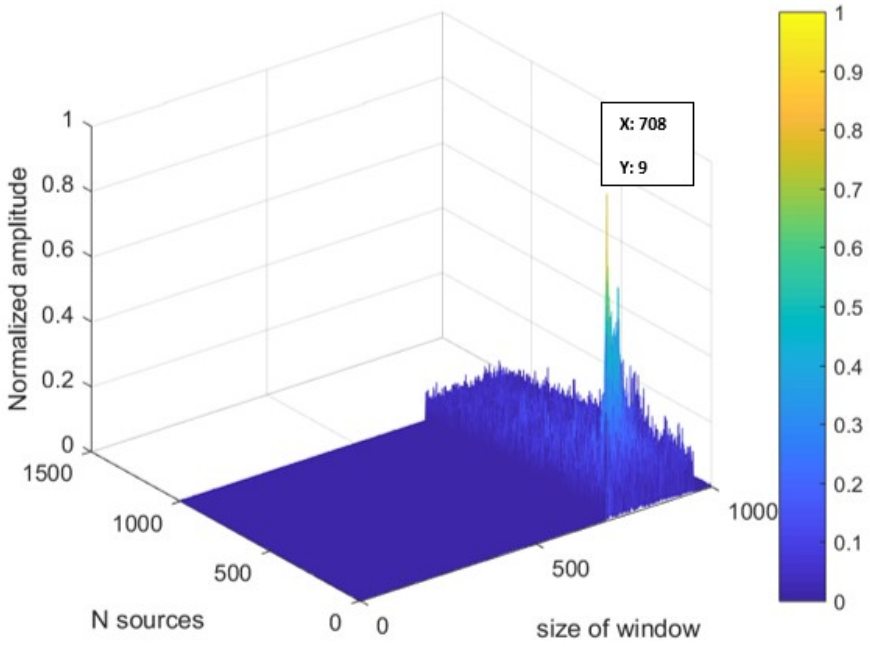

Figure 2.18: A 3D plot of $\boldsymbol{Lw_2}$ giving information about MU1 position.

The same thing was yielded for Lw_3 when calculated using bw_3 (coincides with MUAP2). In Lw_3, the amplitude was the highest at Y=263. A decrease in the normalized amplitude was noticed in Lw_3 with a value equal to 0.58. This is because the second MU is in a deeper location than the first one. A similar pattern was observed during the computation of Lw_4 using bw_4 and Lw_5 using bw_5 respectively. The highest amplitude further decreased to reach 0.43 at a location of Y=519 in Lw_4, providing us with data about the third MU, and then to a value of 0.21 at Y=775 in Lw_5, revealing data about the fourth MU. This is because MU3 and MU4 are positioned in deeper locations. Another observation from the content of those windowed inverse solutions is that the location of the highest amplitude was shifting in place as the depth increased [124].The shift in the Y coordinate and the change in the normalized amplitude as the depth is increased (for Lw_2, Lw_3, Lw_4, and Lw_5) are shown in Table 2.4.

Table 2.4: A summary of the inverse solution results.

	Normalized amplitude Z	**Y-coordinate**
Lw_2	1	(9)
Lw_3	0.58	(12)
Lw_4	0.43	(17)
Lw_5	0.21	(22)

Furthermore, when the Y coordinate information was plotted against the corresponding depth of the source it represents, a fitting equation, which enables estimating the corresponding depth information for a given yielded coordinate, is proposed.

This approach is depicted in Figure 2.19. To test the equation efficiency, a MU with a depth of 5mm was simulated and the yielded Y-coordinate for this depth was substituted in the equation

seen in Figure 2.19 (where c represents the Y-coordinate and d represents the depth); a depth of d=4.21 mm was retrieved. This validates the efficiency of the proposed methodology and the stability of the relationship between Y-coordinate and the depth.

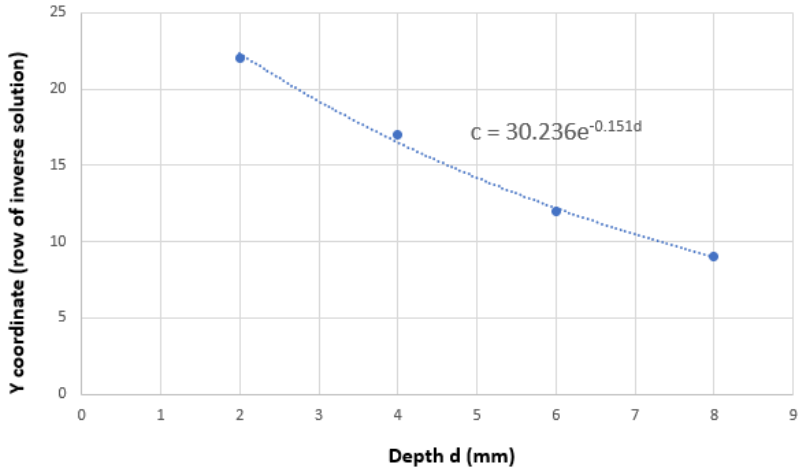

Figure 2.19: A scatterplot of Y-coordinate versus depth.

The same procedure was tested on a horizontal alignment of MUs (having the same depth but with different transverse locations). The results yielded for such a configuration highlighted the limitations of the model being used. Results showed that the position of the maximum amplitude of the Y-coordinate was not changing with transverse change, so we were not capable of differentiating between a MU placed on the right and one on the left. Consequently, we reached the limit of this model and we need to shift to another more realistic model to design a more efficient identification method based on 2D curve fitting.

2.3 Curve Fitting Based Minimum Norm Estimation for Motor Unit Spatial Localization (CFB-MNE)

In this section, an improvement of the previous identification methodology is described. It bears on the use of a more realistic generation model of the HD-sEMG signals. For this purpose,

a description of the analytical cylindrical volume conductor model will first be presented. Following that, the formulation of the inverse problem will be explained as well as the proposed innovative algorithm for source localization. Then, this algorithm will be tested using several computer simulations to verify its validity.

Afterwards, the yielded results and a discussion of the limitations and capabilities of the proposed algorithm will then be tackled. Finally, in the last part of this study, conclusions will be drawn, and an insight of future perspectives will be addressed.

2.3.1 Description of the cylindrical generation model

All the tests done in this section are simulated using a fast analytical HD-sEMG model developed by Carriou et al. [23]. We used an analytical model instead of a numerical one mainly due to the diminished time of the analytical model in giving an estimated solution compared to a numerical one [23, 125].

In a comparative study performed by Heringa et al. [126], results showed that the use of analytical models yielded low storage requirement and fast convergence compared to their numerical counterparts. Since time is the most important concern in the previously suggested sEMG applications, the model proposed by Carriou et al. will be adopted in this study.

This model, composed of multi layers (muscle, fat, and skin), provides a cylindrical description of the volume conductor model with cylindrical coordinates (ρ, θ, z). As shown in Figure 2.20(a), the center of the muscle cylinder is considered as origin of the volume conductor, and each of the three layers has a finite length in the radial direction (ρ).

As for the skin and fat layers, both are homogenous and isotropic. Meanwhile, the muscle layer, even though homogenous, is classified as being anisotropic (the longitudinal direction records a

higher conductivity than the others). Regarding the muscle sources, those are modeled as fibers situated in the inner most layer (muscle layer) along the z-axis. The intracellular action potential production, propagation, and extinction along the fiber is considered in this model. This model also allows the existence of four types of MUs (slow (S), fast intermediate (FI), fast resistant (FR) and fast fatigable (FF)).

Furthermore, the recruitment of the MU relies on the size principle. Moreover, surface integration of the electrical activity generated by the muscle portion under the area of an electrode grid (Figure 2.20(b)) is performed to yield the HD-sEMG signal. This electrode grid is positioned at the outermost boundary, formed between the skin and air.

What distinguishes this model from other models is that it calculates the electrical activity at the skin surface entirely in the Fourier frequency domain. Heavy convolutional operations are transformed into simpler tensor multiplications allowing faster and more efficient simulations. As a matter of fact, the calculus starts from the calculation of single fiber action potential (SFAP), moves to the computation of the motor unit action potential (MUAP), and then ends in the calculation of the HD-sEMG signal (all in the frequency domain).

The yielded result is further multiplied by the transfer function of the volume conductor model, which is calculated and stated in frequency coordinates. Note that the transfer functions of the volume conductor model are obtained by Poisson's equation (for the layer containing the sources) and by Laplace equation (for the other two layers).

Finally, the surface electrical activity is calculated by performing the 3D inverse FT of the obtained multiplication results, and this will result in the formation of a potential map in the

spatio-temporal domain where the HD-sEMG signals are obtained by surface integration procedure under the electrodes [23, 127].

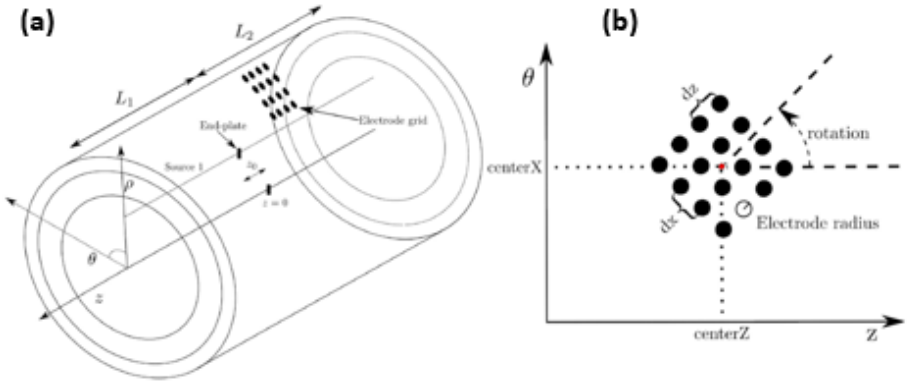

Figure 2.20: Cylindrical volume conductor model (a), and a 4×4 electrode grid with its associated parameters (b) [127].

A detailed mathematical explanation of the calculus adopted in this model can be found in [23]. To summarize the mathematics of the model, consider the illustration shown in Figure 2.21. The recruitment illustration depicts the firing of various MUs at a specific time.

The Fourier transform (FT) of this recruitment is first calculated. This is then multiplied by the 2D FT of the source, which is the IAP generated at a particular time along the z-axis of the muscle fiber.

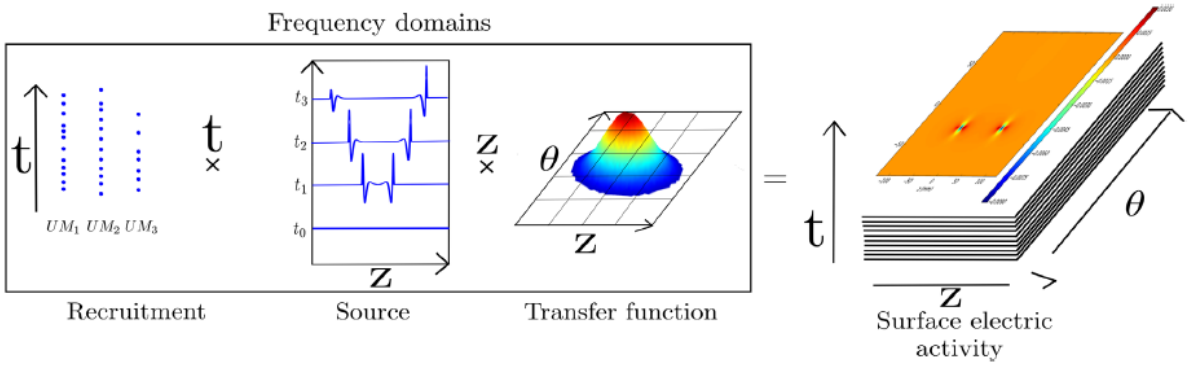

Figure 2.21: A depiction of the calculus of the SFAP [127].

Table 2.5 shows some of the model configuration used for the simulations done in this study.

Table 2.5: Multi-layered cylindrical model (Carriou) configuration.

Parameter	Value (unit)
Sampling frequency	2048 (Hz)
Radial muscle conductivity	0.3 (S/m)
Angular muscle conductivity	0.3 (S/m)
Longitudinal muscle conductivity	0.9 (S/m)
Muscle length	150 (mm)
Muscle radius	30 (mm)
Fat conductivity	0.05 (S/m)
Fat thickness	2 (mm)
Skin conductivity	1 (S/m)
Skin thickness	1 (mm)
Number of electrode grids	1
Center of electrode grids (θ,z)	(0,30) (°, mm)
Number of electrodes	16
Inter-electrode distance (dθ,dz)	(8,8) (mm, mm)
Electrode radius	2 (mm)
Simulation time	4 (s)

2.3.2 The CFB-MNE algorithm formulation

To start with, it is noteworthy to mention that the same methodology explained in Section 2.2.2.1 to construct $\boldsymbol{A}$ and $\boldsymbol{b}$ and to compute $\boldsymbol{L}$ will be followed here. Moreover, the inverse approach that was used for the proposed algorithm was the MNE method only. Although previous results showed that the wMNE inverse method was biased for deeper MUs (reflected by the lower error yielded when comparing the actual and the reconstructed signals) the inverse solution using the wMNE when a big number of mixed MUs were used (both superficial and deep as that seen in Figure 2.2) was always biased for the deepest MU.

Since in practice this algorithm is a blind algorithm and we will have a mixture of deep and superficial MUs, it was shown that the inverse solutions (when MUs as those in Figure 2.2 were used) using the MNE method gave more useful and explainable data that can aid in our algorithm than those yielded by the wMNE.

For this reason, the MNE method was chosen since, as it will be shown later, it allowed the creation of a method that is capable of localizing MUs regardless from their depth. The detailed description of the steps required to localize the positioning of MUs will be mentioned in this section.

The broad and starting idea is to use a limited number of MUs of known locations and characteristics and extract certain information from the inverse solution (in which those MUs participated). The reason why we want the number to be limited is because as we increase the number of MUs participating in the inverse solution calculation, the prediction time will also increase.

Therefore, we should create a tradeoff between the appropriate number of MUs capable of providing enough information for accurate source localization and between the time it takes to do so. In fact, it was evident that depending on the position of the MU, the characteristics of the inverse solution was changing. If this inverse solution was to be plotted in a 3D plot, we will notice that the inverse solution corresponding to each MU will have a different pattern or fingerprint; its shape will change.

Accordingly, in an approach to test which information extracted from this inverse solution best reveal the accurate positioning of the MU, 3 different parameters obtained from the inverse solution will be tested. The selected parameters are the maximum amplitude (Z_{max}), average

amplitude (Z_{avr}), and energy (E); energy is calculated by computing the 2-norm or maximum singular value of Z, and then squaring it [128]. The purpose of collecting certain data from the inverse solution, is to use this information to create a fitting curve to be used later to predict the positioning (ρ and θ) of a definite MU.

This study will first start by placing 25 MUs of known locations and properties within the volume conductor model as portrayed in Figure 2.22 to the left. In this 2D plot, the y(mm) reflects the angular displacement and the x(mm) reflects the radial depth. The MUs have varying ρ (there are 5 ρ values covering a depth of 8mm and are 2mm apart). Those MUs also have an angular coverage ranging between -30° to 30° (5 θ values 15° apart).

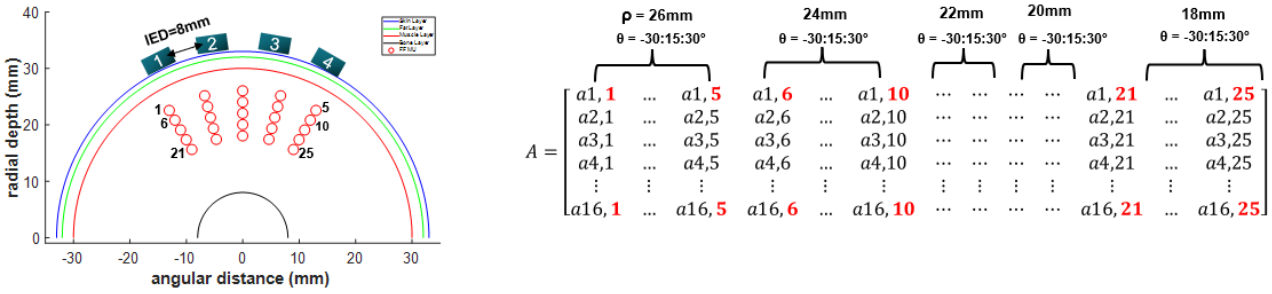

Figure 2.22: A depiction of the 2D position of the MUs (to the left) and the dimensions of matrix A column wise (to the right).

Those MUs involved in the construction of the basis waveform matrix ***A*** and the overall surface EMG signal ***b***. As explained in the previous section, ***A*** will comprise the MUAPs of each of the 25 MUs when present alone.

The firing time of each MU is around 20ms and the frequency is equal to 2048 Hz. Therefore, each submatrix in ***A*** (representing the firing of a single MU) will have a length of 40 time-samples. This will make ***A*** have an overall size of $16(\text{electrode}) \times 1000(25\,MUx40\text{time} - \text{samples})$. Figure 2.22 shows how the different columns of ***A*** are constructed. Regarding ***b***, this signal will include the firing of each of the 25 MUs (with no overlapping between the firing of

each MU as it was shown previously in Figure 2.17) collectively from the 16 different electrodes for a duration of 1 second, and thus will have a size of $16(\text{electrode}) \times 2048(\text{time} - \text{samples})$.

However, when calculating the inverse solution ***L***, a moving window ***w*** of a size equal to the size of firing of each MU is going to be applied on ***b*** and used with ***A*** (containing the participation of the entire 25 MUs). Accordingly, in **each calculation process**, the yielded inverse solution ***Lwi*** as the window is moving will have a size of 1000×40 and will include information regarding **one of the 25 MUs at a time**.

The number of rows in each ***L*** will correspond to the activity coefficient of one of the 25 MUs (25 MUs each of a size of 40 time-samples), and the number of columns will be dependent upon the size of the moving window across ***b***.

For instance, if the moving window was passing through the part of ***b*** that includes the firing of MU1 and the inverse solution was calculated, the yielded ***L*** is expected to have the highest coefficient in the 1st 40 rows of ***L*** (since in ***A*** the firing of MU1 was placed at the beginning of the matrix).

A 3D plot of ***L*** is shown (Figure 2.23), where the Y-axis represents the number of rows in ***L*** (equal to the number of columns of ***A*** and gives an idea about the MU). The X-axis represents the number of columns in ***L*** (determined by the window size moving across ***b***), and the Z-axis represents the amplitude or intensity at each X-Y location. One can observe a distinct pattern was noted at a location corresponding to MU1.

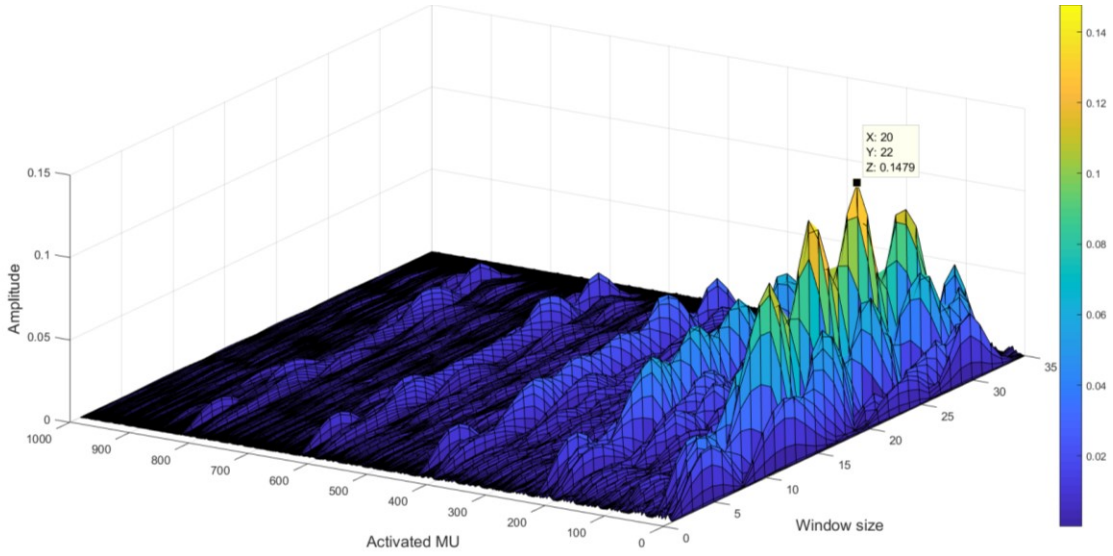

Figure 2.23: A 3D plot of the inverse solution L calculated with a part of b containing the firing of MU1.

The next step involves extracting the parameters Z_{max}, Z_{avr}, and E of this pattern. The same thing is to be repeated for the entire useful information obtained as the window is moving across ***b*** and the inverse solution is being calculated.

Eventually, 25 different Z_{max}, Z_{avr}, and E sets will be gathered, and each of the 25-parameter set will be used to create a fitting curve. Figure 2.24(a) shows the fitting curves (of a biharmonic type) which is composed of the 25 Z_{max} extracted from the inverse solution (the black dots on the curve represent the Z_{max} for each of the 25 MUs which were used to formulate this curve). Similar plots are shown for Z_{avr} and E in Figures 2.24(b) and 2.24(c) respectively.

In those curves, θ information were plotted on the X-axis, the various ρ values were plotted on the Y-axis, and the Z-axis was preserved for Z_{max}, Z_{avr}, or E. The fitting curve is a biharmonic spline interpolant. This interpolating surface is a linear combination of Green functions centred at each data point [129]. For 1D, the surface s(x) is expressed in Equation 2.5.

$$s(x) = \sum_{j=1^n} w_j, g(x, x_j) \tag{2.5}$$

where n in the number of data points $x_j = (x_j, y_j)$, $g(x, x_j)$ is the Green's function, and w_j is the weight of data point j. The derivation of the technique in 2 or more dimensions is similar to that of the 1D and a more detailed explanation can be found in [129]. Now, this fitting curve will be used to anticipate the position of MUs of unknown locations.

This procedure involves placing a tested MU randomly within the volume conductor and recording the signal $\boldsymbol{b}$ for this test point. Then the inverse solution for this test point is to be calculated by using its corresponding $\boldsymbol{b}$ and the entire $\boldsymbol{A}$ matrix which we composed ahead of time. From the inverse solution of the test MU of an unknown position, Z_{max}, Z_{avr}, and E will be extracted and will be fitted in each of the 3 fitting curves to see the corresponding ρ and θ that each will yield.

Then the root mean square error (RMSE) [130] between the actual and predicted position will be calculated for each dimension. Plus, during the calculation of the inverse solution, it was noted that for deeper MUs, a distinct pattern was noticed in the range of the MU that was positioned above the deeper MU instead of its actual range. For illustration purposes, the following example will be taken; consider MU6 which is positioned at ρ=24mm and θ=-30°.

Normally, the inverse solution $\boldsymbol{L_{w11}}$ of this MU should have had a Z_{max} in the range 241:280th rows. However, since this MU is masked by a more superficial one at the same angle (the 1st MU ρ=26mm and θ=-30°), then the Z_{max} was noted to be in the range 1:40 (at Y=17 which corresponds to MU1) instead of the range 201:240. This is shown in Figure 2.25. This was also noticed in each of the MUs placed at the deeper levels. This observation illustrates the difficulty of recovering the position of deep MUs. To avoid this problem, the algorithm 1 will be modified and tested in the next section.

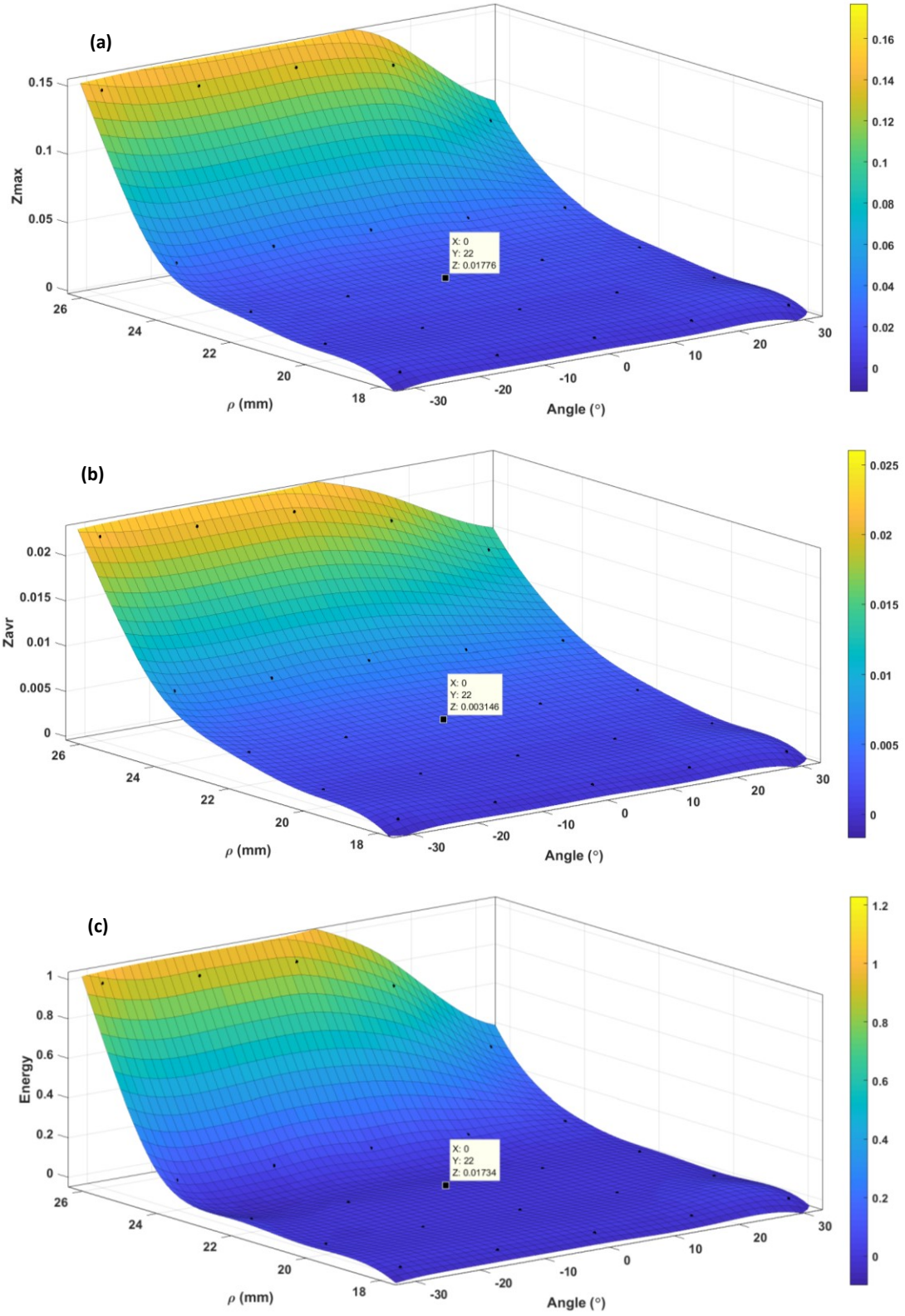

Figure 2.24: The 3D fitting curves of Zmax (a), Zavr (b), and E (c).

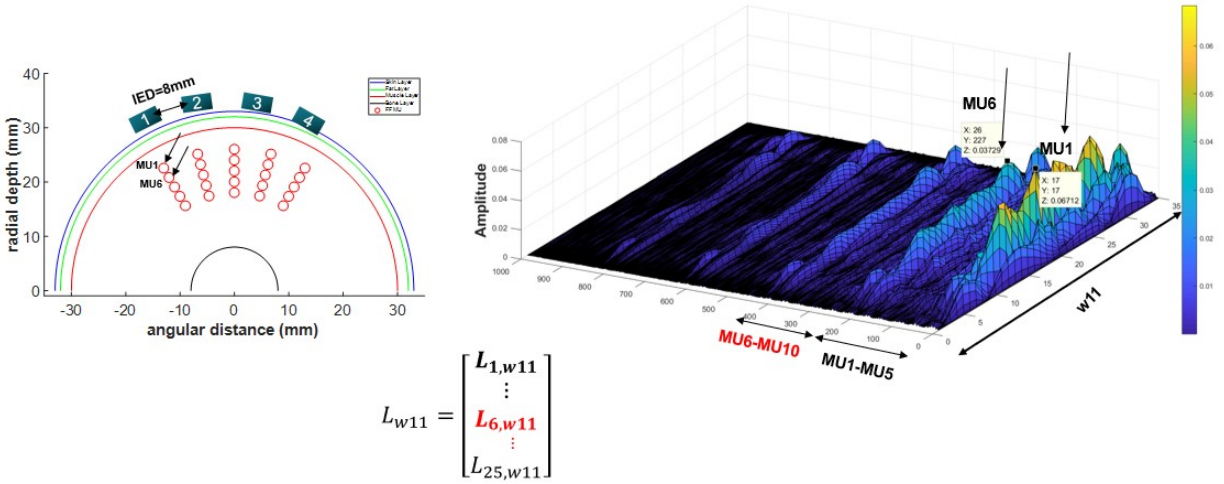

Figure 2.25: A 3D plot of the inverse solution Lw11 of a deep MU showing the problem faced with deep MUs.

After, a detailed description of the various algorithms used to localize MUs and how each of those algorithms was tested is given. In the first algorithm, when extracting the information from the inverse solution for each MU, Z_{max}, Z_{avr}, and E will not be calculated from the information of the part of the inverse solution having the maximum intensity. Instead, those parameters will be calculated from the portion of the inverse solution where each individual MU should have had a maximum amplitude (this is known before since in this part of the work prior to developing the fitting curves, we are dealing with pre-defined MUs which we know the location of which and thus we know where in the inverse solution each MU should give the highest peak). To further explain this step, one can consider the following example: after calculating the inverse solution using a matrix ***A*** containing the 25 MUs and using a specific window (which will include the MUAP of one of the 25 MUs at a time) of the surface recording ***b*** (containing the MUAPs of the 25 MUs) the yielded inverse solution ***L*** should be zero everywhere except at the location corresponding to this MU. For instance, if the window was passing through the part of ***b*** including the MUAP6, then one would expect that all the rows of ***L*** will be almost zero expect those rows between 201:240 (since if you refer to Figure 2.22, those rows correspond to MU6 and should contain the highest activity coefficient). However, as it is shown in Figure 2.25, non-

zero values were noticed at two different locations in $\boldsymbol{L}$. The first location is between the rows 201:240 with a peak of 0.037, and the second location is between the rows 1:40 with a higher value peak of 0.067. Here in this inverse solution, the maximum peak should have been noticed at the first location and not the second. The reason why a higher peak was noticed at the second location is because the MU that produced this maximum peak (MU1) is positioned directly above MU6 at a more superficial location; it is masking the effect of MU6. Therefore, now one should choose which one of those two non-zero patterns should be taken to calculate Z_{max}, Z_{avr}, and E. Initially, we chose to take the non-zero pattern of the actual location and not the maximum location, and to calculate Z_{max}, Z_{avr}, and E from it. This algorithm will be defined as algorithm 1. It is important to emphasize here that those steps are performed as pre-processing steps and won't be involved in calculating the prediction time of the algorithm. In those pre-processing steps, we know where the 25 MUs that are going to be involved in the construction of the matrix $\boldsymbol{A}$ are located, and we choose which information we want to take from their inverse solutions to form the fitting curves. After this step, the algorithm becomes blind (we will not have any information about the MUs used to test this algorithm other than the EMG signal ($\boldsymbol{b}$) which is produced because of the activation of this MU). This EMG signal will be used with the dictionary (matrix $\boldsymbol{A}$) that was prepared in the pre-processing step along with the fitting curves.

To test the formulated fitting curve (the algorithm is blind now), 20 random test MUs were placed in the volume conductor model (one at a time), and the inverse solution $\boldsymbol{L}$ is calculated using a $\boldsymbol{b}$ recording of the contribution of the test MU alone and the $\boldsymbol{A}$ containing the contribution of the 25 MUs (this was repeated for the 20 different test MUs).

Then, the same information, Z_{max}, Z_{avr}, and E, was extracted from the inverse solution of each of the test MUs. Note that here Z_{max}, Z_{avr}, and E are calculated for the waveform containing the

maximum value in the inverse solution. For example, shown in Figure 2.26 is the inverse solution of a definite MU (the window size reflected by the X-axis here was randomly taken as 300 time-samples just for the purpose of the example, but later shorter window size of 40 time-samples will be chosen to reduce detection time). However, in such plot, you can notice on the Y-axis that each **200 time-samples** (5 different angles for each depth multiplied by the 40 time-samples that the firing of each MU takes as seen in the dictionary in Figure 2.22) should give information about **one of the 5 depths** we chose in our dictionary. In algorithm 1, we always choose the 1st 200 time-samples (to which the maximum value in the entire inverse solution will always belong to even if its actual location is in a different depth) to calculate Z_{max}, Z_{avr}, and E. Then, the value of each of those will be plugged in its corresponding fitting curve to check the (ρ, θ) it will yield.

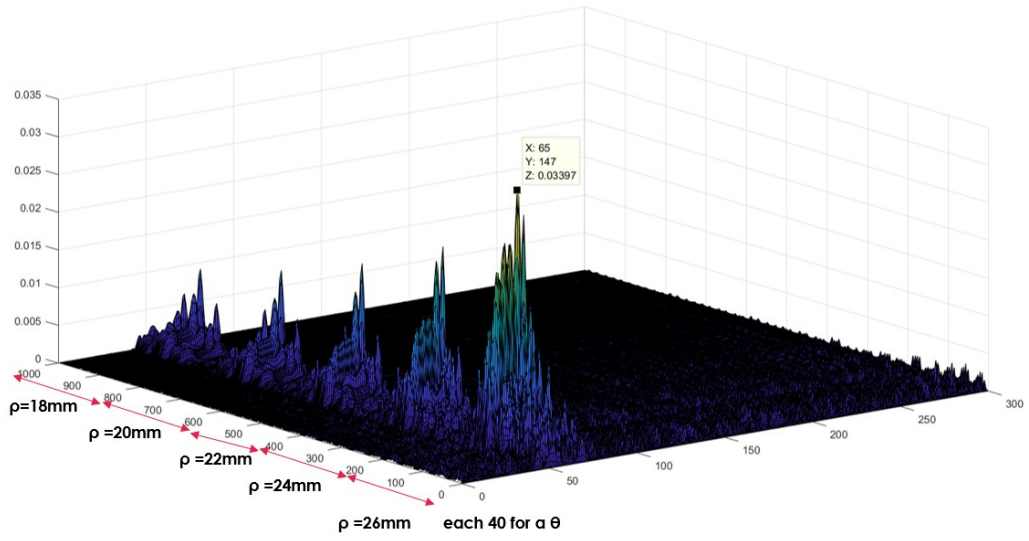

Figure 2.26: Example of the inverse solution of a random MU.

The steps of the algorithm are clarified in Figure 2.27 (steps 1 and 2 are in the pre-processing part while steps 3 and 4 are in the blind part of the algorithm).

Subsequently, after this is done for the 20 test MUs (for each of the 3 parameters), the RMSE for both (ρ, θ) was calculated for each of the 3 parameters. Finally, to be able to assess the performance of the algorithm and each of the 3 parameters and compare them, the mean and standard deviation (SD) of the RMSE for ρ and θ in each of the cases was then calculated.

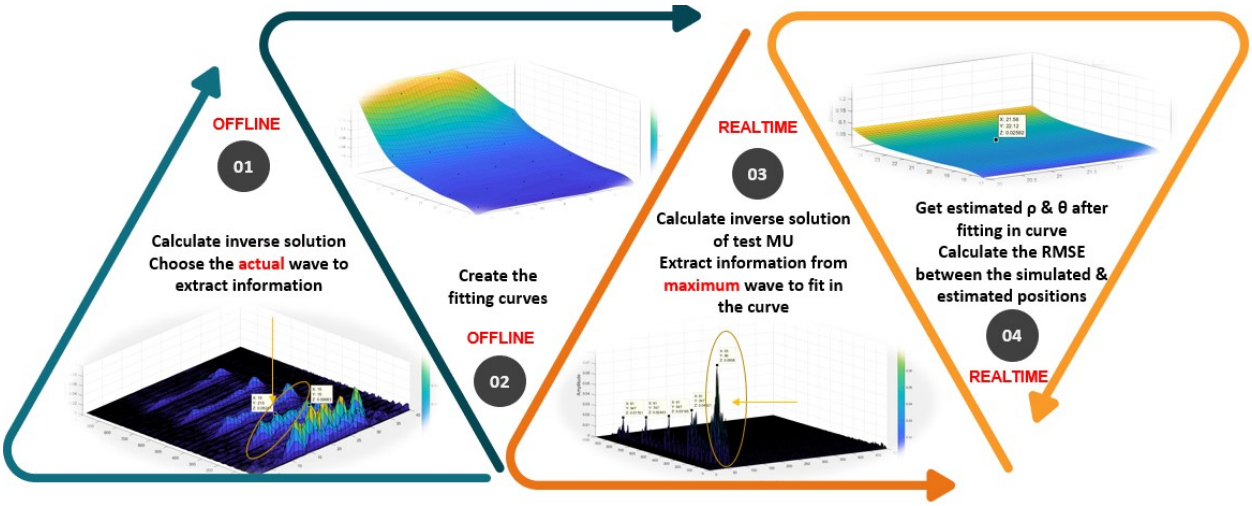

Figure 2.27: General steps to extract the data of the test point to be fitted in the 3D fitting curve for Algorithm 1.

The steps of the algorithm 1 that should be performed will be detailed below (note that the steps 1-4 below are done ahead of time using the 25 pre-determined MUs that we have information about):

1. Compute the inverse solution per MU as explained in the beginning of section 2.3.2 (***b*** will contain the contribution of the 25 MUs and a moving window will section ***b*** to include the firing of 1 of the 25 MUs at a time):

   for wi=1: n (n=length of ***b***/size of window)

   $$\hat{\boldsymbol{L}}_{\boldsymbol{wi}} = \boldsymbol{A}^{\boldsymbol{T}}(\boldsymbol{A}\boldsymbol{A}^{\boldsymbol{T}} + \boldsymbol{\alpha}\boldsymbol{I})^{-\mathbf{1}}\boldsymbol{b}_{\boldsymbol{wi}}$$

   end

2. Choose the $\hat{\boldsymbol{L}}_{\boldsymbol{wi}}$ reflecting the coefficients of the actual MU depth and not that of the maximum amplitude (we can choose this since this step is in the pre-processing step)
3. Compute max ($\hat{\boldsymbol{L}}_{\boldsymbol{wi}}$), mean ($\hat{\boldsymbol{L}}_{\boldsymbol{wi}}$), and energy ($\hat{\boldsymbol{L}}_{\boldsymbol{wi}}$) for each of the 25 MUs
4. Construct 3 fitting curves using the data yielded in the previous step
5. Test with a random MU and compute the 3D inverse solution curve ($\boldsymbol{b}$ will contain the contribution of this tested MU only):

   for wi=1: n (n=length of $\boldsymbol{b}$/size of window)

   $\hat{\boldsymbol{L}}_{\boldsymbol{wi}} = \boldsymbol{A}^{\boldsymbol{T}}(\boldsymbol{A}\boldsymbol{A}^{\boldsymbol{T}} + \boldsymbol{\alpha}\boldsymbol{I})^{-\mathbf{1}}\boldsymbol{b}_{\boldsymbol{wi}}$ end
6. Calculate max ($\hat{\boldsymbol{L}}_{\boldsymbol{wi=1:n}}$) and choose the $\hat{\boldsymbol{L}}_{\boldsymbol{wi}}$ to which this maximum value belongs
7. Calculate max ($\hat{\boldsymbol{L}}_{\boldsymbol{wi}}$), mean ($\hat{\boldsymbol{L}}_{\boldsymbol{wi}}$), and energy ($\hat{\boldsymbol{L}}_{\boldsymbol{wi}}$)
8. Fit the values max ($\hat{\boldsymbol{L}}_{\boldsymbol{wi}}$), mean ($\hat{\boldsymbol{L}}_{\boldsymbol{wi}}$), and energy ($\hat{\boldsymbol{L}}_{\boldsymbol{wi}}$) each in its corresponding fitting curve and record the estimated position (ρ, θ)
9. Compute the RMSE (Simulated ρ, Estimated ρ) and RMSE (Simulated θ, Estimated θ)
10. Repeat from steps 5-9 for the other tested MUs
11. Calculate mean(ρRMSE), mean(θRMSE), std(ρRMSE), std(θRMSE)

Due to possible higher errors in detection of deeper MUs (as it will be shown ahead), modifications of Algorithm 1 are proposed and put under test. For this purpose, we propose 2 modified versions (Algorithms 2 and 3). The common thing between Algorithm 1 and 2 is that both algorithms follow the exact steps required to form the 3D fitting curves (exact same pre-processing steps and both will have same fitting curves). Therefore, steps 1-5, listed for

Algorithm 1, are the same in Algorithm 2. The difference between the two algorithms is in the 6th step. Instead of using the data of the 1st pattern (with the highest peak) only, in Algorithm 2 the data of each of the 5 different peaks present (each represents a different depth and is 200 time-samples long as it was shown in Figure 2.26) is taken and the average of the five peaks is used (step 3 in Figure 2.28(a)). From this resulting average peak, Z_{max}, Z_{avr}, and E are computed and used in each of the 3 fitting curves.

It is good to mention here that Algorithm 1 will still be used for the detection of the superficial MUs. Algorithm 2 can be considered as hybrid that uses Algorithm 1 in case it was shown that the tested MU is superficial or uses Algorithm 2 if not.

The method used to check if the tested MU is superficial (without knowing its position) bears on comparing the 1st two peaks (corresponding to the 1st two depth levels on the Y-axis, which are 200 time-samples long each) in the inverse solution of the test MU. It was empirically observed, from our simulations, that if the MU was superficial, the difference between the first two peaks was significant.

As a threshold, if the difference is greater than 0.1, the MU is considered superficial, and Algorithm 1 is applied. Otherwise, if the difference is less than 0.1, the MU is not considered superficial, and Algorithm 2 is applied.

The other modification of Algorithm 1 will be called Algorithm 3. Like the approach followed in Algorithm 2, Algorithm 1 is going to be used for superficial MUs and for deeper ones Algorithm 3 comes in hand. The difference between Algorithm 3 and both Algorithms 1 and 2 is in the formation of the fitting curves. In Algorithms 1 & 2, the problem of masking was disregarded and not taken into consideration during the extraction of the data from the inverse solutions.

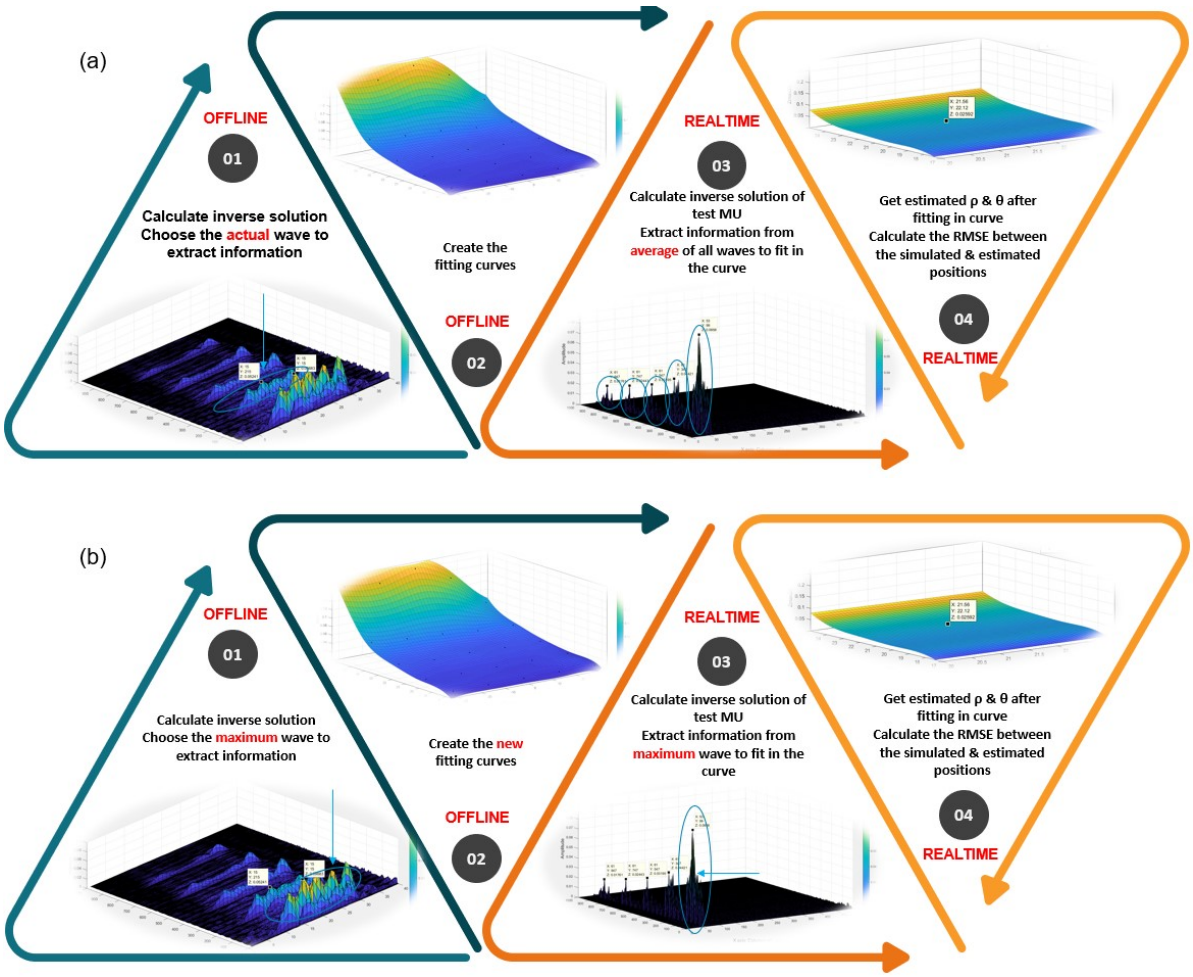

Figure 2.28: Steps of Algorithm 2 (a) and Algorithm 3 (b).

So, in the third algorithm, instead of taking the data of the actual peak, the data of the maximum peak will be taken regardless of if it reflects the information of the correct analyzed MU from the dictionary. This is shown in step 1 of Figure 2.28(b). However, when the inverse solution of a tested MU is calculated, we will go back in this algorithm to taking the data from the first highest peak only, and not the average of the 5 peaks as done in Algorithm 2 (step 3 in Figure 2.28(a)). This algorithm is also tested for the same 20 test points used in Algorithms 1 and 2 for the purpose of comparing their performance in the detection of the positions of unknown MUs, and the same calculations for RMSE, mean, and SD were performed. Finally, the entire procedure is repeated but with varying the noise level to evaluate its effect on the prediction accuracy of the

proposed algorithm. All the previous simulations in this section are done on signals affected by a realistic noise with SNR of 18dB of the simulated electrode grid.

2.3.3 Testing and results of CFB-MNE methods

The results yielded for the various algorithms and parameters will now be explained. After obtaining the ρ (mm) and θ (°) of a random MU, the RMSE between the actual and the yielded ρ and θ will be calculated. Then, the RMSE information are gathered for the entire tested MUs, and then the mean and SD for those are calculated to assess identification errors. The distribution of the 20 tested MUs along with the pre-defined MUs are plotted in Figure 2.29 where the x-axis reflects the θ value in degrees and the y-axis the ρ in mm. The pre-defined MUs involved in solving the initial inverse solution are plotted as purple circles and the ones that are used to test the various algorithms are plotted in dashed blue. Then, the mean and SD results for the 3 parameters for both ρ and θ, for the three different algorithms, are shown in Table 2.5.

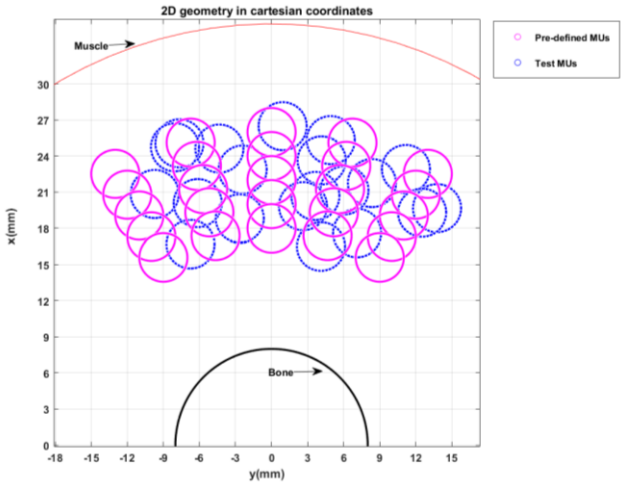

Figure 2.29: Distribution of pre-defined MUs (purple) and test MUs (blue).

Now, each of the 3 fitting curves is going to be used to predict the (ρ, θ) position of the tested MUs. For example, when using the fitting curve of Z_{max}, for Algorithm 1, the tested MU positioned at ρ=22mm and θ=16° yielded a Z_{max} of 0.034 (Figure 2.30(a)).

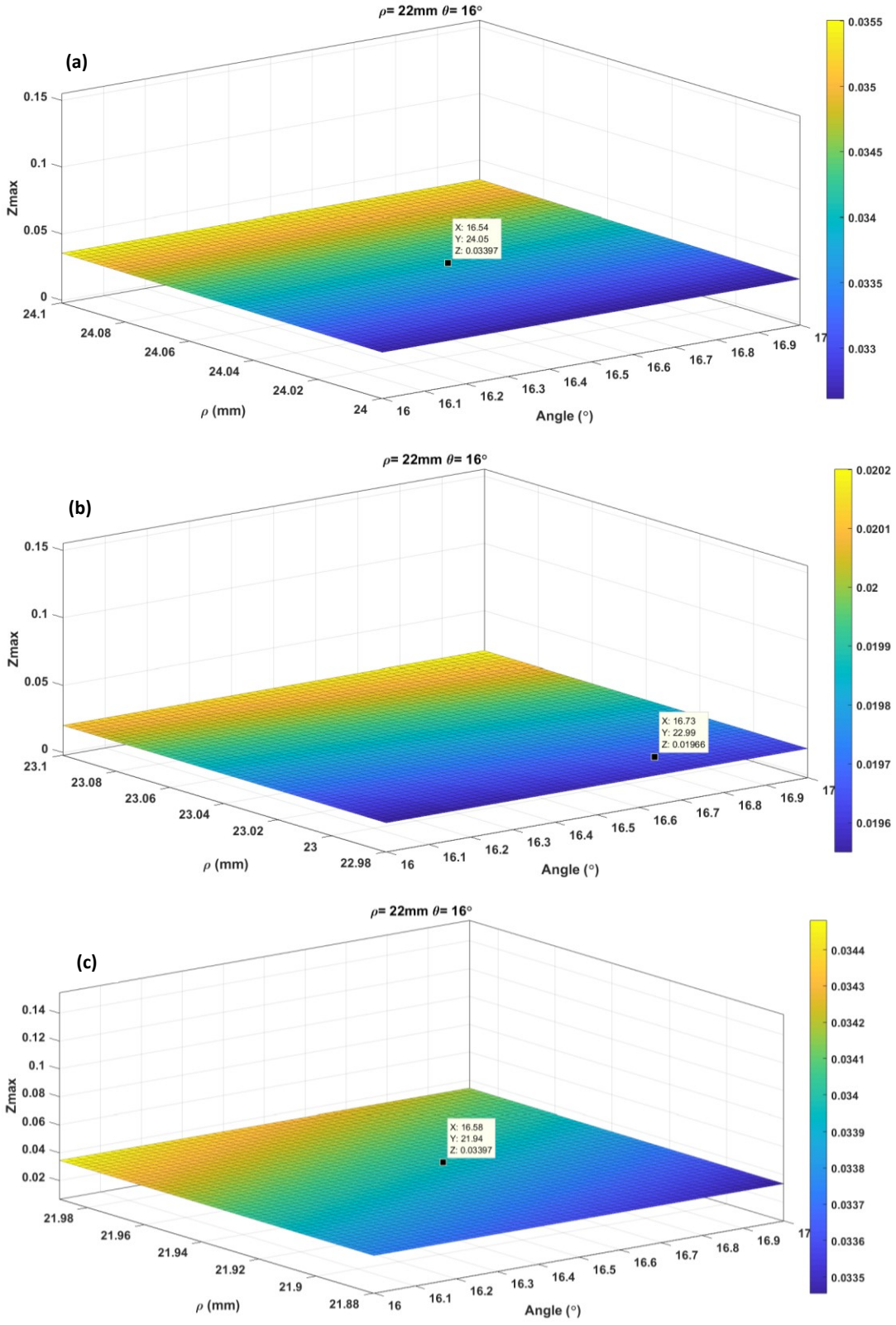

Figure 2.30: A zoomed plot of the fitting process used to estimate the position of a tested MU using Algorithms 1 (a), 2 (b), & 3 (c).

This will give an estimated position of ρ=24.05mm and θ=16.54° when fitted in its fitting curve as shown in Figure 2.30(a) (the plot is a zoom in taken from the original fitting curve shown in Figure 2.24). On the other hand, when using each of the fitting curves of Z_{max} for Algorithm 2 and 3, the tested MU, positioned at ρ=22mm and θ=16°, produced an estimated position of ρ=21.94mm and θ=16.58° as shown in Figure 2.30(c) for Algorithm 3. It also provides an estimated position of ρ=22.99mm and θ=16.73° as shown in Figure 30(b) for Algorithm 2. It is obvious that Algorithms 2 and 3 performed better than Algorithm 1. This will be further confirmed for the rest of the tested MUs summarized in Figure 2.31. This figure displays the results of all the algorithms for one of the parameters (Z_{max}). For illustration, the circle drawn in black is for bone, red for muscle, green for fat, and blue for skin. In Figure 2.31(a), where only a portion of the 2D volume conductor is shown, the simulated positions of the 20 random tested MUs (plotted in different colors as a complete circle), are plotted against the estimated positions (plotted in the same colors but with a dashed circle) for Algorithm 1. One can note the larger difference between the estimated and the simulated MU position for the tested MUs that are deeper (MUs in the bottom in black and yellow which are noted to by an arrow). As for the more superficial MUs (MUs in red and cyan which are noted by an arrow), a smaller difference was noticed. As mentioned earlier, the problem mainly lies in the correct detection of the depth. In contrast, the angular detection is less sensitive and more accurate. Meanwhile, it is noticeable how the difference (for deeper sources) was diminished for Algorithm 2, as seen in Figure 2.31(b) for the deeper sources (black and yellow). As for Algorithm 3, this difference further decreased, as displayed in Figure 2.31(c). An only exception was noticed when choosing a tested MU with a position more superficial than the pre-defined MUs (extrapolation from the fitting curve). This yielded higher errors (as shown for the green MU pointed at by an arrow).

(a)

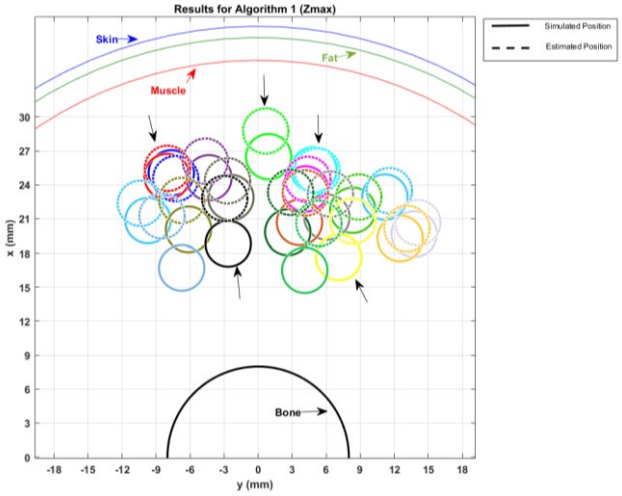

(b)

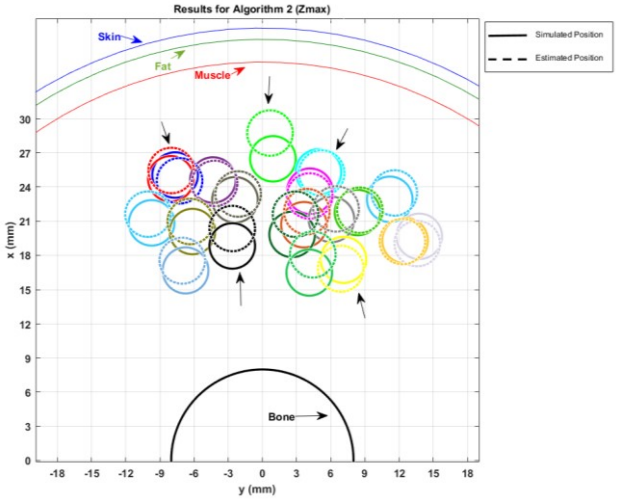

(c)

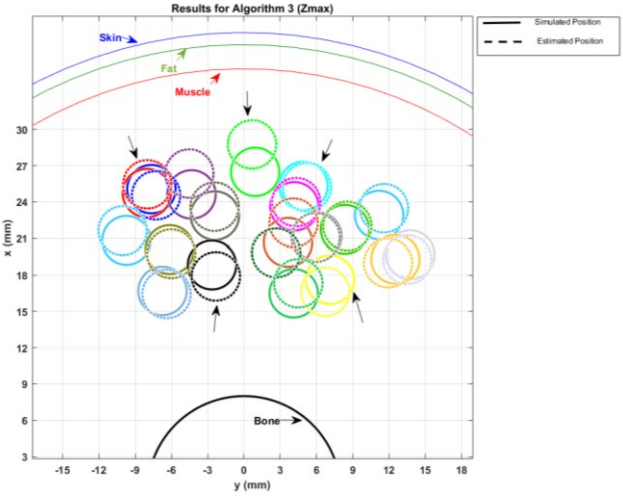

Figure 2.31: A comparison between the simulated and estimated MU positions using Algorithms 1 (a), 2 (b), & 3 (c).

Therefore, the increase of the number and surface repartition of predefined MUs (dictionary) should give a better precision and the increase of surface covered by those predefined MUs will give a better spatial resolution. This was also confirmed by the results shown in Table 2.6. Results show that Algorithms 2 and 3 performed better than Algorithm 1 in the prediction of depth (ρ), and that the Z_{max} and Z_{avr} parameters produce a lower identification error, when compared to E, in each of the algorithms.This is reflected by the lower mean error and SD values obtained in Algorithms 2 and 3 for Z_{max} and Z_{avr} (lower than 1mm for both parameters in each of the 2 algorithms and higher than 1mm for all the parameters in Algorithm 1 during the estimation of ρ). Meanwhile, Table 2.6 also shows that when it comes to the angular detection, all algorithms produced an almost negligible localization error with a mean error value and SD of less than 1°.

Table 2.6: Mean and SD of the RMSE between the actual and obtained ρ (mm) & θ(°) of 20 test MUs for the 3 Algorithms (SNR 18dB).

		Algorithm 1			**Algorithm 2**			**Algorithm 3**		
		Z_{max}	**Z_{avr}**	**E**	**Z_{max}**	**Z_{avr}**	**E**	**Z_{max}**	**Z_{avr}**	**E**
Depth ρ (mm)	**Standard Deviation, SD:**	1.369	1.287	1.607	0.848	0.556	1.245	0.540	0.517	1.130
	Mean, $\bar{x}$:	2.007	1.897	2.185	0.700	0.729	1.1	0.560	0.669	0.944
Theta θ (°)	**Standard Deviation, SD:**	0.163	0.239	0.173	0.182	0.190	1.068	0.228	0.241	0.443
	Mean, $\bar{x}$:	0.264	0.309	0.314	0.317	0.277	0.672	0.250	0.268	0.402

Hence, we can say that either the Z_{max} or Z_{avr} parameter can be used when extracting data from the inverse solutions to create fitting curves. Moreover, after putting the 3 algorithms under test it was proven that both Algorithms 2 & 3 were the most successful in the localization with low errors for both ρ and θ with a slightly better performance for Algorithm 3 over Algorithm 2.

Furthermore, the tested algorithms seem to allow accurate and fast localization of MUs, where 16ms computational time, in the proposed simulation, were required for processing a sEMG signal window of around 20ms. This enables using those algorithms in real-time analysis. The proposed study was inspired by the work of Mesin [17] who was distinguished in the inverse problem approach that he followed. This is dictated in the form of a pre-determined simulated basis waveform matrix (dictionary) that can be prepared prior to applying the inverse problem. As for Mesin's work, in this study, the purpose was to develop a real time localization technique using HD-sEMG signals. However, the approaches and the end results are different. The key difference between the two studies done is that Mesin did not attempt to identify single MU position. Instead, he used an over-determined problem to obtain the average estimation of the depth of a group of MUs and not the depth of a single MU. In our approach, a regularized under-determined approach was applied on HD-sEMG signal recorded by a 2D grid of 4×4 electrodes. The proposed algorithms could identify single MUs positioning in a cylindrical muscle geometry. In addition, both superficial and deeper sources were also differentiated using a curve fitting technique for source localization in a relatively fast duration. Faster processing could be obtained using a more effective processor (the simulations were done on an OMEN by HP PC with a processor having the following specifications: Intel(R) Core (TM) i7-7700HQ CPU 2.80GHz, and 16.0 GB installed RAM), a compiled routine (instead of the MATLAB implementation which is used in this study), or by using shorter window lengths.

2.4 Comparison between different inverse methods

The described algorithms relied on the classical MNE inverse method framework. However, other existing methods had to be tested and compared with this method to check if there is another more superior technique that we should follow.

The other method that was tested is the sLORETA, since it is known for its minimized localization errors as explained in Chapter 1 [92]. The Z_{max} parameter and Algorithm 3 were chosen to compare the two methods (best combination).

The same computing steps were applied for the two methods and the same MUs with uniform random positions were used to test the performances. According to the obtained results, the sLORETA method also yielded promising results that are comparable to those yielded by the MNE method.

The performance of the two methods is depicted (boxplot of the localization RMSE error) in Figure 2.32. In Figure 2.32(a), the mean error of the localization of ρ in mm is plotted on the y-axis for method 1 (MNE) and method 2 (sLORETA) which are placed on the x-axis.

This is also expressed in the results shown in Table 2.7, where only a slight difference in the methods was noticed and both methods yielded localization errors of less than 1mm for ρ and less than 1° for θ with trivial differences in the computing time. This confirms that the proposed method, using MNE formalism, is efficient and pertinent for the localization of MUs using HD-sEMG signals.

Table 2.7: A summary of the source localization results for the MNE and sLORETA for both ρ and θ.

20 random MUs		**MNE**	**sLORETA**
ρ (mm)	Standard Deviation, SD:	0.540	0.493
	Mean, $\bar{x}$:	0.560	0.501
θ (°)	Standard Deviation, SD:	0.228	0.312
	Mean, $\bar{x}$:	0.250	0.202

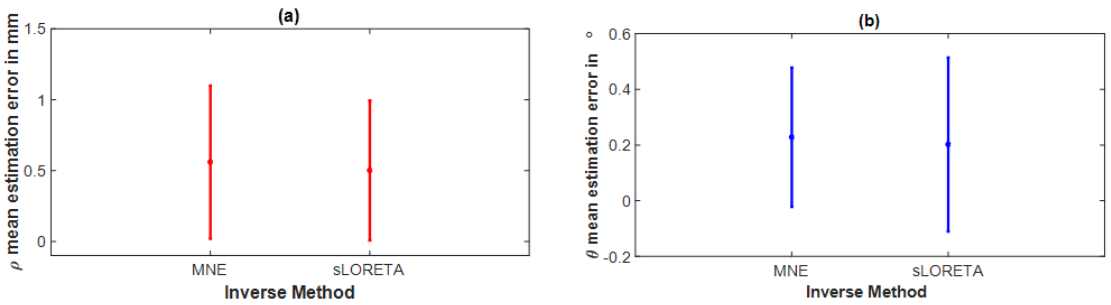

Figure 2.32: Mean and the standard deviation of the localization error for ρ (a) and θ (b) for MNE and sLORETA methods.

2.5 Conclusion

The present chapter focused on benchmarking an algorithm after calibration and testing before applying to real data. The innovation in this work is exhibited in the following: first, the model used to construct the waveform database (MU dictionary) is a realistic and accurate physiological model with complex geometry. This model calculates the HD-sEMG signals analytically, hence avoiding high computational times encountered in numerical models. Moreover, the number of MUs used in the simulations of the proposed algorithm is large and not restricted to only few MUs and the associated HD-sEMG measurements. This all allowed the creation of a predictive tool, based on a curve fitting technique derived from information extracted from the minimum norm inverse solution. After testing 3 algorithm versions and 3 parameters extracted from the 3D fitting curve, the best combination seems to be capable of not only reconstructing the signals produced by MUs within the muscle geometry, but also to accurately recover the position of those MUs within this muscle geometry. Moreover, this predictive tool (tested on simulations) can work in real-time. For the coming chapter, more complex source localization scenarios will be tested (including MUAP superposition), a sensitivity analysis which assesses the robustness of the proposed algorithm to definite changes (both in the anatomy and the detection system) will be performed, and finally a spatiotemporal identification based on realistic simulated MU recruitment will be tested and discussed.

Chapter 3

Method Evaluation and Applications

Contents

3.1 Introduction

The aim of this thesis chapter is to evaluate the robustness of the proposed methods and algorithms, described in chapter 2, by first testing the ability of the algorithm to estimate superimposed MUs (as opposed to chapter 2 where the methods were tested on single test MU at a time). This situation often occurs when several MUs are recruited at same time during the muscle contraction. After that, further complexity is introduced by testing whether the algorithm can estimate different types of MUs (such as those composed of FF or S fibers type). Another significant testing to be done on the algorithm is to evaluate its sensitivity to definite instrumental or physiological changes. For this purpose, a robustness analysis is to be performed in this chapter also. This will be done by assuming that there is a mistake between the dictionary constructed (simulated MU fingerprints) ahead of time and between the actual anatomy and associated setup. The purpose of this test is to check whether there is a need for a user case dictionary or a general dictionary is enough. Finally, since the limitation that we have is the inability to validate the algorithm proposed, due to the lack of an imaging technique that allows the dynamic imaging of MUs in action at different force levels, we will try to validate by simulation. This will be done by simulating MUs with realistic recruitment patterns. Not only the spatial recruitment of the MUs will be recovered but also the temporal recruitment. This simulated application prefigures possible real-time identification on experimental signals for diagnosis purpose.

3.2 Robustness analysis: generic or personalized dictionary

In the following section, it is beneficial to recall the steps of the algorithm that are going to be performed in each of the subsections below. The algorithm involves blindly taking the surface EMG signal (Figure 3.1(a)) generated by the participation of one or more MUs for each of the 16

channels. This signal is chopped into windows and each window from this signal is used (Figure 3.1(b)), with the dictionary prepared ahead of time and containing the participation of 25 preset MUs, to calculate the inverse solution. From each of the yielded inverse solutions (per window), the maximum amplitude is extracted.

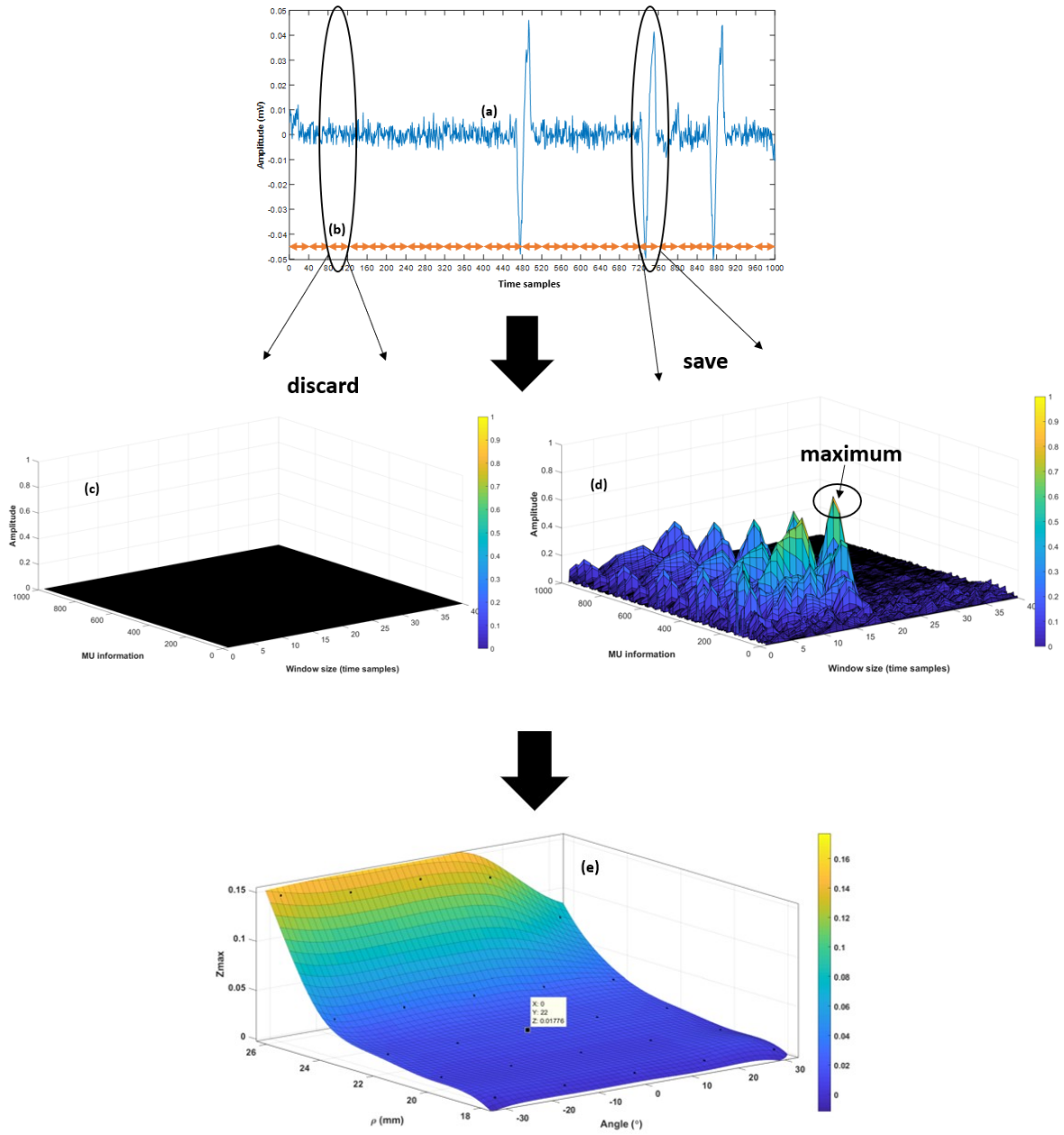

Figure 3.1: Steps of the algorithm: (a) the surface EMG signal, (b) the window size, (c) the discarded inverse solution windows, (d) the saved maximum amplitude in the windows where a MU fired, and (e) the fitting curve to estimate the location

If this maximum amplitude is above a definite threshold (Figure 3.1(d)) and is not considered as noise (Figure 3.1(c)). Note that the threshold (which is similar for all participating MUs given that the chosen muscle radius is the same) is chosen according to the lowest value of amplitudes participating in the creation of the fitting curve. Then, this maximum amplitude is taken and plugged in the fitting curve to check the MU position that it yields (Figure 3.1(e)).

The purpose of the work done in this section is to evaluate how robust is the proposed algorithm to certain factors that are thought to impact its performance. Among those are its ability to deal with superimposed MUs and its ability to differentiate between different MU types. Indeed, a robustness analysis was performed by supposing that there was an error between the actual investigated physiological system and the basis waveforms (dictionary) used to fit the HD-sEMG data.

The way that the algorithm deals with certain instrumentation uncertainties (such as the change in number of electrodes, their alignment, and varying the level of noise on the signals), and how it responds to certain anatomical or physiological uncertainties (fat thickness, fiber length, muscle radius, and CV) was put under test. For each test, a reference dictionary was considered and a change of one of the mentioned parameters was done at a time when simulating the tested MUs to be used with this reference dictionary and the positions were estimated.

It is noteworthy to mention that Algorithm 3 will be adopted for the rest of the simulations since it has proven superiority, in chapter 2, over other algorithms, and the Z_{max} parameter will be extracted from the inverse solution as an indicator for the position, since it also yielded the best results.

3.2.1 Methodology and results

3.2.1.1 Ability to estimate superimposed MUAPs

The position of the chosen MUs in this testing was also chosen according to a uniform random distribution, where 3 MUs that are randomly positioned are superimposed with a delay between the firing of each MU. The delay was also chosen to be between 3-5ms according to a uniform random distribution having a mean of 3ms and a SD of 2ms. Another factor to take into consideration in this testing is the moving window size, which was also varied between 10-100 time-samples (4.8ms-48ms) and the effect of this variation was studied. First, different window sizes during the calculation of the inverse solution were tested. The success of the algorithm to identify the spatial location of those three superimposed MUs was put under test. The mean and standard deviation of the RMSE between the actual position and yielded position for 20 different superposition combinations was eventually computed. Also, the duration taken by the algorithm when using different window sizes was also documented. However, the choice of the window size greatly affects the success of the algorithm. Though a window with a shorter duration is faster to process, the more we shorten the window size the more the probability that overestimation (same MU detected more than one time) error will occur. On the other hand, larger windows might lead to detecting more than one MU in the same window and one blurring the effect of the other (especially if the time delay between the discharging of the MUs is too short); this is known as underestimation. To further explain this, consider the two examples ahead. As displayed in Figure 3.2, a plot of the inverse solution of different windows, although results show the existence of 2 MUs (we can infer that from the significant amplitudes recovered from each of the windows), but in fact the same MU was counted twice since it is apparent that it started in the first window and continued in the other with almost the same normalized maximum

amplitude of 1. This is known as the problem of overestimation. Similarly, a window size which is too large will cause an underestimation (Figure 3.3), meaning that 2 or less MUs will be estimated instead of 3 (since the firing of more than one MUs are caught in the same window). So, the correct identification is dependent on both the window size and the delay. As a beginning, it was shown that below a definite time delay (4ms), it is impossible to differentiate between the 3 superimposed MUs (if their firing happened in the same window) while avoiding the problem of overestimation, and this resulted in a high localization error.

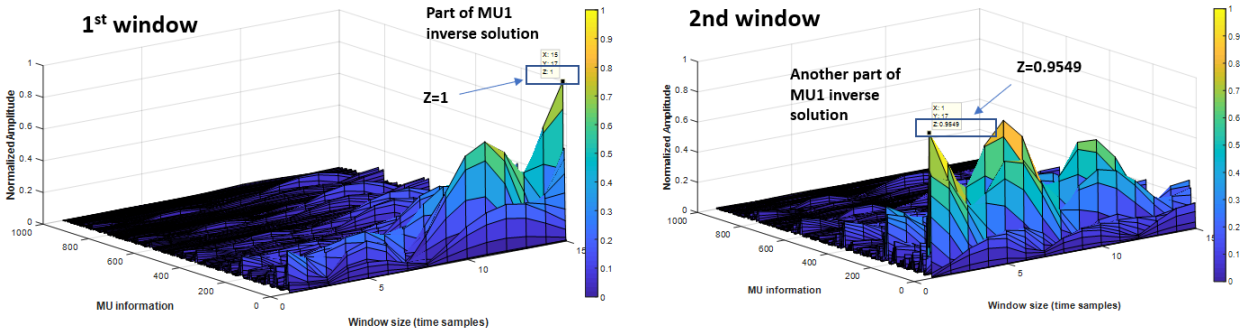

Figure 3.2: Example of overestimation with a window size of 15 time-samples (7.3ms).

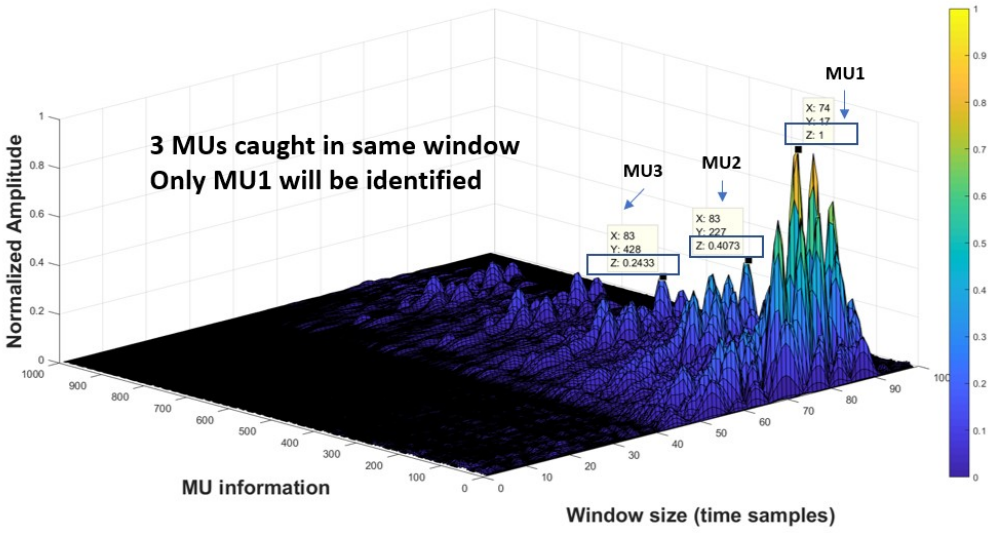

Figure 3.3: Example of underestimation, where 1 MU is estimated instead of 3 for a window size of 90 time-samples (44ms); this happens for short delays and for large analyzing windows.

This is shown in Table 3.1; when the time delay was around 3.9ms, the mean of RMSE of localization was 2.143mm for ρ and 1.342° for θ. This increased to 3.643mm for ρ and 1.424° for θ when the delay was even lower (3.2ms) (the results are marked in red in Table 3.1).

Therefore, the limitation of this algorithm is exhibited in small delays between the superposition of the MUs. Above this time delay, the algorithm registered a mean of RMSE below 1mm for ρ and below 1° for θ. However, this only works when the appropriate length of the moving window is chosen.

Indeed, results showed that an average window size of 20 time-samples (9.7ms) allows proper detection of MUs when delay is between 4-5ms with avoiding the problem of overestimation. Window sizes of 18, 20, and 22 were used with time delays of 4.23, 4.51, and 4.99ms. The results of each time delay for the 3 different windows were averaged and displayed in Table 3.1. As long as the delay between the firing of the superimposed MUs is greater than 4ms and as long as the window length is between 18-22 time-samples, the algorithm was shown to be effective. The results are summarized in Table 3.1 (marked in blue).

If the delay was larger, the algorithm will work given the fact that a window large enough is used. On the other hand, if the delay was brief, the window length must also be small enough to capture the MU. However, this might vary depending on the random discharging pattern of the MUs in nature, and the efficiency stated in this section might be different because one cannot expect which part of the MU firing will be in which part of the window; the process is very random (this is further demonstrated in the examples shown in the last section of this chapter).

As for the duration of the algorithm in detecting the MUs position, it was discovered that the larger the window size, the shorter the duration to process the entire signal, but more is the

duration per window. Since we are working in real-time, what we are interested in is the processing time per window.

Although the shorter the window the less the processing time inside the window (as shown in Table 3.2), the limitation in reducing the window size was described in the problem of overestimation. It was shown that for the appropriate window size and time delay for the algorithm to work well, the processing duration per window was around 15-16ms (marked blue in Table 3.2).

It is important to re-emphasize that the yielded results in this section were for simple superposition cases. In more complex situations, when the delay is even shorter than 3ms, even shorter window sizes will be needed and this will result in the problem of overestimation.

Therefore, the most appropriate window sizes in future more realistic examples will be chosen as the ones yielding the shortest processing durations (18-22 time-samples length which results in an appropriate processing time of around 16ms per window) while avoiding overestimation, since any other factor might change due to the complex and chaotic nature of the EMG signal.

Table 3.1: Superposition averaged results for window sizes ranging between 18-22 time-samples for various time delays (3 tests for each delay).

Delay (ms)	**RMSE**	
	ρ (mm)	**θ (°)**
4.99	0.487 +/-0.564	0.185 +/-0.272
4.51	0.745 +/-0.733	0.267 +/-0.334
4.23	0.934 +/-0.812	0.436 +/-0.476
3.94	2.143 +/-1.439	1.342 +/-0.762
3.22	3.643 +/-1.564	1.424 +/-0.987

Table 3.2: The source localization duration for the proposed algorithm for different window sizes.

Window size (time-samples)	**80** (39ms)	**40** (19.5ms)	**20** (9.7ms)	**15** (7.3ms)	**10** (4.8ms)
Duration per window	20.5ms	16.4ms	15.3ms	15.1ms	14.9ms

3.2.1.2 Ability to estimate different types of MUs

In this subsection, the ability of the algorithm to differentiate between two different fiber types (the FF and the S fibers) will be put under test. It is noteworthy to mention that for all the previous simulations done in this thesis, the fiber FF type was used. Therefore, the dictionary was created with MUs of this type, and the tested MUs whose position was to be retrieved were also of the same type. The success of the algorithm was tested assuming that all the MUs contain fibers of the same type.

Also, the exact same steps were repeated but instead of using FF MUs, S MUs were used. Similarly, the dictionary, the fitting curve, and the random test MUs were also all of the same type. However, in reality this is not the case. Hence, the aim of this section is to check how the algorithm will perform with a unified dictionary of one type of fibers only (either FF or S) whether the actual MU to identify is FF or S.

Accordingly, two different scenarios were put under test. First, the same dictionary (as well as the same fitting curve) that was produced earlier (using MUs of type FF) was used. However, the MUs of the unknown positions that were used were of a type S. After that, a new dictionary and a new fitting curve (composed using preset MUs of type S), and the MUs with unknown positions that were used to test of the algorithms were of a type of FF. As an example, consider

the following scenario: suppose that we have two different dictionaries prepared ahead of time; one of type FF and the other of type S.

Now, we have in hand the surface EMG signal detected at the electrode grid and we want to know the position as well as the type of fibers used to produce such a signal. The question here is: will this algorithm be able to give the correct position and type given using either one of the two dictionaries knowing that the MU creating the surface EMG signal is of a type S?

For this purpose, for scenario 1, 20 MUs of random unknown positions and consisting of S fibers were used to test the algorithm. Then, the mean and SD of the localization errors were calculated to assess how close the detected position is from the actual one. The same approach was done in scenario 2 but with reversing the type of fibers. The dictionary was of a type S and the random test MUs were of a type FF. For instance, if we have a random MU of an unknown position and fiber type, the surface EMG signal set due to this MU will be used with dictionary 1 (of type FF) and then with dictionary 2 (of type S).

Results showed that a MU of type FF, when used with a dictionary of type S, gives a position more superficial than it actually is, and when used with a dictionary of type FF gives accurate position. Hence, an FF MU could either be correctly seen as an FF MU in the correct position, or as a S MU in a more superficial position. For further explanation consider the following example; a MU of FF type positioned at ρ=23mm, θ=21° will be detected as: A MU of type FF and position ρ=23.62mm, θ=21.21° (which is the correct option since we used the correct dictionary type) or a MU of type S and position ρ=24.8mm, θ=21.6° (which is the wrong option since we used the S dictionary type).

Likewise, results showed that a MU of S type can either be correctly seen as a S MU in the correct position, or as an FF MU in a deeper position.

A summary of the results yielded for the 20 random test MUs of four different cases will be displayed: using a dictionary of FF type with a MU of type FF, using a dictionary of FF type with a MU of type S, using a dictionary of S type with a MU of type FF, and using a dictionary of S type with a MU of type S. The RMSE results of the 20 MUs of random positions are shown in Table 3.3.

When the preset MUs in the dictionary and the actual active MUs are assumed to be of the same type (either FF or S), the RMSE for both ρ and θ were less than 1mm and 1°. Meanwhile, when the type of fibers in the dictionary was different than those in the actual system, the RMSE for ρ increased to around 1.2mm (the θ error was uninfluenced).

As mentioned earlier, when the dictionary containing MUs with FF fibers is used to solve the inverse problem of a random MU of a type S, this MU appears to be around 1.2mm deeper than it actually is. On the other hand, if the dictionary contains S fibers and used against an FF type MU, this MU appears to be around 1.2mm more superficial than it is (the error is almost doubled).

Table 3.3: A summary of the RMSE results for the change in fiber type.

20 random MUs		**FF in FF**	**FF in S**	**S in FF**	**S in S**
RMSE	**ρ (mm)**	0.560 +/- 0.540	1.206 +/- 0.587	1.261 +/- 0.476	0.495 +/- 0.111
	θ (°)	0.228+/- 0.250	0.459 +/- 0.143	0.488 +/- 0.025	0.517 +/-0.213

Eventually, what can be done to get more accurate results regardless from the dictionary being used is to get the average of the RMSE from both dictionaries and by that the mean error will decrease and will be around 0.9mm for ρ (which is acceptable even if we did not know which dictionary to use).

This section put light on the benefits of personalized identification with MU type but pointed out the complexity related to compensatory effect between MU type and its depth.

3.2.1.3 Instrumentation uncertainty

In this subsection, the effect of the technical problems/limitations that might occur during experimental measurement was studied. The following parameters were changed one at a time (OAT approach): the amount of Gaussian additive noise (with a SNR which was varied between 12 and 18dB), the change in the number of electrodes in the measuring grid (32 electrodes versus 16 electrodes), and the misalignment of the detection grid with respect to the fibers (0°, 5°, 10°, and 30°).

3.2.1.3.1 Noise addition

The first parameter whose effect to be studied is how the amount of noise added to the signals will affect the ability of the algorithm to do proper source localization. Note that here, the dictionary is constructed with MUs whose corresponding MUAPs are contaminated by a noise with a SNR of 18dB (often observed in experimental signals).

Then 20 MUs of random unknown positions are used with this dictionary but once the signals of those MUs were contaminated by a noise level with a SNR of 18 dB, 15dB, and then 12 dB respectively.

What is notable in the yielded results is that the amount of noise scarcely affected the performance of the algorithm, unlike what usually happens as we increase the noise level (reasons discussed in the discussion section). For instance, in Mesin's work [20], when the levels of noise were high, the algorithms gave higher errors.

Mesin concluded that the effect of the noise on the identification process was influential for SNR equal to 15dB or lower [20]. This was not noticed when we increased the noise levels. A comparison between the localization results for the 3 levels of noise is listed in Table 3.4.

Table 3.4: A summary of the RMSE results with an added noise of 18dB, 15dB, and 12dB for both ρ and θ.

20 random MUs		**18dB (dictionary level)**	**15dB**	**12dB**
RMSE	**ρ (mm)**	0.560 +/- 0.540	0.621 +/- 0.569	0.712 +/- 0.522
	θ (°)	0.228 +/- 0.250	0.442 +/- 0.223	0.232 +/- 0.217

For instance, the mean value for the RMSE of the (ρ,θ) prediction, in the presence of a mean SNR =15dB, was 0.621mm for ρ and 0.442° for θ (for Z_{max} parameter using Algorithm 3). Meanwhile with the presence of a mean SNR=12dB, the mean values of the RMSE were (0.712mm, 0.232°).

Indeed, the error in detection of the depth increases as the noise level increases, but this increase is insignificant. Graphically, Figure 3.4 shows the mean and SD values of the localization for each noise level. This seems to indicate that the proposed inverse approach is relatively robust against noise. This assertion must be validated in further studies.

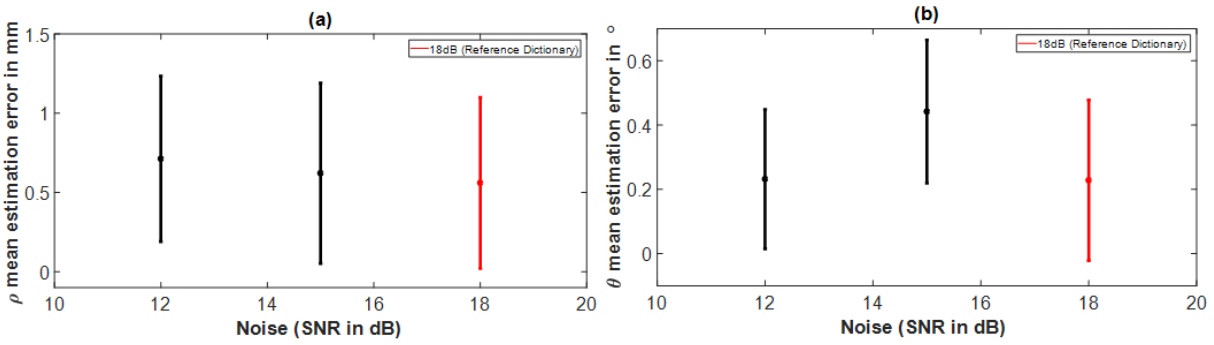

Figure 3.4: Results showing the mean and the standard error of localization of ρ (a) and θ (b) for the noise parameter. The bar in red in each graph indicates the reference condition (dictionary).

3.2.1.3.2 Change in number of electrodes

For all the simulations done previously, a 4×4 electrode grid with an IED of 8mm was used. Here, the number of electrodes was increased (in the θ direction) and an 8×4 electrode grid with an IED of 8mm. Hence, the area coverage of the electrode grid was increased. The purpose here is to check the influence of increasing the number of electrodes on the localization error and on the processing time. For this purpose, the entire steps of the algorithm were repeated with the larger electrode grid.

What was notable about the results yielded using this electrode grid is that the information contained in the inverse solution is more reflecting the actual position of the MU than it did when using the smaller grid. From the 3D plot of the inverse solution of a random MU, where we used to extract the maximum amplitude and use it to estimate the position from the fitting curve, now we can gain extra information, other than only the maximum amplitude, that can further confirm the position yielded by our algorithm.

This thing was absent when using a smaller grid. As a demonstration consider the following example: consider a random MU which is positioned at ρ=22mm, θ=16°. The algorithm will be applied to try to predict the position of the MU to see if it matched the actual position. A

comparison between the inverse solution content yielded when using 16 and 32 electrodes will also be shown. Previously, when 16 electrodes were used, from the 3D inverse solution plot, which is yielded by using the dictionary containing the contribution of 25 pre-determined MUs and the surface EMG signal from this random MU, two pieces of information were of interest. First, the maximum amplitude value in this inverse solution was used and fitted in the 3D fitting curve to predict the position. Also, the Y-coordinate information hold some information about the position too (as it will be shown ahead). As shown in Figure 3.5, the yielded Y value was equal to 147.

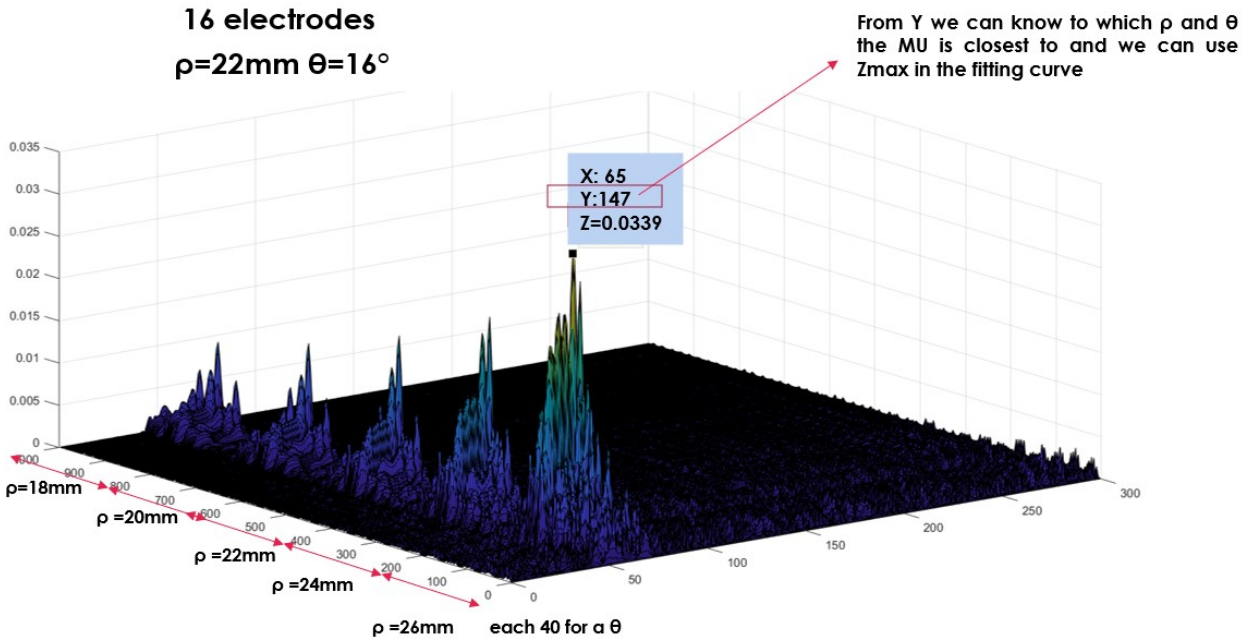

Figure 3.5: The 3D inverse solution of the random MU, using a 16-electrodes grid.

If we refer to our dictionary (shown in Figure 3.6), we can see that this value lies within the range 121:160. This range, as explained in the previous chapter, indicates a definite position, to which our random MU should be closest.

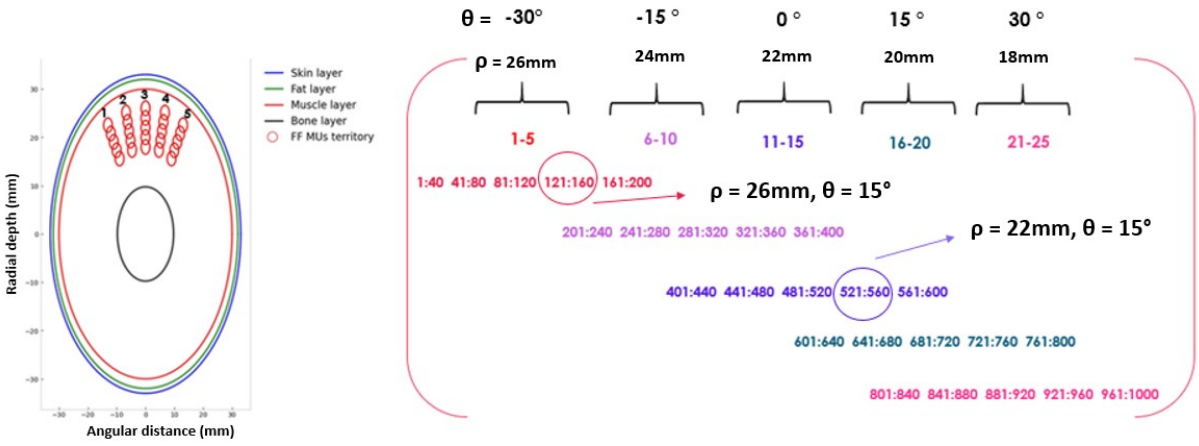

Figure 3.6: The position of the Y-coordinate information (circle in red) of the random MU in the dictionary used.

However, as shown in Figure 3.6, this range belongs to a MU positioned at ρ=26mm, θ=16°. Even though the θ estimation is correct, the ρ estimation is wrong and indicates a more superficial MU. This was explained previously as the problem of masking (the correct range should be between 521:560 which is circled in purple in Figure 3.6). This problem was tackled in the modification that was done in the algorithm as explained before and therefore, the only parameter we use from this 3D inverse solution is the maximum amplitude. This changed when using the 32-electrodes grid; as shown in Figure 3.7, the Y-coordinate value for the maximum amplitude change to 548 which lies within the range 521:560. This range corresponds to a MU positioned at ρ=22mm, θ=15° as shown in Figure 3.6 in the dictionary, which is a more accurate and closer to the actual MU. Also here, using the maximum amplitude value in the 3D fitting curve yielded accurate position values. Hence, by using an electrode grid covering a wider muscle surface area, additional information is prevailed in the inverse solution that can further confirm that the results of our algorithm are reliable. It is notable to mention that the algorithm (based on the maximum amplitude value and the fitting curve), almost performed similarly for 16 electrodes and for 32 electrodes, with a RMSE value less than 1mm for ρ and less than 1° for θ for both electrode grids, with a slight decrease in the ρ error values for the 32 electrodes.

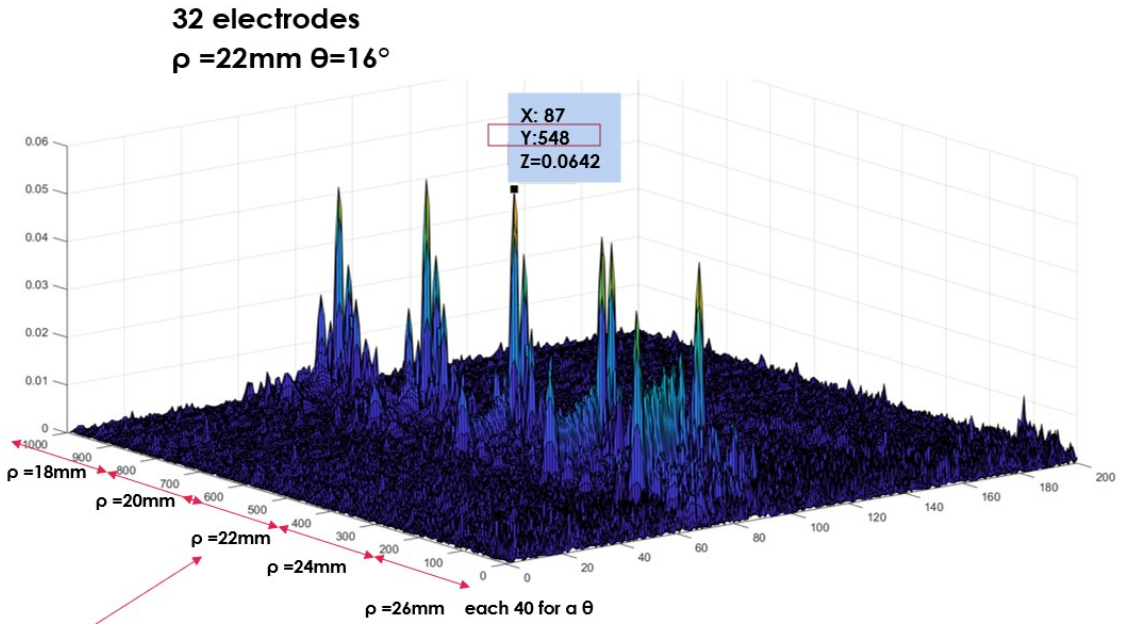

Figure 3.7: The 3D inverse solution of the random MU, using a 32-electrodes grid.

However, this was at the expense of time, where the processing time per window increased from around 15ms per window for the 16 electrodes to 19ms per window for the 32 electrodes, with the same computing conditions. This was tested for 20 MUs of random positions whose localization results are tabulated in Table 3.5 with a comparison with the 16 electrodes results.

Table 3.5: A summary of the RMSE results for 16 electrodes and 32 electrodes for both ρ and θ.

20 random MUs		**16 electrodes**	**32 electrodes**
RMSE	**ρ (mm)**	0.560 +/- 0.540	0.473 +/- 0.247
	θ (°)	0.228 +/- 0.250	0.424 +/- 0.149
Processing time per window		15ms	19ms

3.2.1.3.3 Misalignment of electrodes

For the reference dictionary in this study, the center of the electrode grid was 30mm (along the longitudinal axis) from the motor end plate, directed in an angular direction of 0° along the angular axis, and the electrode grid was aligned with respect to the fibers. However, we will assume that there exists a possible misalignment of the electrode grid, where it can be rotated by 5° and then by 10° with respect to the fibers. The same procedure was done for 20 MUs positioned according to a uniform normal distribution for the two different angles.

As shown in Figure 3.8 and reflected by the results listed in Table 3.6, there was a slight increase in the estimation errors for both ρ and θ (both were still less than 1mm and 1°) for the misalignment of 5 and 10°. The reduced effect of the angle changing is due to the small size of the grid used in this study compared to that one used by Mesin [20]. Mesin's results showed considerable effects at a misalignment of 10°.

Therefore, we further increased the misalignment to 30° to be able to notice the effect of this parameter. Indeed, the RMSE of ρ increased to above 1mm as shown in Figure 3.8 and Table 3.6 (as for θ it was not affected and it was nearly the same).

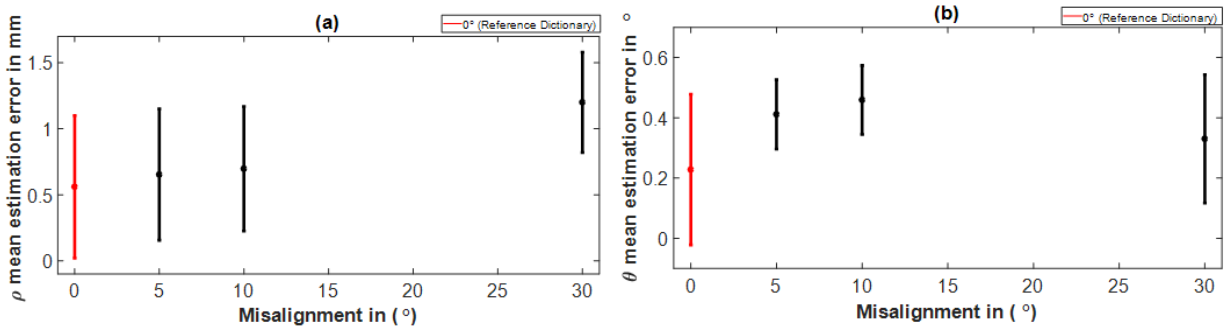

Figure 3.8: Results showing the RMSE of localization of ρ (a) and θ (b) for the misalignment parameter. The bar in red in each graph indicates the reference condition (dictionary).

Table 3.6: A summary of the RMSE for a misalignment of 0°, 5°, 10°, and 30° for both ρ and θ.

20 random MUs		0 °	5 °	10 °	30 °
RMSE	ρ (mm)	0.560 +/- 0.540	0.653 +/- 0.498	0.697 +/- 0.472	1.211 +/- 0.381
	θ (°)	0.228 +/- 0.250	0.411 +/- 0.115	0.459 +/- 0.1143	0.332 +/- 0.213

3.2.1.4 Anatomical and physiological uncertainty

The following subsection deals with how the algorithm will work with the presence of an anatomical or physiological difference in the analyzed neuromuscular system and the configuration used to create the MU dictionary.

This difference could be in the mean CV value (between 3 and 4m/s), in the muscle radius of the analyzed muscle anatomy (30mm and 40mm), in the fiber length (short fibers and long fibers), and in fat thickness (1, 2, and 6mm). Those parameters have been chosen in relation to their important impact on the sEMG signal generation.

3.2.1.4.1 Change in CV value

In this study, the dictionary is composed of MUs having a mean CV value of 4m/s. Then, 20 MUs of random unknown positions that are used to solve the inverse problem have a mean CV value of 3m/s. Results showed the influencing impact the mean CV has on the performance of the algorithm. The reason for this influence is that the surface EMG signal produced when the mean CV is 3m/s has a maximum amplitude significantly lower than when the mean CV was 4m/s. Hence, the maximum amplitudes in the inverse solutions will also be different for the two cases. As shown in Table 3.7, it is evident that the mean error of the localization of θ was not

influenced and was still less than 1°, but the localization of ρ increased to almost 2mm as the mean CV is decreased. Therefore, the mean CV and the depth are cofounding factors.

Table 3.7: A summary of the RMSE results for a mean CV=4m/s and a mean CV=3m/s for both ρ and θ.

20 random MUs		**CV=4m/s (dictionary)**	**CV=3m/s**
RMSE	**ρ (mm)**	0.560 +/- 0.540	1.838 +/- 0.846
	θ (°)	0.228 +/- 0.250	0.530 +/- 0.150

3.2.1.4.2 Change in muscle radius

Another anatomical parameter that might influence the performance of the algorithm in case of a mismatch between the dictionary and the studied neuromuscular system is the radius of the muscle that was assumed when constructing the MU dictionary (a muscle radius of 30mm was chosen for the dictionary).

However, suppose that we were working on a larger or smaller muscle radius. Will this influence the ability of the algorithm to correctly localize the MUs or will it be unaffected? Will a single dictionary be enough for any muscle radius, or should we use personalized libraries within the dictionary according to the subject anatomy? To answer those questions, it was assumed that the muscle radius is 40mm instead of 30mm, and the effect of this 10mm difference was studied.

The following criteria is going to be followed when choosing the locations of the MUs to be placed in a 40mm muscle radius: for instance, take the example of a MU positioned at ρ=17mm and θ=-10° (Figure 3.9 red filled circle) in a muscle radius of 30mm. In fact, this MU is positioned 13mm away from the muscle surface. Equivalently, in a muscle radius of 40mm a MU positioned 13mm away from the muscle surface will have a ρ=27mm and θ=-10° (Figure 3.9 empty red circle). In Figure 3.10, the MUAP of the MU in a 30mm muscle radius (ρ=17mm and θ=-10°) is plotted in blue and the MUAP of the MU in a 40mm muscle radius (ρ=27mm and θ=-10°) is plotted in orange. It is notable that the two signals are nearly the same (slight difference because of noise). Now, if the MUAP of the 40mm muscle radius (generated due to this MU: ρ=27mm and θ=-10°), was used with the 30mm muscle radius dictionary, a MU with a position of ρ=17.2mm and θ=-10.35° will be yielded. This is expected since the same MUAP was yielded from a MU positioned at ρ=27mm and at ρ=17mm.In the same manner, 20 MUs with ρ values between 4 to 14mm away from the muscle surface (placed each one at a time in a muscle radius of 40mm), were used with the dictionary (30mm) to solve the inverse problem. Indeed, this change yielded a RMSE equal to 9.44mm +/- 0.513mm for ρ and 0.201° +/- 0.201mm for θ. It is obvious that the radial depth error was gravely influenced while the angular error was not. Hence, the algorithm is greatly biased by the muscle radius and the choice of the appropriate dictionary is a must for successful localization.

However, this error is not a real (it is a methodological bias). If you refer to the surface and estimate the depth rather than rho (ρ), the estimation will work well. For this reason, computing the depth rather than rho for future works is recommended. Therefore, there is a relatively small effect of curvature variation for varying radius (30 to 40 mm).

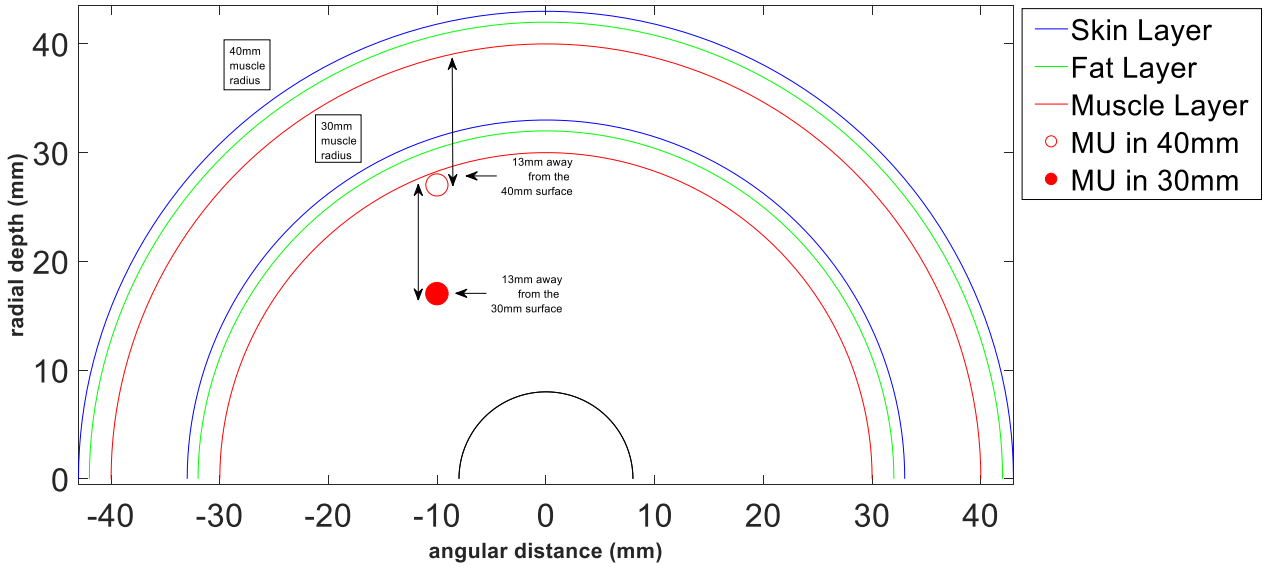

Figure 3.9: The position of a MU which is 13mm away from the 40mm muscle radius surface (empty red circle) and 13mm away from the 30mm muscle radius surface (filled red circle).

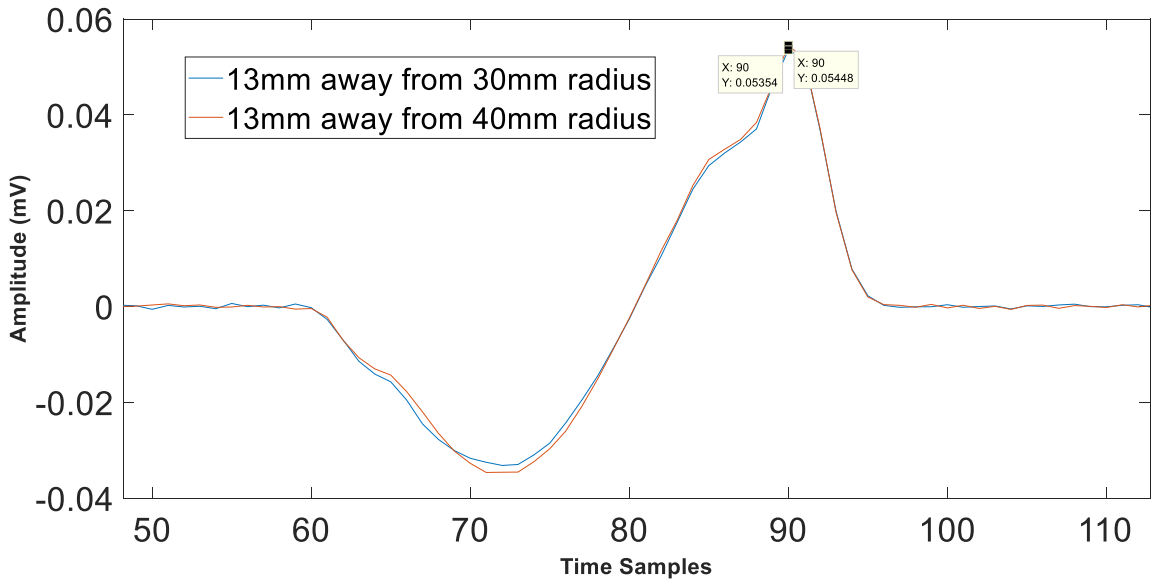

Figure 3.10: The MUAP recorded from a MU positioned 13mm away from a 30mm muscle radius surface (in blue) and 13mm away from a 40mm muscle radius surface (in orange).

3.2.1.4.3 Change in fiber length

Now, it will be assumed that there is a difference between the fiber length in the analyzed anatomy and between the adopted dictionary (150 mm fiber length). A shorter fiber length of 100 mm (i.e, a shorter studied muscle) will be assumed. In fact, the algorithm was biased by the

change in the fiber length and the RMSE of ρ increased from 0.560 mm to 1.134 mm (with a high SD value of around 1). This is shown in Figure 3.11 and Table 3.8.

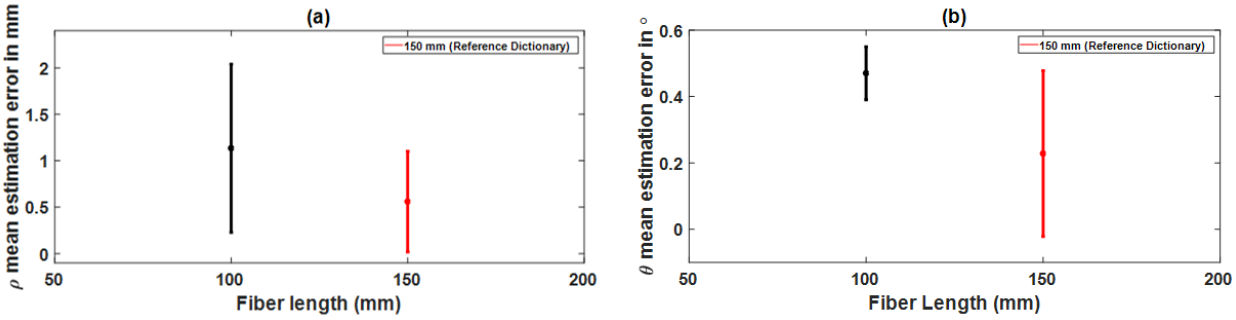

Figure 3.11: Results showing the RMSE of localization of ρ (a) and θ (b) for the fiber length parameter. The bar in red in each graph indicates the reference condition (dictionary).

The reason for the high SD value is that it was noted that from the 20 MUs used to test the algorithm, the superficial ones yielded low errors in the estimation of ρ (less than 1mm) but the deeper ones yielded a higher error (1-3mm). Those results were similar to the results yielded by Mesin [20]. In fact, the RMSE for the 10 superficial MUs was 0.338mm for ρ, and that for the 10 deep ones was 2.296mm.

This can be explained by the contribution of the non-propagating component of the MUAP that is affected by the fiber length and has important impact on its shape especially for deeper MUs.

Table 3.8: A summary of the RMSE for a fiber length of 150mm and 100mm for both ρ and θ.

20 random MUs		**L=150mm (dictionary)**	**L=100mm**
RMSE	**ρ (mm)**	0.560 +/- 0.540	1.317 +/- 0.905
	θ (°)	0.228 +/- 0.250	0.470 +/- 0.080

3.2.1.5 Change in fat thickness

The last parameter whose effect to be studied is the fat thickness. This parameter is important and related to the Body Mass Index (BMI). The fat thickness might vary from one individual to another, and it is important to check whether a general dictionary might work for any body mass index (BMI), or a personalized dictionary is needed. The fat thickness that was used to construct the dictionary was 2mm. Similarly, it will be assumed that there is a difference in the fat thickness of the studied muscle anatomy and between the dictionary. Fat thicknesses of 1mm and 6mm will be tested.

The overall radius of the volume conductor (skin, fat, and muscle) was preserved to 33mm. In the dictionary, when the fat layer thickness was 2mm, the muscle radius was 30mm and the skin 1mm (Figure 3.12(a)). For the 1mm fat thickness, the muscle radius thickness was altered to 31mm to preserve the overall radius. Meanwhile, when the fat thickness was increased to 6mm, this in turn was opposed in a decrease in the muscle radius to 26mm.

As a matter of fact, as shown in Table 3.9, the mean error of the ρ estimation was a bit influenced when the fat thickness was 1mm less. In fact, in this test, MUs appeared a bit deeper than they are since their electrical manifestations are crossing 1 extra mm of muscle even though they are crossing 1mm less in fat.

Hence, the muscle effect is superior to the fat effect (as an example consider the MUs in Figure 3.12 which are in the same positions in Figure 3.12(a) and (b)). This resulted in an overall RMSE of 0.601mm for ρ (which is still less than 1mm) and an overall RMSE of 0.288° for θ. However, when the difference between the dictionary and the studied physiological system was further increased and the fat thickness was assumed to be 6mm, the results were highly influenced.

The RMSE for ρ jumped to 1.765mm with a SD of 0.421 (the θ RMSE was not much influenced). Indeed, with more fat tissue but while preserving the distance that the signal will propagate in less muscle and more fat configuration as shown in Figure 3.12(b), the signal is penetrating from a more superficial area (since it is closer to the surface of the muscle).

Hence, the MUs will appear in a more superficial position than they actually are. Also, the yielded results were similar to Mesin's results, where the noticed effect on the algorithm was when the fat thickness increased up to 6mm [20].

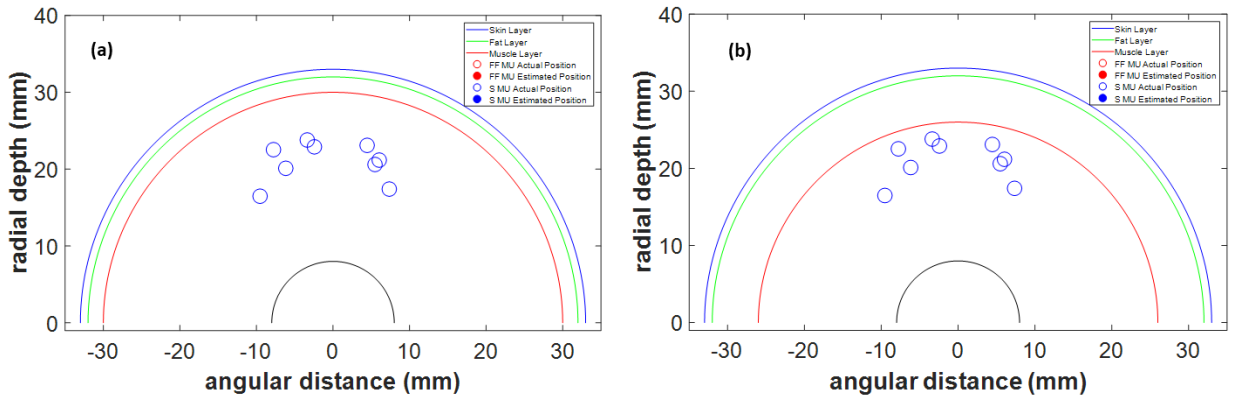

Figure 3.12: (a) Volume conductor used in the reference dictionary with 2mm fat and 30mm muscle radius, (b) 6mm fat thickness and 26mm muscle radius.

Table 3.9: A summary of the RMSE results for a fat thickness of 1, 2, and 6mm for both ρ and θ.

20 random MUs		**1mm**	**2mm(dictionary)**	**6mm**
RMSE	**ρ (mm)**	0.601 +/- 0.318	0.560 +/- 0.540	1.765+/- 0.421
	θ (°)	0.288 +/- 0.265	0.228 +/- 0.250	0.487 +/- 0.276

3.2.2 Discussion

Indeed, the results yielded in this section proved that there are certain key parameters that might change from one person to another and can be influential on the performance of the algorithm if it was different from the values present in our dictionary.

Signal to noise level and grid misalignment:

Certain parameters, like the amount of noise that might contaminate the signals, have shown to be not so much influencing. The reason for this opposes what is expected because this algorithm searches for the maximum amplitude in the 3D inverse solution even if the overall shape is affected by the noise level. However, most importantly, the noise is spread over the entire inverse solution plan and this is why the noise addition was not as effective as one would expect.

As for the grid misalignment, localization errors were also largely affected by misalignments of 30° and above. This is because the shape of the MUAPs is greatly altered in the electrodes that are aligned to the muscle fibers in this algorithm.

One of the possible methods to overcome the problem of misalignment is by altering the configuration of the electrode grid; decreasing the number of electrodes which are aligned with the fibers and increasing the density of those in the transverse direction [20].

CV influence:

Indeed, the algorithm was highly influenced when there was a difference in the mean CV between the dictionary and the studied neuromuscular system. Thus, the same dictionary cannot be used for assessing a subject with different mean CV as related to muscle fatigue or aging

[131, 132]. These two situations must be dealt with caution with probably personalized dictionaries simulated at lower mean CV.

Muscle radius:

Closely related to that, it was shown that the muscle radius (that might vary from one person to another depending on the person's muscle characteristics [133]) also affects the estimation process.

More precisely, the muscle curvature should affect the distance between the electrodes and the MUs, and by the way, will have a negative impact on the localization performance.

Fiber length:

Also, the fiber length showed to have an important effect on the algorithm performance. This is owed to the non-propagating component in the MUAP related to the end fiber effect which is present in a lower amount in superficial MUs than in deeper ones.

In fact, the non-propagating component content is lower in the dictionary of longer fibers (our reference dictionary was composed of longer fibers). This will lead to different MUAP shapes and to an increased error in localizing deeper MUs as it was shown [20].

Fat thickness influence:

Another affecting parameter was possible high fat thickness. This might occur for obese people (BMI>30 kg/cm2) with a high fat content within their bodies. We can conclude here that we cannot just use the same dictionary for a normal body weight person and for an obese person. Even for lower BMI (between 26 an 30kg/cm2), a personalized dictionary is also recommended since fat thickness and MU depth are confounding factors that bias the MU localization.

From the deep screening of the obtained results in this robustness analysis, one can conclude that personalized libraries within the dictionaries, incorporating influenced parameters, must be saved ahead of time. Depending on the characteristics and history of the patients (active lifestyle or a sedentary one, young or elderly, gender, BMI, muscle anatomy, etc..), and after the data about the patient are collected, the appropriate user-dependent libraries within the dictionary are chosen before running the algorithm.

3.3 Spatial and temporal identification of MU activation

In the previous testing of the algorithm, the activation of only one MU at a time was made, or the activation of several MUs but with one only being caught in a window at a time. In this section, more realistic recruitment patterns for the MU activation are adopted including both spatial and temporal recruitment. This recruitment pattern is created by the model we are using, and involve sophisticated cases of superposition.

The goal of this section is not only trying to identify the MU spatially (position localization), but also to know their temporal activation (the firing time of each MU). This last task is known in the signal processing community related to sEMG signals as the decomposition process. Several algorithms exist with specific approaches and performances [16, 134, 135, 136]. To illustrate the potential of the developed approach to perform spatiotemporal identification, three realistic simulated scenarios will be considered.

In the first scenario, 5 MUs, whose positions are shown in Figure 3.13(a), are firing over the duration of 3 secs with a recruitment pattern shown in Figure 3.13(b), where MU1 (the MU with the deepest radial depth) fired 49 times, MU2 40 times, MU3 34 times, MU4 26 times and MU5 21 times respectively, with a total of 170 discharges for the 5 MUs collectively.

The surface recording of the firing of those MUs is plotted in Figure 3.13(c) from one of the electrodes. Thus, not only 5 spatial locations should be recovered, but also 170 different firing times.

From the recruitment patter shown in Figure 3.13(b) and the signal in Figure 3.13(c), it is evident that complex superposition patterns (with very short delays between the firings of the MUs) are noted in this case. The next step involves applying a window over the signal shown in Figure 3.13(c) and using each windowed part of this signal with our dictionary (consisting of the 25 pre-determined MUs as usual) to calculate the inverse solution.

But since this is a blind test and we have no idea what the type of the existing fibers is, two dictionaries are used simultaneously, one constructed from S fibers and the other for FF fibers and the position of each MU using each dictionary is averaged to get the estimated position. By following this criterion, we can estimate the position regardless of the type of fibers.

The inverse solution of each window is saved and its maximum value is calculated. This maximum value will decide first if this window is discarded or kept (based on a threshold value which is preset according to the lowest value used in the formation of the fitting curves). If this window is kept, then the maximum value of this window is used to determine the position of the MU by referring to the fitting curve.

As for the calculation of the estimated discharge time, by knowing the length of each window (its duration) and its sequence, we can know the duration span of each window. The MU could have fired at any time in this window. However, since the window duration will be optimized, then we will consider that the MU fired somewhere in the middle of the window.

The chosen window size is around 19.5ms (40 time-samples) which is equal to the duration of each individual MU firing in the dictionary we established as explained in Chapter 2.

As discussed earlier in the beginning of this chapter, we do not want the size of the window to be large since this will not only increase the processing time, but it will also increase the probability of more than one MU being discharged in the same window.

This will in turn cause the inability to localize those MUs (underestimation error). At the same time, reducing the size of the window too much will chop the same MUAP into several parts and this will increase the probability of the overestimation error (as depicted in section 3.2.2.1), where the same MU will be treated more than one time.

It was shown in the previous section that as long as the delay between the firing of the superimposed MUs is greater than 4ms and as long as the window length is between 18-20 time-samples (8.7ms-9.7ms), the algorithm was shown to be effective. However, in the realistic recruitment of MUs increasing probability of superimposed MUAPs happens with a delay less than 4ms. Therefore, with such window durations, not all the MUs can be detected in the same window as it will be shown in the results of this section.

Also, when using the same window sizes that were tested in the superposition section previously, overestimation error is occurring (even though it was not faced in the simple cases) since in the realistic cases the signal is crowded with numerous firings of various MUs at different times. However, the window size that was chosen in this section was a window size that performed almost equal in the processing duration and at the same time gave the least underestimation in the same window. As it was recorded in Table 3.2, when the window size was 40 time-samples (19.5ms) the processing duration was also almost 16ms. This window size will be adopted in the

realistic recruitment patterns that will be tested in this section, as it was shown after numerous tests with realistic MU firings, it is the most convenient. Optimization procedure of the window length can be developed in future studies.

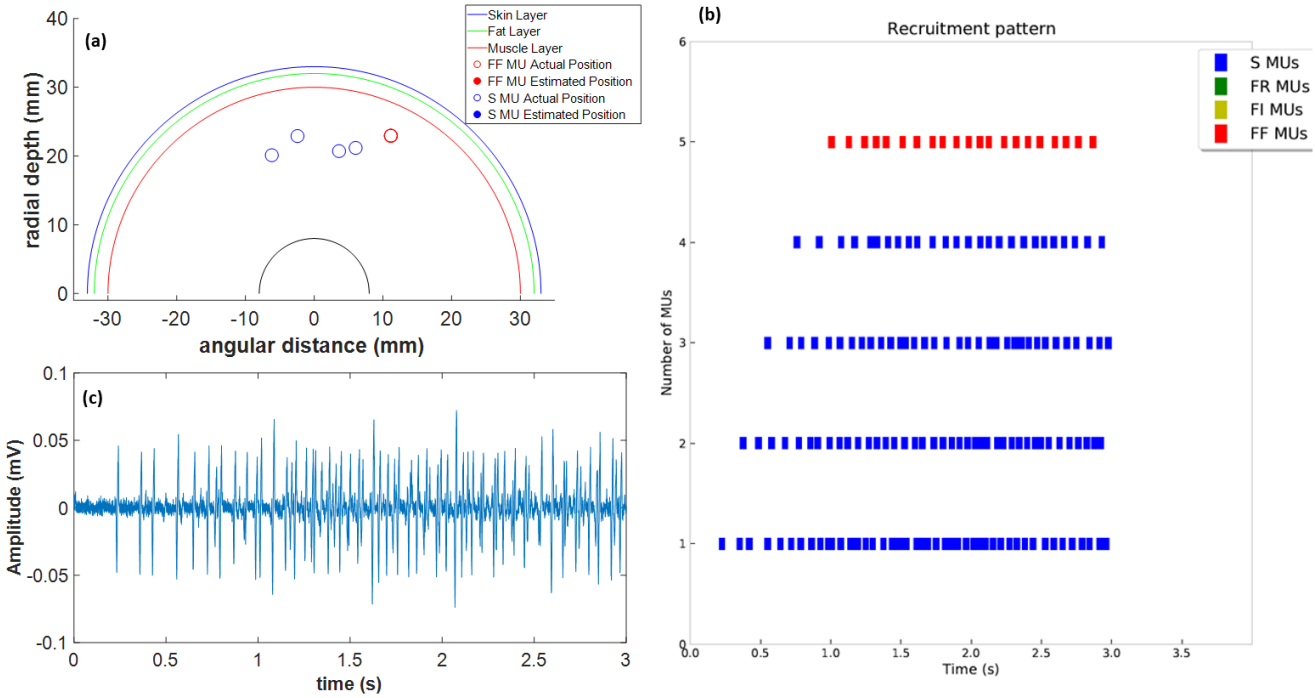

Figure 3.13: (a) the spatial distribution of the 5 MUs, (b) the recruitment pattern for each of the 5 MUs, and (c) the EMG signal resulting from the recruitment of the 5 MUs.

Then, while the inverse solution of each window is being calculated, a 2D image of this inverse solution will be displayed in front of the operator to further aid in only keeping the windows with significant information and discarding the noisy ones. For illustration purpose, consider one of the inverse solutions shown in Figure 3.14.

In this plot, the x-axis reflects the window size and the y-axis gives specific information about each MU (for details, see Chapter 2). The values at each x-y location are given a definite color according to the color bar shown to the right. As shown in Figure 3.14(a), the color yielded in this window is almost uniform and has a dark blue color indicating that this inverse solution was yielded when the window was passing through a noise part of the sEMG signal.

Therefore, such a window, if not already discarded due to the threshold value we set initially, should be discarded now. This will decrease the probability of falsely reading noisy windows as MU with low amplitude.

Meanwhile, if the inverse solution is the result of when the window was passing through a part of the sEMG signal where one or more MUs were being discharged, then we expect to see a pattern as that shown in Figure 3.14(b).

It is noteworthy to mention that the beginning and the end of the discharge of a MU are clearly observed in the inverse solution image. For instance, we can know from Figure 3.14(b) that only 1 MU discharged in this window.

However, it is not always that simple. To describe the complexity of the situation, consider the example shown in Figure 3.15, where the inverse solutions of two consecutive windows are plotted.

Figure 3.15(a) shows the start and end of the inverse solution of MU1, and the start of inverse solution of MU2. Since the maximum of the inverse solution of MU2 is in the same window with the inverse solution of MU1, and it is higher than all the values for MU1, only MU2 was detected and MU1 was missed.

Also, in Figure 3.15(b) the maximum value detected in the window after was for MU3. But we can see clearly that there was another pattern in the inverse solution image in the window in Figure 3.15(b) whose maximum was not taken into consideration since MU3's maximum was higher.

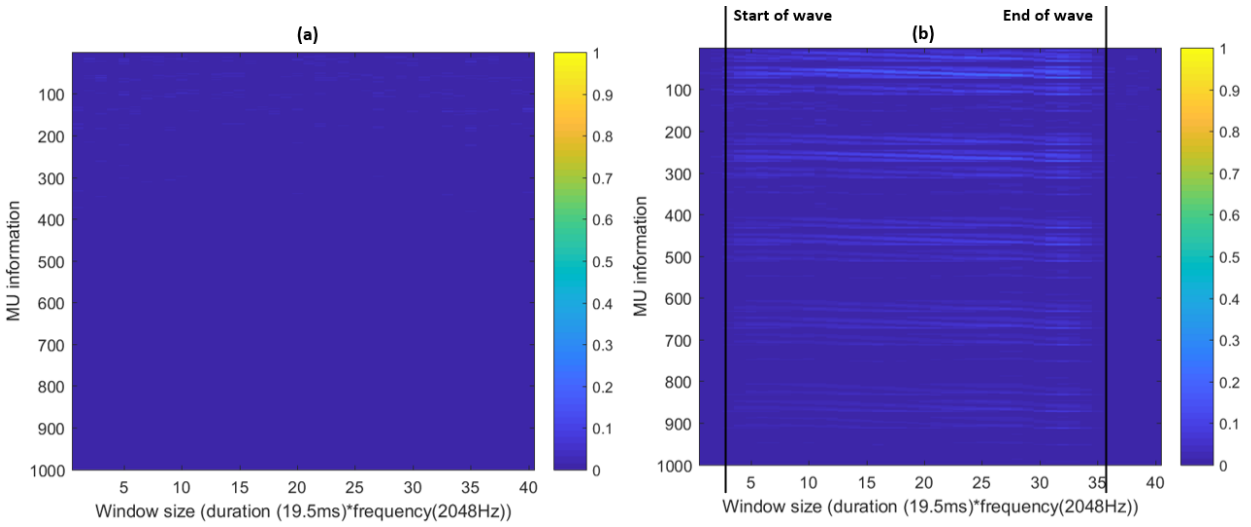

Figure 3.14: Example of two consecutive windows containing: (a) only noise information and (b) information about the firing of a single MU.

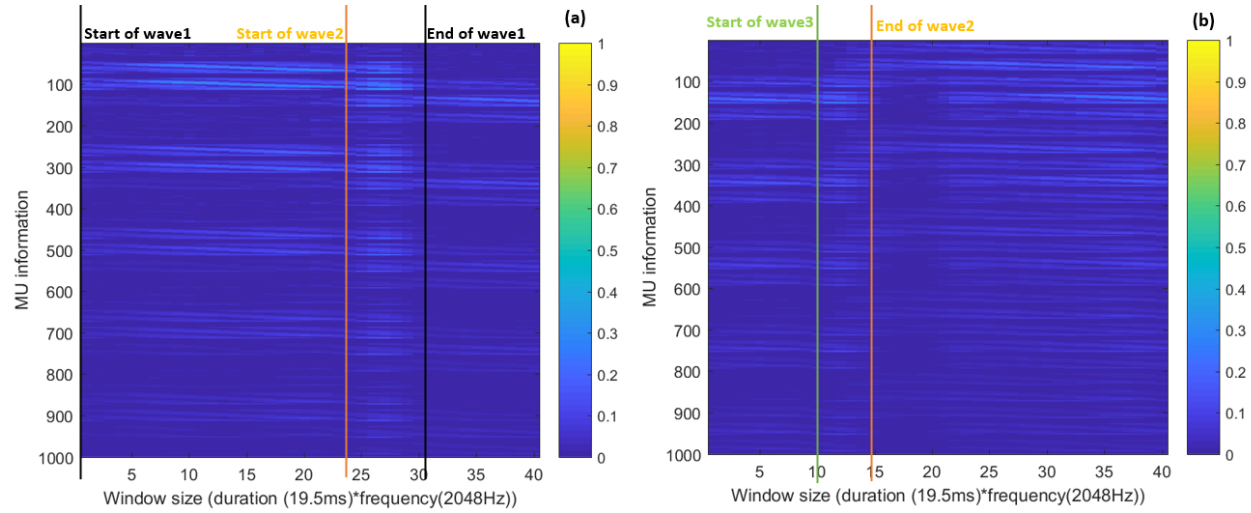

Figure 3.15: Example of two consecutive windows containing: (a) information including the superposition of MU1 and MU2 (b) information including the superposition of MU2 and MU3.

It can even get more complex as shown in Figure 3.16, where the inverse solution in that window includes a part of the firing information of MU1 including its maximum value, along with a big part of the firing information of MU2 including its maximum value also, and almost half of the firing information of MU4 with a maximum value higher than that of MU1 and MU2. So here, information of MU1 and MU2 are blurred and masked by MU4 which is detected alone in this window. However again, from those images we know that there are 3 contributing MUs in this window.

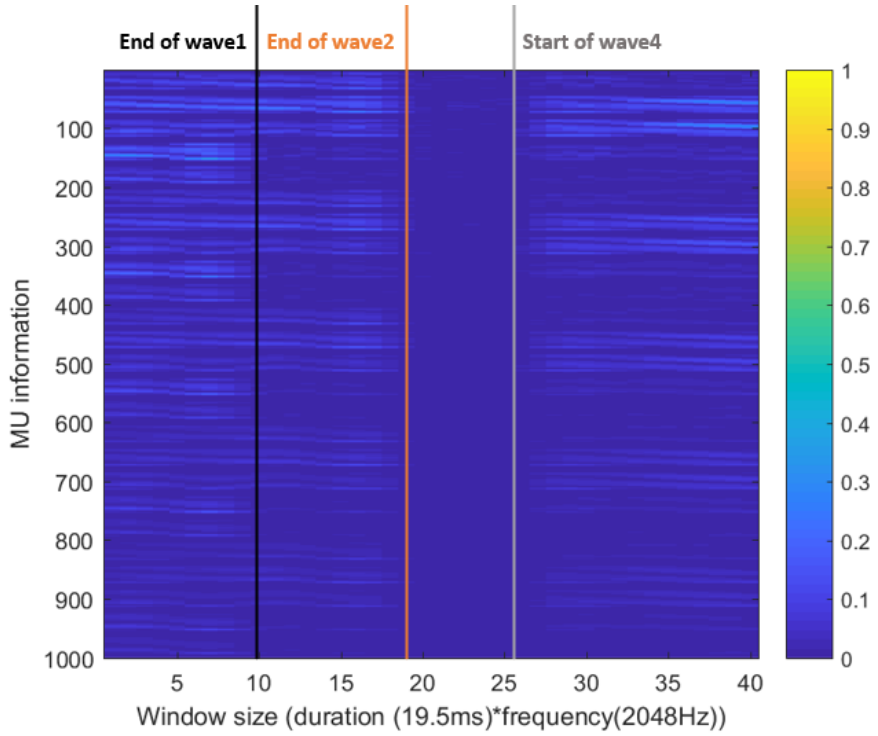

Figure 3.16: Example of a window containing information including the superposition of MU1, MU2, and MU4.

Eventually, the estimated spatial location (ρ (mm), θ (°)) is compared with the actual spatial location of all the MUs that were captured by the algorithm and plotted on a 2D plot of the cylindrical muscle volume.

Also, the estimated discharge time is compared with the actual discharge time for all the MUs that were also captured. The mean and SD of the RMSE for each MU spatial location is finally calculated, as well as the overall temporal discharge error (difference between the real firing time and the estimated one).

After that, in the second and third scenarios, the number of MUs is increased to 7 and then finally to 10 and the same steps are repeated to evaluate the limitations of the CFB-MNE method. The actual spatial distribution and temporal discharge for the MUs are shown for case 2 in Figure 3.17(a) and Figure 3.17(c) and for case 3 in Figure 3.17(b) and Figure 3.18(d)).

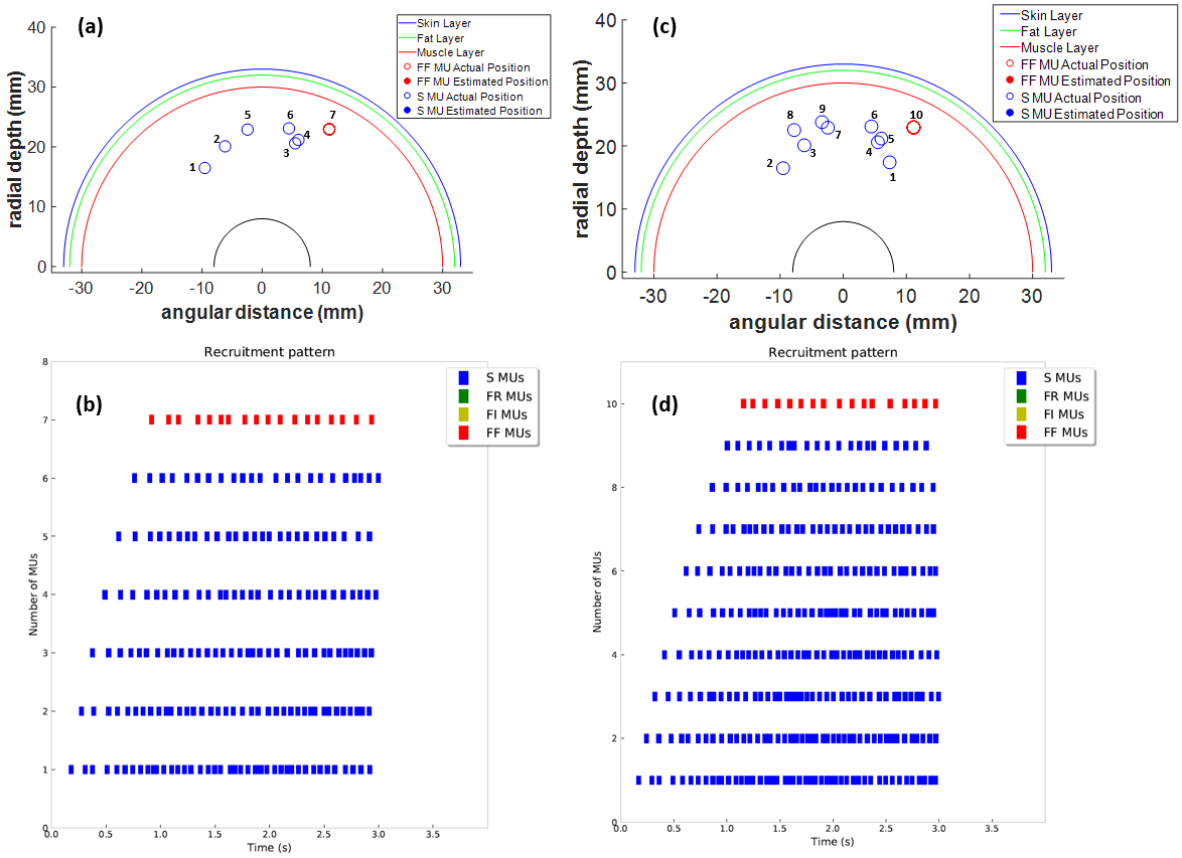

Figure 3.17: (a) the 7 MUs spatial localization in cylindrical coordinates, (b) the temporal recruitment pattern for the 7 MUs, (c) the 10 MUs spatial localization in cylindrical coordinates, (d) the temporal recruitment pattern for the 10 MUs.

In scenario 2, as shown in Figure 3.17(b), MU1 (the MU with the deepest radial depth) fired 41 times, MU2 38 times, MU3 34 times, MU4 29 times and MU5 26 times, MU6 23 times and MU7 18 times, respectively, with a total of 209 discharges for the 7 MUs collectively. Meanwhile, in scenario 3, MU1 (the MU with the deepest radial depth) fired 45 times, MU2 44 times, MU3 40 times, MU4 38 times and MU5 36 times, MU6 32 times and MU7 30 times, MU8 25 times, MU9 21 times, and MU10 17 times, respectively, with a total of 328 discharges for the 10 MUs all together as it is displayed in Figure 3.17(d). Eventually, after applying the algorithm on the 3 different scenarios, the following is computed: the estimated location for each MU (ρ, θ) and the estimated temporal discharge time (plotted and compared with the actual location and the actual temporal discharge), the average of the estimated positions for each MU

at different temporal discharges (plotted and compared with the actual location), the mean and SD of the localization error for each individual MU (plotted as error bars), the mean and SD of the localization error for all the MUs collectively (tabulated numerically), the mean and SD for the temporal discharge of the MUs collectively (tabulated numerically), and the percentage of success of the algorithm on each of the MUs (plotted as a bar plot).

3.3.1 Results

This section will present the yielded results after applying the algorithm on the 3 different described scenarios. As it was mentioned, the estimated location for each MU (ρ, θ) and the estimated temporal discharge time in each window was recorded and plotted against the actual ones. Then, those figures are collected and assembled in a video that can run and show us what is happening, one analyzing window after the other. As an example, consider Figures 3.18 and 3.20. In those figures, which deal with scenario 3 (the most complicated out of the 3 scenarios), a plot of the estimated localization results against the actual positions is done for the 10 windows that included the 1st firing of each of the 10 MUs. The selected windows show the information yielded for the 1st discharge of each of MU1 (Figure 3.18(a)), MU2 (Figure 3.18(b)), MU3 (Figure 3.18(c)), MU4 (Figure 3.18(d)), MU5 (Figure 3.20(a)), MU6 (Figure 3.20(b)), MU7 (Figure 3.20(c)), MU8 (Figure 3.20(d)), MU9 (Figure 3.20(e)), and MU10 (Figure 3.20(f)). In each plot, the title contains: the estimated temporal discharge, the temporal discharge error, and the localization error. For instance, it was estimated that MU1 discharged at t=0.186s and localized at ρ=19.33mm and θ=23.6° which scored a (0.45 mm, 0.6°) localization error and a 19ms temporal discharge error. Along to the images generated in Figures 3.18 and 3.20, in each window another image is also displayed in the video showing how many MUs discharged in each window and at which time instants (Figures 3.19 and 3.21). If those MU firings were

detected by the algorithm, their firings will be plotted in green and if it was missed it will be plotted in red. For instance, for MU1's first discharge, it fired alone in the selected window as shown in in Figure 3.18(a).

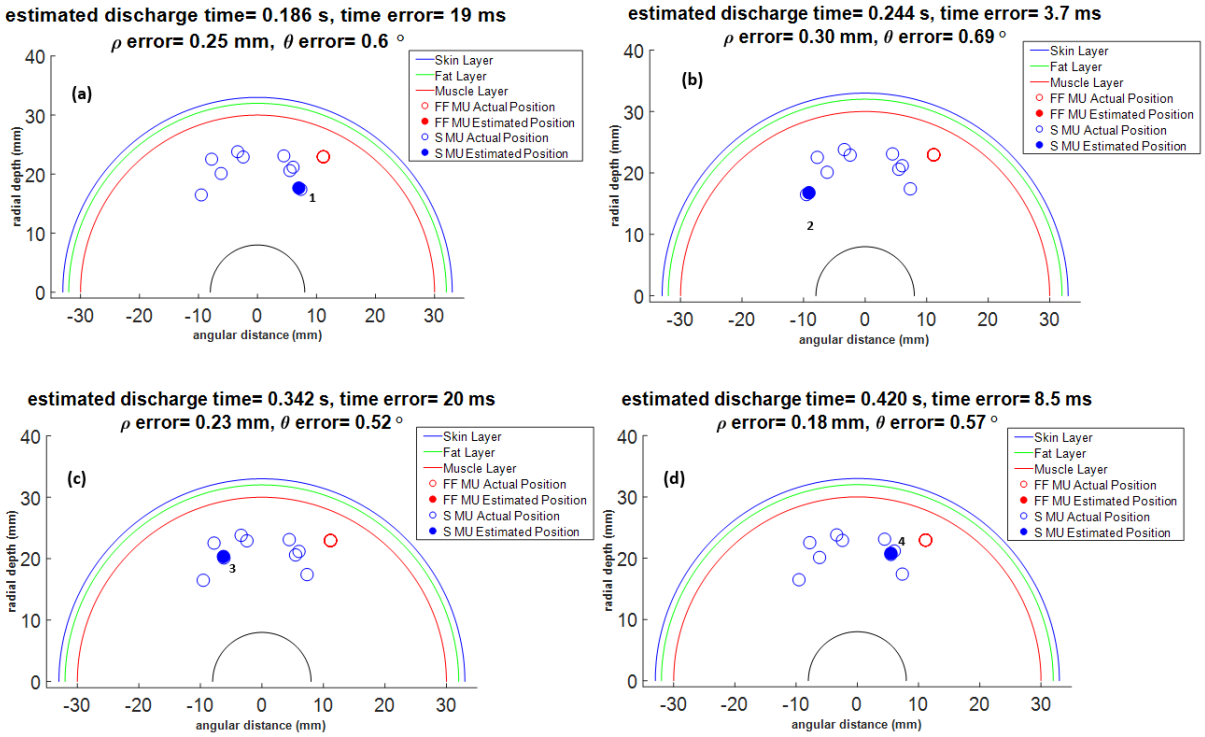

Figure 3.18: The estimated spatial and temporal information of the first firing for MU1 (a), MU2 (b), MU3 (c), and MU4 (d).

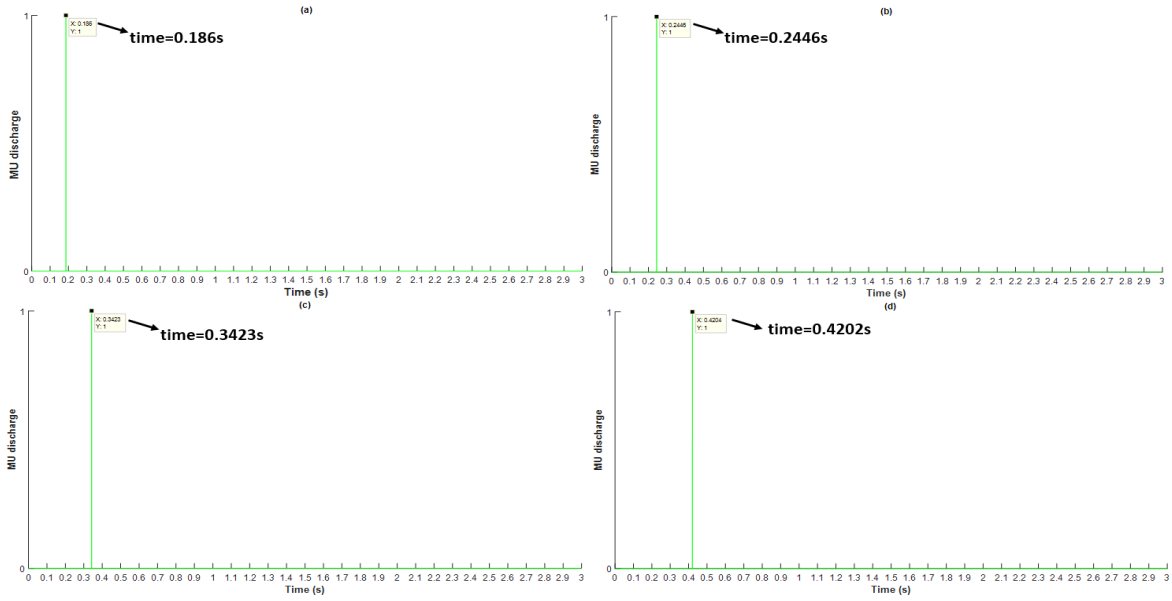

Figure 3.19: The estimated discharge times of the first firing for MU1 (a), MU2 (b), MU3 (c), and MU4 (d).

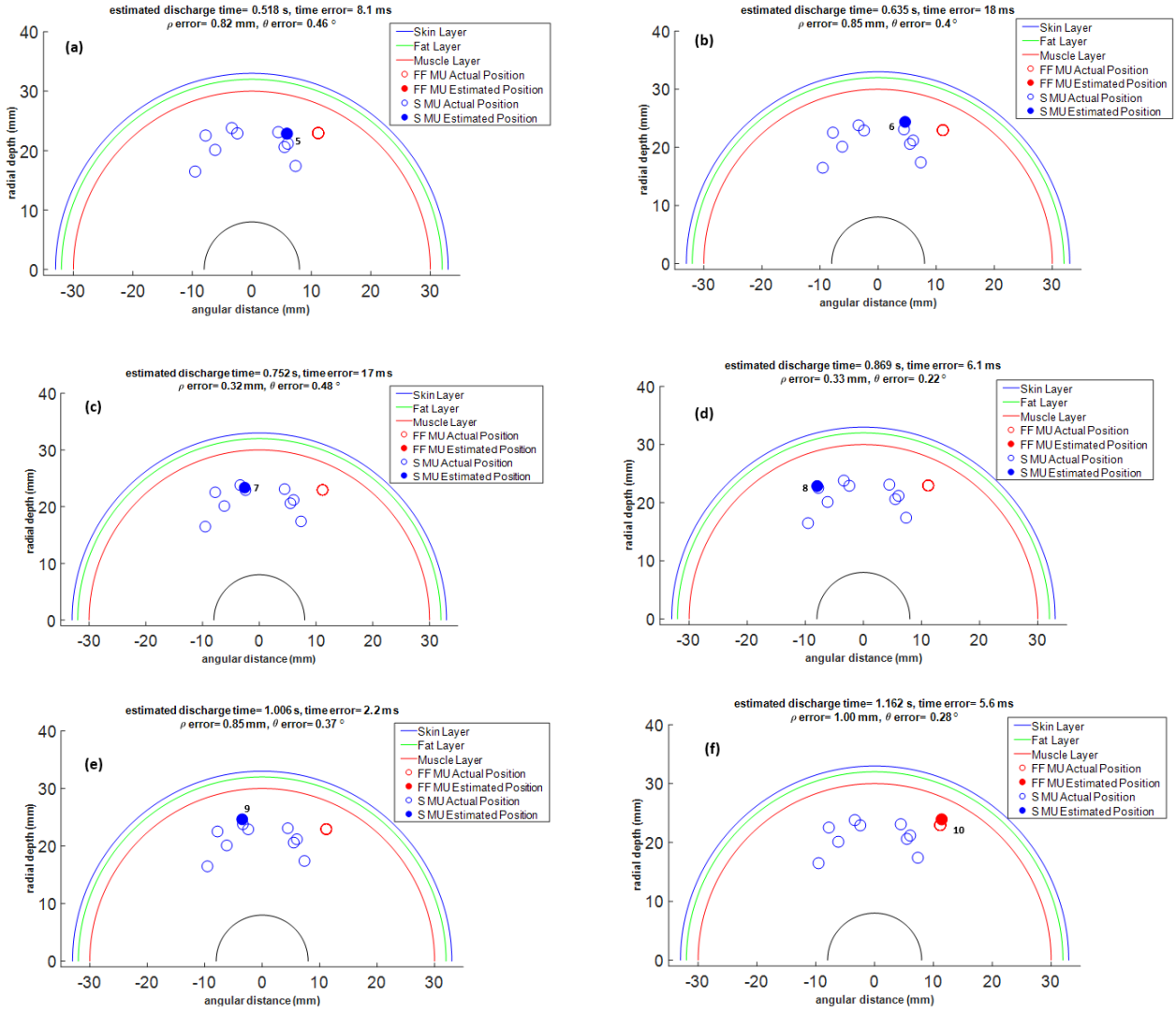

Figure 3.20: The estimated spatial and temporal information of the first firing for MU5 (a), MU6 (b), MU7 (c), MU8 (d), MU9 (e), and MU10 (f).

This methodology is also applied to the first temporal discharge of MU2, MU3, MU4, MU5, and MU6 whose 1st temporal firings are shown in Figures 3.19(b), 3.19(c), 3.19(d), 3.21(a), 3.21(b), respectively.

However, if we take the example of the 1st temporal discharge of MU7, MU8, MU9, and MU10 shown in Figures 3.21(c), 3.21(d), 3.21(e), and 3.21(f) respectively, one can see that there are firings from other MUs in the same window (3-4 MUs discharging at the same time in each of

the mentioned windows). The firing spikes of the MUs that were missed in the selected window are plotted in red and the recognized spikes in green.

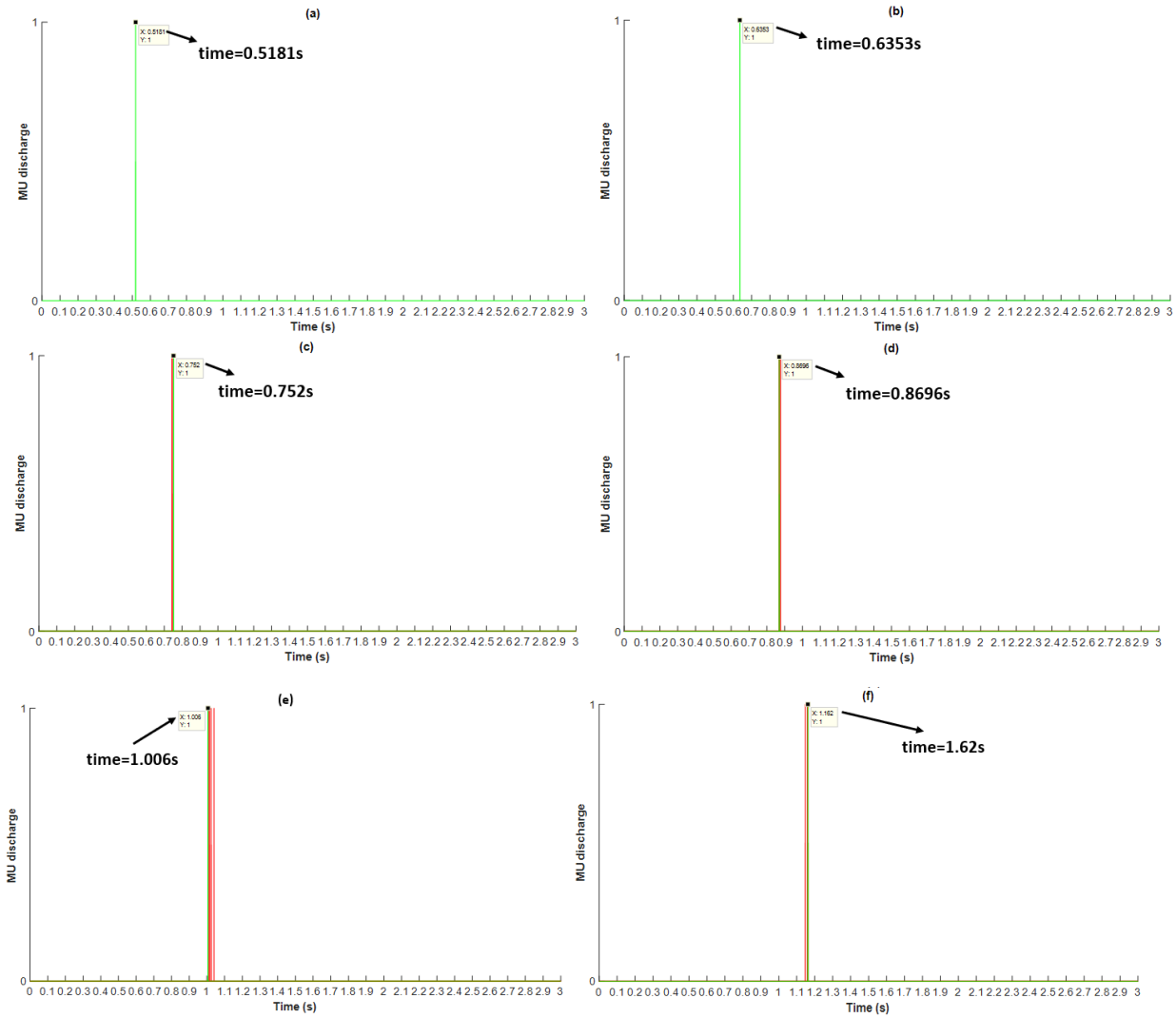

Figure 3.21: The estimated discharge times of the first firing (in green) for MU5 (a), MU6 (b), MU7 (c), MU8(d), MU9 (e), and MU10 (f).

As a detailed example, considering the case of the 1st discharge of MU7 (MU7 estimated position during the 1st discharge is shown in Figure 3.22(a)), we will see in Figure 3.22(b) that MU7 was detected at t=0.752s. However, two other MU firings were missed in the same window (those plotted in red which are in fact the 4th discharge of MU4 and the 3rd discharge of MU5). A zoomed plot of the discharge times is shown in Figure 3.22(c).

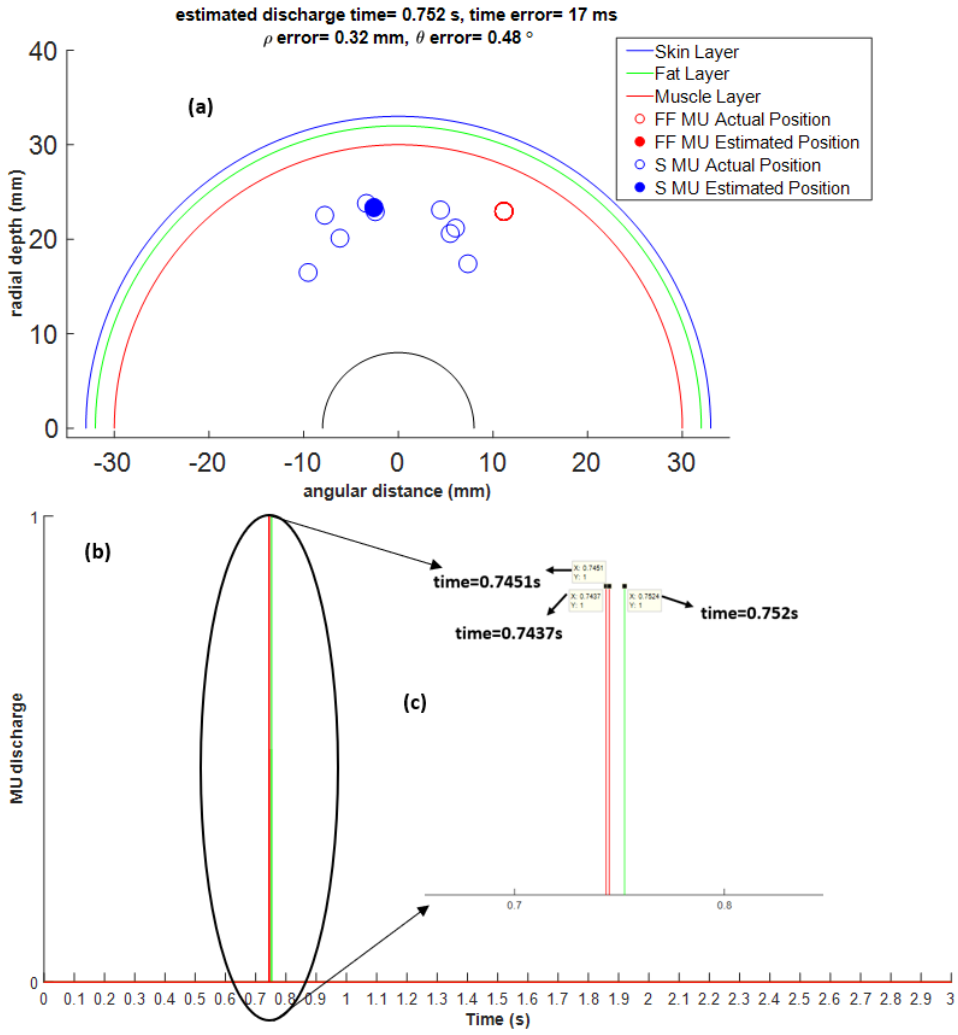

Figure 3.22: The estimated spatial (a) and temporal (b) information of the first firing for MU7, with a zoomed view of the discharge times (c).

To summarize the localization results, the mean and SD of the localization error (for each of ρ and θ) for each MU in each scenario, are calculated and graphically shown error bars in Figure 3.23. In this figure, the center of each bar indicates the mean value of the error and the width of the bar indicated the SD (+/-).

The red bars reflect ρ errors and the blue ones reflect the θ errors. Even though two dictionaries were used and the error was averaged, in scenario 1, all the 5 MUs had a RMSE of less than 1mm for ρ (Figure 3.23(a)) and less than 0.5° for θ (Figure 3.23(b)).

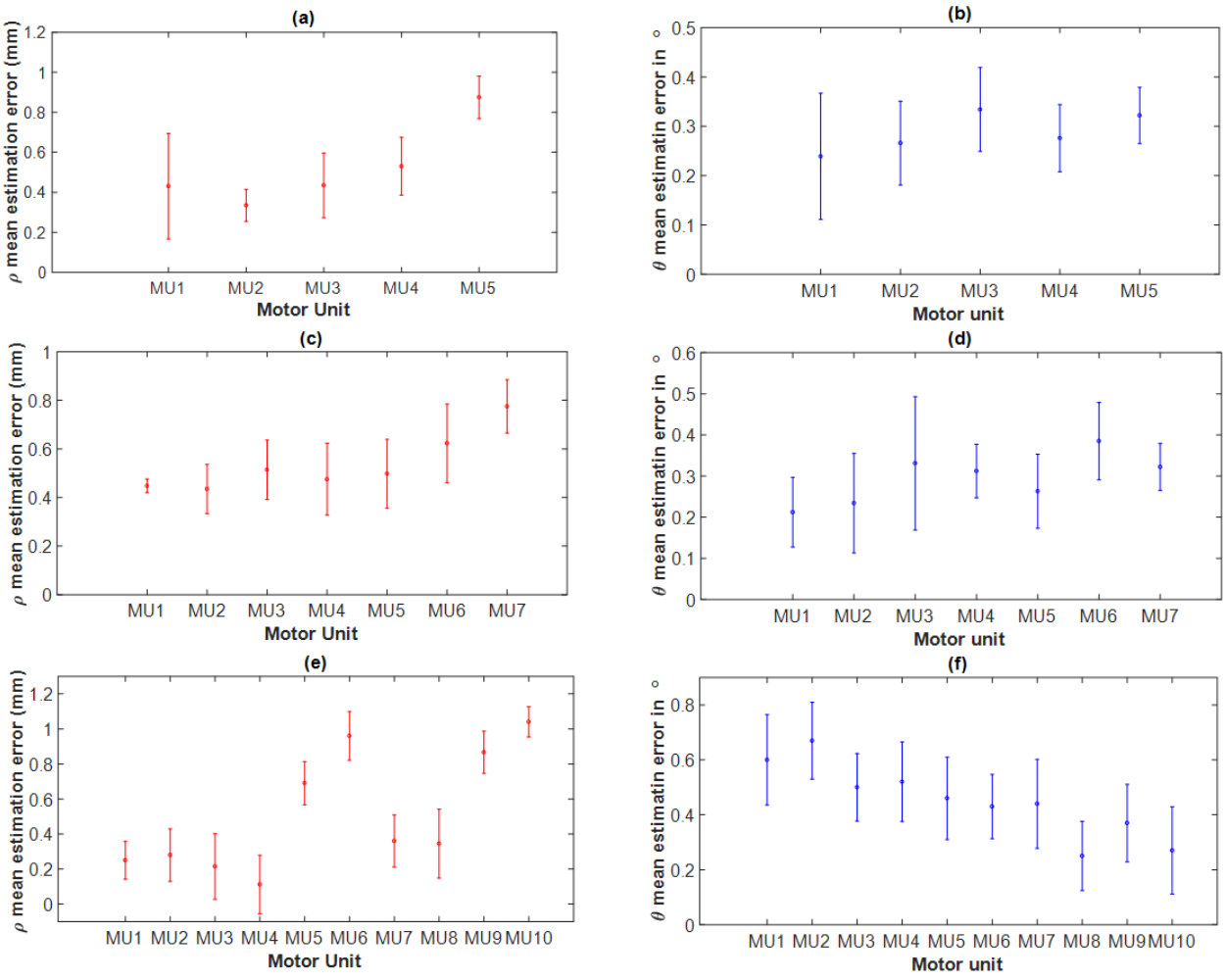

Figure 3.23: A plot of the error bars for the estimation of: (a) ρ (in red) for case 1, (b) θ (in blue) for case 1, (c) ρ (in red) for case 2, (d) θ (in blue) for case 2, (e) ρ (in red) for case 3, and (f) θ (in blue) for case 3. The center of each bar reflects the mean value and its width to both sides reflects the SD.

This was the same for scenario 2, where all 7 MUs also had a RMSE less than 1mm for ρ (Figure 3.23(c)) and less than 0.5° for θ (Figure 3.23(d)). For scenario 3, MU10 (which is the most superficial) had a RMSE of around 1mm for ρ, while the rest of the 9 MUs had a RMSE less than 1mm for ρ (Figure 3.23(e)). All 10 MUs had a RMSE less than 0.8° for θ (Figure 3.23(f)).

After that, the average of the mean and the SD of the localization errors and the temporal discharge errors for all the MUs collectively, in each of the 3 scenarios, is calculated and shown in Table 3.10. For scenario 1, for the 94 discharge times where the 5 MUs were spatially localized, the averaged RMSE for all the firing times (for those MUs that were located) was

17.8ms with a +/- SD of 13.9ms. The 5 MUs were localized with an averaged RMSE of less than 1mm for ρ and less than 0.5° for θ. For scenario 2, the averaged RMSE for the firing times of the 7 MUs collectively was 11.2ms with a +/- SD of 8.43ms. The averaged RMSE for the discharge times of the 10 MUs was 10.8ms with a +/- SD of 13.9ms for scenario 3. Similar results are obtained for ρ and θ averaged RMSE for the three scenarios.

Table 3.10: Summary of results of the mean and SD of the error (discharge time, ρ, and θ) for all the MUs together in each scenario.

Averaged RMSE								
Scenario 1			**Scenario 2**			**Scenario 3**		
Time (ms)	**ρ (mm)**	**θ (°)**	**Time (ms)**	**ρ (mm)**	**θ (°)**	**Time (ms)**	**ρ (mm)**	**θ (°)**
17.8 +/- 13.9	0.521 +/- 0.151	0.287 +/- 0.084	11.2 +/- 8.43	0.538 +/- 0.116	0.294 +/- 0.096	10.8 +/- 13.9	0.511 +/- 0.142	0.451 +/- 0.143

Also, the average of the estimated positions for each MU at different temporal discharges are plotted and compared with the actual locations and displayed in Figure 3.24(a) for scenario 1, in Figure 3.24(b) for scenario 2, and in Figure 3.24(c) for scenario 3 respectively.

One can observe little variations in the MU localization for the same MU at various firing time. This is mainly due to possible MUAP superposition happening in the same window when this MU is firing. For this reason, the maximum amplitude that the inverse solution of definite MU would give can increase or decrease in a small amount depending on the other MU firings involved in the same window. This leads to possible adaptive thresholding to take into account possible superposition.

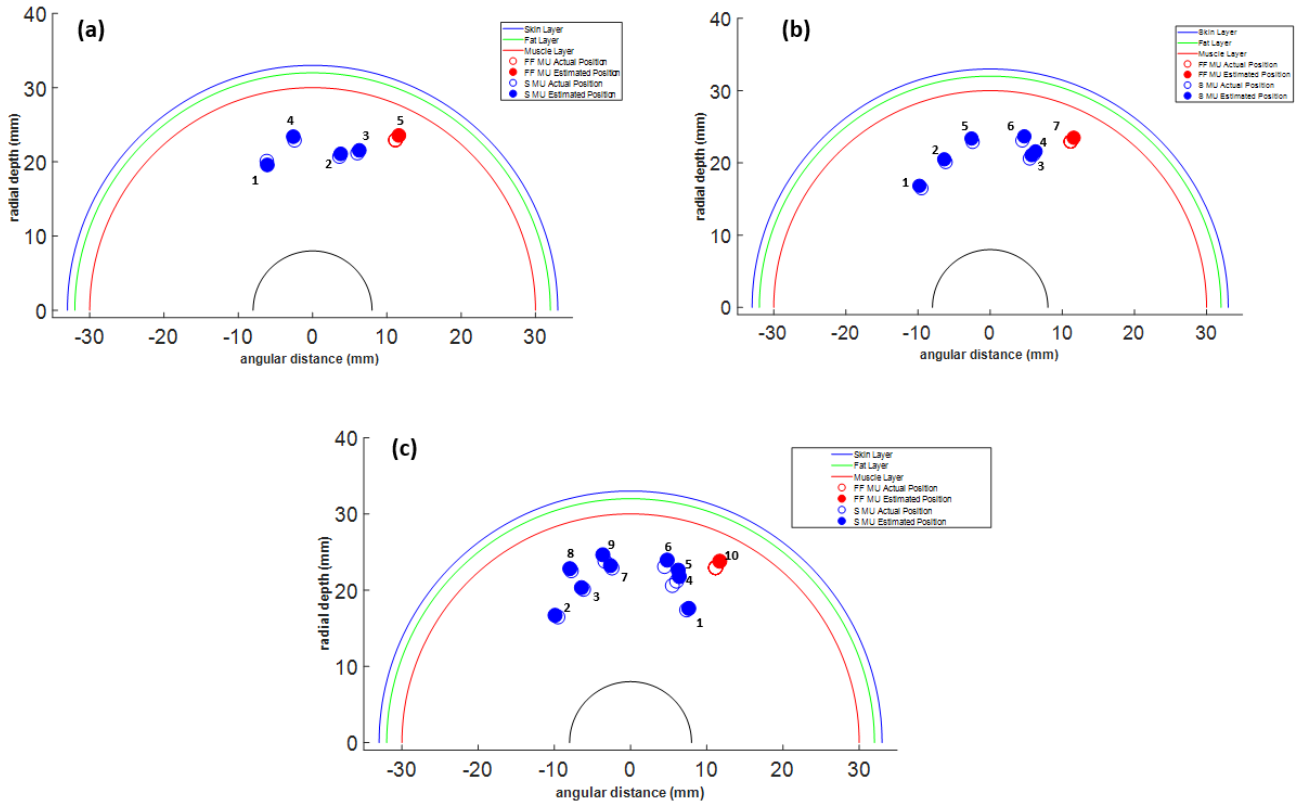

Figure 3.24: The average estimated position for each MU plotted against the actual position for: (a) scenario 1, (b) scenario 2, and (c) scenario 3.

Finally, the percentage of identification success of the algorithm, computed for each MU and each scenario, is displayed as a bar graph in Figure 3.25(a) for scenario 1, Figure 3.25(b) for scenario 2, and Figure 3.25(c) for scenario 3. For scenario 1, the percentages of success to recover both the spatial and temporal information of the MUs were as follows (Figure 3.25(a)): 35% for MU1 (the deepest), 48% for MU2, 50% for MU3, 77% for MU4 and 100% for MU5 (the most superficial) respectively. Concerning scenario 2, the percentages of success were (Figure 3.25(b)): 17% for MU1 (the deepest), 34% for MU2, 41% for MU3, 48% for MU4, 52% for MU5, 80% for MU6, and 100% for MU7 (the most superficial) respectively. Finally for scenario 3, the percentages of success were (Figure 3.25(c)): 8.33% for MU1 (the deepest), 10% for MU2, 9.1% for MU3, 18.4% for MU4, 21.8% for MU5, for MU6, 46% for MU7, 76% for MU8, 76.2% for MU9, and 100% for MU10 (the most superficial).

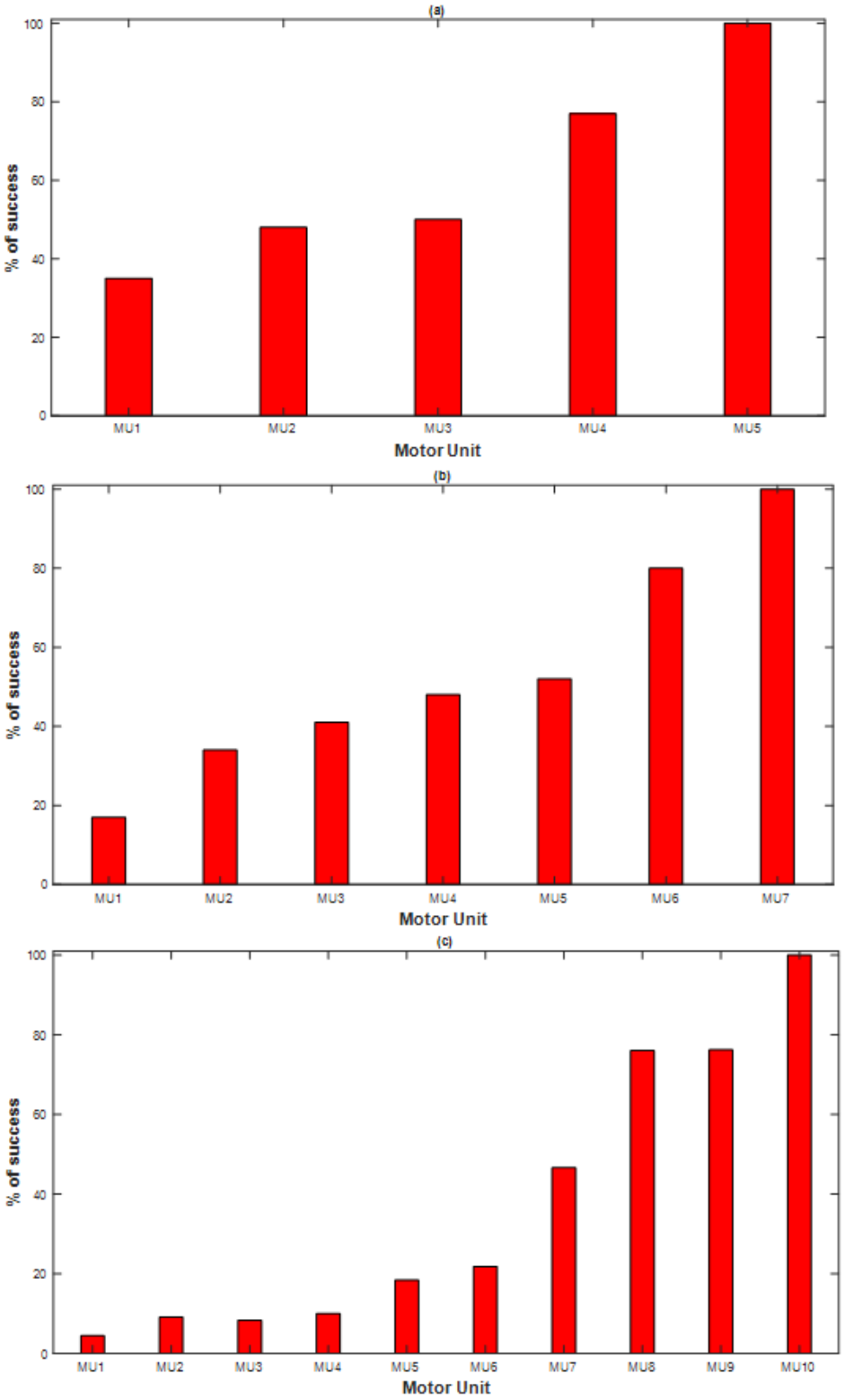

Figure 3.25: A bar graph of the % of identification success of the algorithm for both the spatial location and temporal firing for each MU in: (a) scenario 1, (b) scenario 2, and (c) scenario 3.

3.3.2 Discussion

The significance of this last part of the thesis is that it dealt with realistic MU recruitment patterns even though the number of MUs that were simulated was simplified. A novel approach of detecting both the spatial and temporal recruitment of MUs within a cylindrical muscle volume conductor was tested. Starting with the first scenario, 5 MUs of varying depth levels were put under test. As it was shown in Figure 3.25(a), MU1 had the least success rate (lower than 50%) in detecting both the spatial location and the discharge time at the same time. Meanwhile, MU5 had the highest success rate where it scored a 100%. This means that the algorithm gave promising abilities in collecting information about the spatial localization of this MU and each time this MU discharged throughout the measurement time. MU2, MU3, and MU4 had increasing success rates (50% and above). The reason why deeper MUs were not always being successfully detected is since most of the times those are being blurred by the inverse solution of the MU which is placed over them. Because we are relying in our algorithm on the maximum amplitude of the inverse solution in a definite window, and since deeper MUs will give lower maximum amplitudes that the ones positioned above them, it happens that the maximum amplitude of the deeper MU will coincide with the maximum amplitude of a more superficial one, thus leading to the detection of the more superficial one and the blurring of any MU which is deeper. This was also encountered in the approach followed by Mesin [20], where he simulated 4 muscle regions (two superficial and two deep) and he concluded that most of the classification error that occurred were due to the blurring effect of the superficial MUs at the expense on the deep ones. According to the results, the more we increased the number of MUs participating, the more complex the recruitment pattern became, and greater is the probability that more than one MU will fire in the same window simultaneously blurring the effect of all the

ones deeper than it. Thus, the deeper MUs will have lower success rates. For instance, in scenario 2, where 7 MUs of varying depths were participating, MU1, MU2, and MU3 had success rates less than 50%, while MU4, MU5, MU6, and MU7 had success rates higher than 50%, with the most superficial MU again scoring 100% detection success in both spatial and time location for the entire discharge pattern of the MU (Figure 3.25(b)). Thus, more than half of the MUs present in this example scored above 50%. For scenario 3, the number of MU increased to 10 MUs with a realistic recruitment pattern shown in Figure 3.17(d) corresponding to low muscle contraction level (between 5 to 10% MVC, Maximum Voluntary Contraction). Similarly, the more superficial MUs were more successfully detected at the expense of the deeper ones (Figure 3.25(c)). The deepest 4 MUs success rates dropped to below 20%, MU5 and MU6 between 20 & 40%, and MU7 till MU10 almost 50% and above respectively. We can see that the more the complexity increases, the more the deeper MUs are less detected at the expense of the more superficial ones. However, an important point must be highlighted. One can note that in the 3 scenarios, always the deepest MU is detected at least 1 time, and each of the participating MUs no matter how much their numbers increased is detected once. When we say detected, we mean both spatially and temporally. Therefore, the advantage of this algorithm is that it has 100% success in spatially detecting MUs with errors less than 1mm for ρ and less than 1° for θ. When it comes to detecting both the spatial as well as the temporal recruitment of the MU at the same time, the limitation of the algorithm is exhibited for the deeper MUs. The algorithm showed high success rates for the spatial and temporal localization of MUs at the expense of the deeper ones. Indeed, the limitation of this algorithm lies in the kind of information that we used to identify each MU using a simple rule (the maximum amplitude from the inverse solution image). Whatsoever, if we go back to the example in Figure 3.16, we can see that though our algorithm

was only capable of detecting one of the 3 MUs present in this window, visually, one can see the presence of the 3. Therefore, the information is embedded but the way to extract this information still needs to be improved.

As a possible insight to overcome this limitation, Artificial intelligence (AI) and machine learning can be employed [19]. Signal processing or image processing techniques could also be mixed with our algorithm to greatly increase its sensitivity to differentiate between different MUs even if this is blurred related to superposition effect in the same analyzing window. As a proposition, this might be by training a neural network with various inverse solution images of the same set of MUs discharging at different times. After several trainings, the neural network must be able to identify each MU from the other according to the way its inverse solution image is varying and not only according to a single parameter (like the maximum amplitude used in this study). In fact, the color map images showed that the inverse solution of each MU had a specific shape (signature or fingerprint) different from the others. As an inspiration for a future work, most recently, in July 2022, the researcher Bin He (who is really famous in source localization for EEG sources [114]), announced a novel, AI-based dynamic brain imaging technology capable of mapping out the changing electrical activity within the brain in a rapid manner and in real time. His team is currently working [137] on innovating a deep learning methodology which can accurately and rapidly translate the surface EEG signals recorded from the surface of the scalp to the sources that gave rise to those signals, and this all be done without any human involvement. Obviously, a similar approach should be applied on HD-sEMG signals that will improve spatiotemporal identification in different contexts and in presence of the described perturbations. On the other hand, it is important to recall that the proposed approach is model dependent. For now, only fusiform muscle, with aligned fibers, as the Biceps Brachii is

considered. However, the same methodology could be coupled to HD-sEMG generation model related to other muscles including pennate angles and varying anatomical geometry.

3.4 Conclusion

In this chapter, the robustness and limits of the CFB-MNE algorithm were tested. The main purpose of the first section was to check whether the same dictionary can work with any user regardless of his/her status or there is a need for a user personalized dictionary. What is meant by the status here is the age of the user, the medical status, the weight, and lifestyle. Also, the status might be related to the technical clinical settings during the measurement process (the way the electrode grid is placed on the muscle surface, the noise imposed on the measured signals, or the number of electrodes used). Results of the first section showed that the personalization of the dictionary according to the characteristic of the user is mandatory for some parameters. Therefore, after certain data are collected from the user (age, weight, BMI, disease history, etc.), the appropriate libraries for each parameter are selected and the algorithm is run for the most accurate localization results. As for the second section of this chapter, the algorithm was pushed to the limits by identifying realistic recruitment patterns of MUs. The advantage of the algorithm was that it was capable of the spatio-temporal recruitment of MUs in real-time, but not in equal success rates for all MUs; superficial MUs had better identification, in agreement with literature, than the deeper ones. Future perspectives to overcome the limitation of the proposed algorithm and to advance it further includes the use of machine learning methods coupled to image processing techniques applied on the inverse solution curve images. However, this work opens the door to possible real clinical applications, in a near future, and in more specific manner, to the study of aging effects (both functional and physiological) on the neuromuscular system for Model Aided Diagnosis (MAD) purpose.

General Conclusion

As it was stated earlier, the objective of the work done in this thesis was to provide an algorithm capable of real-time spatiotemporal localization of MUs using inverse methods applied on HD-sEMG signals. To accomplish this, several preparative steps were first executed in chapter 2 after describing the state of the art and the thesis objectives in chapter 1. Initially, the first contribution was a preliminary study including a comparison between the ability of two inverse problem methods (the MNE and wMNE) to reconstruct the sEMG signal (MUAP) set related to a predefined MU arrangement. For this part, a simple planar muscle model was first used, and the goal was to tune the methods and gain initial feedback about the proposed inverse problem algorithm performance. Results showed that when the sEMG signal (MUAP) is related to a deep MU position, the wMNE reconstructed this signal in a more efficient way than the MNE. Meanwhile, when the participating MUs are superficial, the MNE worked better.

After that, the second contribution was the proposition of a predictive spatial detection method that employs a 1D fitting curve constructed from information extracted from the 3D inverse solution space using a dictionary of pre-defined MUs with known discharge times and locations. The inverse method used was the MNE only since the wMNE did not work well when there was a bigger number of both superficial and deep MUs participating. Results showed that from this information, the locations of MUs were detected correctly but limited only to the radial change. As for the transverse change, we were not able to discriminate between a MU placed on the right and one on the left. Consequently, we reached the limit of the planar model and needed to shift to another more realistic model to design a more efficient identification method based on 3D curve fitting. Accordingly, another contribution was an innovative approach, namely the CFB-MNE method that involves the use of the classical minimum norm inverse method and a 3D fitting

curve interpolation, was proposed and tested. This algorithm was applied to HD-sEMG signals yielded from a sophisticated cylindrical muscle model. Indeed, several versions of this algorithm were presented and evaluated in terms of accuracy. Moreover, different parameters were extracted from the inverse solutions and their accuracy was evaluated as identifiers of the MU position. Among the parameters tested, the maximum amplitude, obtained from the analyzed window, of the inverse solution was shown to be the most appropriate. This predictive tool demonstrated to accurately work in real-time and in presence of noise. After these calibration steps of the algorithm, another famous inverse method was tested (sLORETA) to check whether there is a need to choose a method more accurate and faster than the classical MNE method. Results showed that the two methods had equivalent performances and that is why we chose to stick with the classical MNE method.

Following that, in chapter 3, the next contribution was to assess whether a unified dictionary works for any patient or there is a need to personalize the dictionaries according to each patient. Firstly, to do that, we assumed that there was a difference between one of the parameters when constructing the dictionary and between the same parameter in the actual patient (this parameter was either anatomical or due to the clinical measurement settings). Results showed that certain parameters such as the amount of additive Gaussian noise, do not affect the performance of the algorithm. However, other parameters, like the CV mean value, the fiber length, the muscle radius, and the fat thickness, etc. were influencing on the performance of the algorithm when there was a difference between the dictionary configuration and the tested simulated muscle. Hence, we were convinced that personalized libraries within dictionaries must be saved ahead of time and chosen for each patient at the time of the test. We also tackled the complex superposition problem, where several MUs can be fired in closer time inducing superposed

MUAPs that are difficult to identify. The obtained localization results concerning simple superposition cases showed promising results but with an important sensitivity to the vicinity of the superposed MUs and their depth.

The final contribution was the test of 3 scenarios of complex and realistic MU recruitment patterns. The method's ability to identify both the numerous discharge times of each MU as well as its spatial location was investigated. In fact, results showed that the algorithm is perfectly capable of spatially detecting MUs with errors less than 1mm for ρ and less than 1° for θ (100% success). As for the detection of both the spatial and the temporal recruitment of the MU at the same time, the limitations of the algorithm surfaced for the deeper MUs (less than 50% success). Indeed, the algorithm showed high success rates for the spatial and temporal localization of superficial MUs at the expense of the deeper ones. The reason for this is because of the data we are using to identify each MU (the maximum amplitude from the inverse solution image). Therefore, if more than one MU fired in the same window, inducing superposition, the maximum amplitude of one MU will mask the maximum amplitude of another MU (this is highly probable to occur in realistic MU firings).

Finally, as a future perspective to overcome the limitations of the proposed algorithm, the use of artificial intelligence (AI) and machine learning was proposed. A combination of AI approaches with signal processing and image processing techniques was suggested to eliminate the blurring action that the superposition effect imposes when more than one MU fires in the same analyzing window. However, it is noteworthy to re-mention that the study presented in this thesis is a preliminary work to benchmark an algorithm and the main purpose of this work was to calibrate and test the algorithm, on realistic simulated data, before applying it to real data whenever made possible. In fact, validation with real data remains a complex task that needs the availability of a

second validation modality like functional imaging. Thus, after hopefully a validation step, the main application of the proposed work, in a near future, will be its use in real-time sEMG applications such fatigue monitoring and muscle contraction monitoring with aging.

Bibliography

[1] C.-P. Ko, "Neuromuscular System," in *International Encyclopedia of the Social & Behavioral Sciences*, N. J. Smelser and P. B. Baltes, Eds. Oxford: Pergamon, 2001, pp. 10595–10600. doi: 10.1016/B0-08-043076-7/03482-3.

[2] K. Mukund and S. Subramaniam, "Skeletal muscle: A review of molecular structure and function, in health and disease.," *Wiley Interdiscip Rev Syst Biol Med*, vol. 12, no. 1, p. e1462, Jan. 2020, doi: 10.1002/wsbm.1462.

[3] K. Muramatsu, "Diabetes Mellitus-Related Dysfunction of the Motor System," *International Journal of Molecular Sciences*, vol. 21, no. 20, 2020, doi: 10.3390/ijms21207485.

[4] E. N. Marieb and K. Hoehn, "Muscles and Muscle Tissue," in *Human Anatomy & Physiology*, 1st ed., vol. 1, Pearson, pp. 278–320.

[5] M. J. Castellanos-Montiel, I. Velasco, and I. Escobedo-Avila, "Modeling the neuromuscular junction in vitro: an approach to study neuromuscular junction disorders," *Annals of the New York Academy of Sciences*, vol. 1488, no. 1, pp. 3–15, 2021, doi: https://doi.org/10.1111/nyas.14504.

[6] R. M. Enoka and J. Duchateau, "Rate Coding and the Control of Muscle Force," *Cold Spring Harb Perspect Med*, vol. 7, no. 10, p. a029702, Oct. 2017, doi: 10.1101/cshperspect.a029702.

[7] E. G. T. LIDDELL and C. G. PHILLIPS, "The cortical representation of motor units.," *Brain*, vol. 75, no. 4, pp. 510–525, Dec. 1952, doi: 10.1093/brain/75.4.510.

[8] G. Kamen and D. A. Gabriel, *Essentials of Electromyography*. Human Kinetics, 2010. [Online]. Available: https://books.google.com.lb/books?id=0a9LnwEACAAJ

[9] D. F. Stegeman, B. U. Kleine, B. G. Lapatki, and J. P. van Dijk, "High-density Surface EMG: Techniques and Applications at a Motor Unit Level," *Biocybernetics and Biomedical Engineering*, vol. 32, no. 3, pp. 3–27, 2012, doi: https://doi.org/10.1016/S0208-5216(12)70039-6.

[10] D. G. Sale, "Influence of exercise and training on motor unit activation.," *Exerc Sport Sci Rev*, vol. 15, pp. 95–151, 1987.

[11] R. D. Henderson and P. A. McCombe, "Assessment of Motor Units in Neuromuscular Disease.," *Neurotherapeutics*, vol. 14, no. 1, pp. 69–77, Jan. 2017, doi: 10.1007/s13311-016-0473-z.

[12] K. Nizamis, N. H. M. Rijken, R. van Middelaar, J. Neto, B. F. J. M. Koopman, and M. Sartori, "Characterization of Forearm Muscle Activation in Duchenne Muscular Dystrophy via High-Density Electromyography: A Case Study on the Implications for Myoelectric Control," *Frontiers in Neurology*, vol. 11, 2020, doi: 10.3389/fneur.2020.00231.

[13] J. M. Hidler and A. E. Wall, "Alterations in muscle activation patterns during robotic-assisted walking.," *Clin Biomech (Bristol, Avon)*, vol. 20, no. 2, pp. 184–193, Feb. 2005, doi: 10.1016/j.clinbiomech.2004.09.016.

[14] S. Srivastava, C. Patten, and S. Kautz, “Altered muscle activation patterns (AMAP): An analytical tool to compare muscle activity patterns of hemiparetic gait with a normative profile,” *Journal of NeuroEngineering and Rehabilitation*, vol. 16, Jan. 2019, doi: 10.1186/s12984-019-0487-y.

[15] T. Castroflorio, D. Falla, K. Wang, P. Svensson, and D. Farina, “Effect of experimental jaw-muscle pain on the spatial distribution of surface EMG activity of the human masseter muscle during tooth clenching.,” *J Oral Rehabil*, vol. 39, no. 2, pp. 81–92, Feb. 2012, doi: 10.1111/j.1365-2842.2011.02246.x.

[16] Y. Wen, S. Avrillon, J. C. Hernandez-Pavon, S. J. Kim, F. Hug, and J. L. Pons, “A convolutional neural network to identify motor units from high-density surface electromyography signals in real time.,” *J Neural Eng*, vol. 18, no. 5, Apr. 2021, doi: 10.1088/1741-2552/abeead.

[17] L. Mesin, “Real time identification of active regions in muscles from high density surface electromyogram,” *Computers in biology and medicine*, vol. 56, pp. 37–50, 2014, doi: 10.1016/j.compbiomed.2014.10.017.

[18] L. Mesin, “Optimal spatio-temporal filter for the reduction of crosstalk in surface electromyogram.,” *J Neural Eng*, vol. 15, no. 1, p. 016013, Feb. 2018, doi: 10.1088/1741-2552/aa8f03.

[19] T. Yu, K. Akhmadeev, E. Le Carpentier, Y. Aoustin, and D. Farina, “Highly Accurate Real-Time Decomposition of Single Channel Intramuscular EMG,” *IEEE Transactions on Biomedical Engineering*, vol. PP, pp. 1–1, Aug. 2021, doi: 10.1109/TBME.2021.3104621.

[20] L. Mesin, “Real time identification of active regions in muscles from high density surface electromyogram,” *Computers in biology and medicine*, vol. 56, pp. 37–50, 2014, doi: 10.1016/j.compbiomed.2014.10.017.

[21] K. van den Doel, U. Ascher, and D. K Pai, “Computed myography: Three-dimensional reconstruction of motor functions from surface EMG data,” *Inverse Problems*, vol. 24, no. 6, p. 065010, 2008, doi: 10.1088/0266-5611/24/6/065010.

[22] K. van den Doel, U. Ascher, and D. K Pai, “Source localization in electromyography using the inverse potential problem,” *Inverse Problems*, vol. 27, no. 2, p. 025008, 2011, doi: 10.1088/0266-5611/27/2/025008.

[23] V. Carriou, S. Boudaoud, J. Laforet, and F. S. Ayachi, “Fast generation model of high density surface EMG signals in a cylindrical conductor volume,” *Computers in Biology and Medicine*, vol. 74, pp. 54–68, 2016, doi: https://doi.org/10.1016/j.compbiomed.2016.04.019.

[24] D. Farina, R. Merletti, and R. M. Enoka, “The extraction of neural strategies from the surface EMG: an update,” *Journal of applied physiology (Bethesda, Md. : 1985)*, vol. 117, no. 11, p. 1215—1230, Dec. 2014, doi: 10.1152/japplphysiol.00162.2014.

[25] Y. Zhang, “Noninvasive imaging of internal muscle activities from multi-channel surface EMG recordings,” *35th Annual International Conference of the IEEE Engineering in Medicine and Biology Society (EMBC)*, pp. 5430–5432, 2013, doi: 10.1109/EMBC.2013.6610777.

[26] I. Y. Shadrin, A. Khodabukus, and N. Bursac, “Striated muscle function, regeneration, and repair,” *Cell Mol Life Sci*, vol. 73, no. 22, pp. 4175–4202, Nov. 2016, doi: 10.1007/s00018-016-2285-z.

[27] K. Mukund and S. Subramaniam, “Skeletal muscle: A review of molecular structure and function, in health and disease,” *Wiley Interdiscip Rev Syst Biol Med*, vol. 12, no. 1, pp. e1462–e1462, Jan. 2020, doi: 10.1002/wsbm.1462.

[28] P. D. Wilson, “Anatomy of Muscle,” in *Reference Module in Biomedical Sciences*, Elsevier, 2014. doi: https://doi.org/10.1016/B978-0-12-801238-3.00250-6.

[29] P. J. Mansfield and D. A. Neumann, “Chapter 3 - Structure and Function of Skeletal Muscle,” in *Essentials of Kinesiology for the Physical Therapist Assistant (Third Edition)*, Third Edition., P. J. Mansfield and D. A. Neumann, Eds. St. Louis (MO): Mosby, 2019, pp. 34–49. doi: https://doi.org/10.1016/B978-0-323-54498-6.00003-5.

[30] Z. Radák, “Chapter 2 - Skeletal Muscle, Function, and Muscle Fiber Types,” in *The Physiology of Physical Training*, Z. Radák, Ed. Academic Press, 2018, pp. 15–31. doi: 10.1016/B978-0-12-815137-2.00002-4.

[31] O. Halevy and S. G. Velleman, “Chapter 23 - Skeletal muscle,” in *Sturkie’s Avian Physiology (Seventh Edition)*, Seventh Edition., C. G. Scanes and S. Dridi, Eds. San Diego: Academic Press, 2022, pp. 565–589. doi: https://doi.org/10.1016/B978-0-12-819770-7.00024-4.

[32] H. L. Sweeney and D. W. Hammers, “Muscle Contraction,” *Cold Spring Harb Perspect Biol*, vol. 10, no. 2, p. a023200, Feb. 2018, doi: 10.1101/cshperspect.a023200.

[33] W. Scott, J. Stevens, and S. A. Binder–Macleod, “Human Skeletal Muscle Fiber Type Classifications,” *Physical Therapy*, vol. 81, no. 11, pp. 1810–1816, Nov. 2001, doi: 10.1093/ptj/81.11.1810.

[34] R. C. Foehring, G. W. Sypert, and J. B. Munson, “Properties of self-reinnervated motor units of medial gastrocnemius of cat. I. Long-term reinnervation.,” *J Neurophysiol*, vol. 55, no. 5, pp. 931–946, May 1986, doi: 10.1152/jn.1986.55.5.931.

[35] C. J. Heckman and R. Enoka, “Physiology of the motor neuron and the motor unit,” *Handbook of Clinical Neurophysiology*, vol. 4, pp. 119–147, Dec. 2004, doi: 10.1016/S1567-4231(04)04006-7.

[36] B. R. MacIntosh , Gardiner, Phillip F.,, McComas, Alan J., “Skeletal muscle : form and function,” 2006. http://catalog.hathitrust.org/api/volumes/oclc/57625723.html

[37] J. Duchateau and R. M. Enoka, “Distribution of motor unit properties across human muscles.,” *J Appl Physiol (1985)*, vol. 132, no. 1, pp. 1–13, Jan. 2022, doi: 10.1152/japplphysiol.00290.2021.

[38] R. Merletti and D. Farina, *Surface Electromyography: Physiology, Engineering and Applications*. 2016. doi: 10.1002/9781119082934.

[39] E. Henneman, “Relation between Size of Neurons and Their Susceptibility to Discharge,” *Science*, vol. 126, no. 3287, pp. 1345–1347, 1957.

[40] D. Farina, M. Fosci, and R. Merletti, “Motor unit recruitment strategies investigated by surface EMG variables.,” *J Appl Physiol (1985)*, vol. 92, no. 1, pp. 235–247, Jan. 2002, doi: 10.1152/jappl.2002.92.1.235.

[41] A. J. Fuglevand, D. A. Winter, and A. E. Patla, “Models of recruitment and rate coding organization in motor-unit pools.,” *J Neurophysiol*, vol. 70, no. 6, pp. 2470–2488, Dec. 1993, doi: 10.1152/jn.1993.70.6.2470.

[42] J. Duchateau and S. Baudry, “Maximal discharge rate of motor units determines the maximal rate of force development during ballistic contractions in human,” *Frontiers in Human Neuroscience*, vol. 8, 2014, doi: 10.3389/fnhum.2014.00234.

[43] C. Gregory and C. Bickel, “Recruitment Patterns in Human Skeletal Muscle During Electrical Stimulation,” *Physical therapy*, vol. 85, pp. 358–64, May 2005, doi: 10.1093/ptj/85.4.358.

[44] H. S. Milner-Brown, R. B. Stein, and R. Yemm, “Changes in firing rate of human motor units during linearly changing voluntary contractions.,” *J Physiol*, vol. 230, no. 2, pp. 371–390, Apr. 1973, doi: 10.1113/jphysiol.1973.sp010193.

[45] B. Schlink, A. Nordin, C. Brooks, and D. Ferris, “Fatigue induces altered spatial myoelectric activation patterns in the medial gastrocnemius during locomotion,” *Journal of neurophysiology*, vol. 125, Apr. 2021, doi: 10.1152/jn.00602.2020.

[46] Z. Gao *et al.*, “Spatial Reorganization of Myoelectric Activities in Extensor Digitorum for Sustained Finger Force Production,” *Sensors*, vol. 19, p. 555, Jan. 2019, doi: 10.3390/s19030555.

[47] Y. K. Mariappan, A. Manduca, K. J. Glaser, J. Chen, K. K. Amrami, and R. L. Ehman, “Vibration imaging for localization of functional compartments of the extrinsic flexor muscles of the hand.,” *J Magn Reson Imaging*, vol. 31, no. 6, pp. 1395–1401, Jun. 2010, doi: 10.1002/jmri.22183.

[48] S. Brorsson, A. Nilsdotter, M. Hilliges, C. Sollerman, and Y. Aurell, “Ultrasound evaluation in combination with finger extension force measurements of the forearm musculus extensor digitorum communis in healthy subjects.,” *BMC Med Imaging*, vol. 8, p. 6, Mar. 2008, doi: 10.1186/1471-2342-8-6.

[49] H. Nakamura, M. Yoshida, M. Kotani, K. Akazawa, and T. Moritani, “The application of independent component analysis to the multi-channel surface electromyographic signals for separation of motor unit action potential trains: part I-measuring techniques,” *J Electromyogr Kinesiol*, vol. 14, no. 4, pp. 423–432, Aug. 2004, doi: 10.1016/j.jelekin.2004.01.004.

[50] J. R. Florestal, P. A. Mathieu, and A. Malanda, “Automated decomposition of intramuscular electromyographic signals,” *IEEE Transactions on Biomedical Engineering*, vol. 53, no. 5, pp. 832–839, May 2006, doi: 10.1109/TBME.2005.863893.

[51] M. Gazzoni, D. Farina, and R. Merletti, “A new method for the extraction and classification of single motor unit action potentials from surface EMG signals,” *J. Neurosci. Methods*, vol. 136, no. 2, pp. 165–177, Jul. 2004, doi: 10.1016/j.jneumeth.2004.01.002.

[52] M. Chen, X. Zhang, and P. Zhou, “A Novel Validation Approach for High Density Surface EMG Decomposition in Motor Neuron Disease,” *IEEE Transactions on Neural Systems and Rehabilitation Engineering*, vol. PP, pp. 1–1, May 2018, doi: 10.1109/TNSRE.2018.2836859.

[53] M. Chen and P. Zhou, “A Novel Framework Based on FastICA for High Density Surface EMG Decomposition,” *IEEE Trans Neural Syst Rehabil Eng*, vol. 24, no. 1, pp. 117–127, Jan. 2016, doi: 10.1109/TNSRE.2015.2412038.

[54] O. Iqbal, S. A. Fattah, and S. Zahin, “Hand movement recognition based on singular value decomposition of surface EMG signal,” in *2017 IEEE Region 10 Humanitarian Technology Conference (R10-HTC)*, Dec. 2017, pp. 837–842. doi: 10.1109/R10-HTC.2017.8289085.

[55] S. Nawab, S.-S. Chang, and C. De Luca, “High-Yield Decomposition of Surface EMG Signals,” *Clinical neurophysiology : official journal of the International Federation of Clinical Neurophysiology*, vol. 121, pp. 1602–15, Oct. 2010, doi: 10.1016/j.clinph.2009.11.092.

[56] J. Roussel, P. Ravier, M. Haritopoulos, D. Farina, and O. Buttelli, “Decomposition of Multi-Channel Intramuscular EMG Signals by Cyclostationary-Based Blind Source Separation,” *IEEE Transactions on Neural Systems and Rehabilitation Engineering*, vol. 25, no. 11, pp. 2035–2045, Nov. 2017, doi: 10.1109/TNSRE.2017.2700890.

[57] F. Negro, S. Muceli, A. M. Castronovo, A. Holobar, and D. Farina, “Multi-channel intramuscular and surface EMG decomposition by convolutive blind source separation,” *J Neural Eng*, vol. 13, no. 2, p. 026027, Apr. 2016, doi: 10.1088/1741-2560/13/2/026027.

[58] X. Zhu and Y. Zhang, “High-density surface EMG decomposition based on a convolutive blind source separation approach,” *Conference proceedings : ... Annual International Conference of the IEEE Engineering in Medicine and Biology Society. IEEE Engineering in Medicine and Biology Society. Conference*, vol. 2012, pp. 609–12, Aug. 2012, doi: 10.1109/EMBC.2012.6346005.

[59] R. Merletti, A. Holobar, and D. Farina, “Analysis of motor units with high-density surface electromyography,” *Journal of Electromyography and Kinesiology*, vol. 18, no. 6, pp. 879–890, 2008, doi: https://doi.org/10.1016/j.jelekin.2008.09.002.

[60] M. Harrach, “Modeling of the sEMG/Force relationship by data analysis of high resolution sensor network,” 2016. doi: 10.13140/RG.2.2.31448.49922.

[61] G. Drost, D. F. Stegeman, B. G. M. van Engelen, and M. J. Zwarts, “Clinical applications of high-density surface EMG: a systematic review.,” *J Electromyogr Kinesiol*, vol. 16, no. 6, pp. 586–602, Dec. 2006, doi: 10.1016/j.jelekin.2006.09.005.

[62] C. J. De Luca, A. Adam, R. Wotiz, L. D. Gilmore, and S. H. Nawab, “Decomposition of surface EMG signals,” *J. Neurophysiol.*, vol. 96, no. 3, pp. 1646–1657, Sep. 2006, doi: 10.1152/jn.00009.2006.

[63] S. Baillet, J. C. Mosher, and R. M. Leahy, “Electromagnetic brain mapping,” *IEEE Signal Processing Magazine*, vol. 18, no. 6, pp. 14–30, 2001, doi: 10.1109/79.962275.

[64] Y. Zhang, D. Wang, and G. W. Timm, "A three-dimensional muscle activity imaging technique for assessing pelvic muscle function," *Inverse Problems*, vol. 26, no. 11, p. 115018, 2010.

[65] R. Howard, R. Conway, and A. Harrison, *An Exploration of Eliminating Cross-Talk in Surface Electromyography using Independent Component Analysis*. 2015. doi: 10.1109/ISSC.2015.7163754.

[66] J. M. Kilner, S. N. Baker, and R. N. Lemon, "A novel algorithm to remove electrical cross-talk between surface EMG recordings and its application to the measurement of short-term synchronisation in humans.," *J Physiol*, vol. 538, no. Pt 3, pp. 919–930, Feb. 2002, doi: 10.1113/jphysiol.2001.012950.

[67] N. Dimitrova and G. V. Dimitrov, "Electromyography (EMG) Modeling," 2006. doi: 10.1002/9780471740360.ebs0656.

[68] J. Malmivuo and R. Plonsey, *Bioelectromagnetism. 7. Volume Source and Volume Conductor*. 1995.

[69] B. He, A. Sohrabpour, E. Brown, and Z. Liu, "Electrophysiological Source Imaging: A Noninvasive Window to Brain Dynamics," *Annu. Rev. Biomed. Eng.*, vol. 20, no. 1, pp. 171–196, Jun. 2018, doi: 10.1146/annurev-bioeng-062117-120853.

[70] H. Hallez *et al.*, "Review on solving the forward problem in EEG source analysis," *Journal of neuroengineering and rehabilitation*, vol. 4, p. 46, 2007, doi: 10.1186/1743-0003-4-46.

[71] H. Hallez *et al.*, "Review on solving the forward problem in EEG source analysis," *Journal of neuroengineering and rehabilitation*, vol. 4, p. 46, 2007, doi: 10.1186/1743-0003-4-46.

[72] A. Heringa, D. F. Stegeman, G. J. Uijen, and J. P. de Weerd, "Solution methods of electrical field problems in physiology.," *IEEE Trans Biomed Eng*, vol. 29, no. 1, pp. 34–42, Jan. 1982, doi: 10.1109/TBME.1982.324961.

[73] T. Gootzen, D. Stegeman, and A. Heringa, "On numerical problems in analytical calculations of extracellular fields in bounded cylindrical volume conductors," *Journal of Applied Physics*, vol. 66, pp. 4504–4508, 1989, doi: 10.1063/1.343949.

[74] T. Gootzen, D. Stegeman, and A. Van Oosterom, "Finite limb dimensions and finite muscle length in a model for the generation of electromyographic signals," *Electroencephalography and clinical neurophysiology*, vol. 81, pp. 152–62, 1991, doi: 10.1016/0168-5597(91)90008-L.

[75] K. Roeleveld, J. H. Blok, D. Stegeman, and A. van Oosterom, "Volume conduction models for surface EMG; Confrontation with measurements," *Journal of electromyography and kinesiology : official journal of the International Society of Electrophysiological Kinesiology*, vol. 7, pp. 221–232, 1998, doi: 10.1016/S1050-6411(97)00009-6.

[76] D. Farina and A. Rainoldi, "Compensation of the effect of sub-cutaneous tissue layers on surface EMG: A simulation study," *Medical engineering & physics*, vol. 21, pp. 487–97, 1999, doi: 10.1016/S1350-4533(99)00075-2.

[77] J. H Blok, D. Stegeman, and A. van Oosterom, “Three-Layer Volume Conductor Model and Software Package for Applications in Surface Electromyography,” *Annals of biomedical engineering*, vol. 30, pp. 566–77, 2002, doi: 10.1114/1.1475345.

[78] M. Lowery, N. Stoykov, A. Taflove, and T. Kuiken, “A multi-layer finite element model of the surface EMG signal,” 2001, vol. 2, pp. 1051–1054 vol.2. doi: 10.1109/IEMBS.2001.1020369.

[79] M. Lowery, N. S Stoykov, J. P. A. Dewald, and T. A. Kuiken, “Volume Conduction in an Anatomically Based Surface EMG Model,” *Biomedical Engineering, IEEE Transactions on*, vol. 51, pp. 2138–2147, 2005, doi: 10.1109/TBME.2004.836494.

[80] L. Mesin and D. Farina, “A Model for Surface EMG Generation in Volume Conductors With Spherical Inhomogeneities,” *IEEE transactions on bio-medical engineering*, vol. 52, pp. 1984–93, 2006, doi: 10.1109/TBME.2005.857670.

[81] G. V. Dimitrov and N. Dimitrova, “Precise and fast calculation of the motor unit potentials detected by a point and rectangular plate electrode,” *Medical engineering & physics*, vol. 20, pp. 374–81, 1998, doi: 10.1016/S1350-4533(98)00014-9.

[82] D. Farina and R. Merletti, “A novel approach for precise simulation of the EMG signal detected by surface electrodes,” *Biomedical Engineering, IEEE Transactions on*, vol. 48, pp. 637–646, 2001, doi: 10.1109/10.923782.

[83] J. Duchêne and J.-Y. Hogrel, *A model of EMG generation*, vol. 47. 2000. doi: 10.1109/10.821754.

[84] R. Merletti, L. Lo Conte, E. Avignone, and P. Guglielminotti, “Modeling of surface myoelectric signals - Part I: Model implementation,” *IEEE transactions on bio-medical engineering*, vol. 46, pp. 810–20, 1999, doi: 10.1109/10.771190.

[85] D. Farina, L. Mesin, S. Martina, and R. Merletti, “A Surface EMG Generation Model With Multilayer Cylindrical Description of the Volume Conductor,” *IEEE transactions on bio-medical engineering*, vol. 51, pp. 415–26, 2004, doi: 10.1109/TBME.2003.820998.

[86] T. A. Kuiken, N. S. Stoykov, M. Popović, M. Lowery, and A. Taflove, “Finite element modeling of electromagnetic signal propagation in a phantom arm,” *IEEE transactions on neural systems and rehabilitation engineering : a publication of the IEEE Engineering in Medicine and Biology Society*, vol. 9, pp. 346–54, 2001, doi: 10.1109/7333.1000114.

[87] D. Hyde, M. Dannhauer, S. Warfield, R. MacLeod, and D. Brooks, “Evaluation of Numerical Techniques for Solving the Current Injection Problem in Biological Tissues,” in *Proceedings. IEEE International Symposium on Biomedical Imaging*, 2016, vol. 2016, pp. 876–880. doi: 10.1109/ISBI.2016.7493405.

[88] E. Olivi, “Coupling of numerical methods for the forward problem in Magneto- and Electro-Encephalography,” 2011.

[89] R. Grech *et al.*, “Review on solving the inverse problem in EEG source analysis,” *Journal of NeuroEngineering and Rehabilitation*, vol. 5, no. 1, p. 25, Nov. 2008, doi: 10.1186/1743-0003-5-25.

[90] S. Baillet, J. Mosher, and R. M. Leahy, “Electromagnetic Brain Mapping,” *IEEE Signal Processing Magazine*, vol. 18, no. 6, pp. 14–30, Dec. 2001, doi: 10.1109/79.962275.

[91] C. M. Michel, M. M. Murray, G. Lantz, S. Gonzalez, L. Spinelli, and R. Grave de Peralta, “EEG source imaging,” *Clinical Neurophysiology*, vol. 115, no. 10, pp. 2195–2222, Oct. 2004, doi: 10.1016/j.clinph.2004.06.001.

[92] M. Jatoi, N. Kamel, A. Malik, I. Faye, and T. Begum, “A survey of methods used for source localization using EEG signals,” *Biomedical Signal Processing and Control*, vol. 11, pp. 42–52, 2014, doi: 10.1016/j.bspc.2014.01.009.

[93] H. Urbanek and P. Van der Smagt, “iEMG: Imaging Electromyography,” *Journal of Electromyography and Kinesiology*, vol. 27, no. 27, 2016, doi: 10.1016/j.jelekin.2016.01.001.

[94] R. Hyder, N. Kamel, T. B. Tang, and J. Bornot, “Brain source localization techniques: Evaluation study using simulated EEG data,” in *2014 IEEE Conference on Biomedical Engineering and Sciences (IECBES)*, 2014, pp. 942–947. doi: 10.1109/IECBES.2014.7047651.

[95] K. van den Doel, U. Ascher, D. K Pai, and J. Steeves, “Computed myography: Three-dimensional reconstruction of motor functions from surface EMG data,” *Inverse Problems*, vol. 24, p. 065010, 2008, doi: 10.1088/0266-5611/24/6/065010.

[96] K. Sekihara and S. S. Nagarajan, “Minimum-Norm-Based Source Imaging Algorithms,” in *Electromagnetic Brain Imaging: A Bayesian Perspective*, K. Sekihara and S. S. Nagarajan, Eds. Cham: Springer International Publishing, 2015, pp. 9–28. doi: 10.1007/978-3-319-14947-9_2.

[97] R. M. Leahy, Mosher J.C., and Phillips J.W., “A Comparative Study of Minimum Norm Inverse Methods for MEG Imaging.,” 2000.

[98] C. Lawson and R. Henson, “22. Linear Least Squares with Linear Equality Constraints by Weighting,” in *Solving Least Squares Problems*, 2015, pp. 148–157. doi: 10.1137/1.9781611971217.ch22.

[99] A. Diab, J. Laforet, B. Karlsson, and C. Marque, “EHG Source Localization Using Signals from a Uterus Electrophysiological Model,” Sep. 2014. doi: 10.13140/2.1.2367.5202.

[100] S. Zahran *et al.*, “Performance of source imaging techniques of spatially extended generators of uterine activity,” *Informatics in Medicine Unlocked*, vol. 16, p. 100167, Sep. 2019, doi: 10.1016/j.imu.2019.100167.

[101] M. Hassan, O. Dufor, I. Merlet, C. Berrou, and F. Wendling, “EEG source connectivity analysis: from dense array recordings to brain networks,” *PLoS One*, vol. 9, no. 8, pp. e105041–e105041, Aug. 2014, doi: 10.1371/journal.pone.0105041.

[102] A. Gydikov, D. Kosarov, and N. Tankov, “Studying the alpha motoneurone activity by investigating motor units of various sizes.,” *Electroencephalography and Clinical Neurophysiology*, vol. 12, no. 2, pp. 99–117, 1972.

[103] D. Kosarov, A. Gydikov, and N. Tankov, "Improvement of the method of motor units location.," *Electromyogr Clin Neurophysiol*, vol. 14, no. 1, pp. 97–107, 1974.

[104] A.Willem Monster and H.Chan, "Surface electromyogram potentials of motor units; Relationship between potential size and unit location in a large human skeletal muscle," vol. 67, no. 2, 1980.

[105] R. A. Jesinger and V. L. Stonick, "Processing signals from surface electrode arrays for noninvasive 3D mapping of muscle activity," in *Proceedings of IEEE 6th Digital Signal Processing Workshop*, Nov. 1994, pp. 57–60. doi: 10.1109/DSP.1994.379868.

[106] E. Lopresti, R. A. Jesinger, and V. L. Stonick, *Identifying significant frequencies in surface EMG signals for localization of neuromuscular activity*. 1995. doi: 10.1109/IEMBS.1995.579384.

[107] J. T. Stonick, R. A. Jesinger, V. L. Stonick and S. B. Baumann, "Estimation and localization of multiple dipole sources for noninvasive mapping of muscle activity," *IEEE International Conference on Acoustics, Speech, and Signal Processing Conference Proceedings*, vol. 5, pp. 2912–2915.

[108] K. Roeleveld, A. Sandberg, E. V. Stålberg, and D. Stegeman, "Motor unit size estimation of enlarged motor units with surface electromyography.," *Muscle Nerve*, vol. 21, no. 7, pp. 878–886, Aug. 1998, doi: 10.1002/(sici)1097-4598(199807)21:7<878::aid-mus5>3.0.co;2-3.

[109] K. Saitou, T. Masuda, and M. Okada, "Depth and intensity of equivalent current dipoles estimated through an inverse analysis of surface electromyograms using the image method," *Med Biol Eng Comput*, vol. 37, no. 6, Dec. 1999, doi: 10.1007/BF02513373.

[110] E. Chauvet, O. Fokapu, and D. Gamet, "Inverse problem in the surface EMG: a feasibility study," in *2001 Conference Proceedings of the 23rd Annual International Conference of the IEEE Engineering in Medicine and Biology Society*, Feb. 2001, vol. 2, pp. 1048–1050. doi: 10.1109/IEMBS.2001.1020368.

[111] J. Wang, Y. Zhang, X. Zhu, P. Zhou, C. Liu, and W. Rymer, "A novel spatiotemporal muscle activity imaging approach based on the Extended Kalman Filter," in *Annual International Conference of the IEEE Engineering in Medicine and Biology Society*, 2012, pp. 6236–6238. doi: 10.1109/EMBC.2012.6347419.

[112] A. Liu, Y. Ning, J. He, S. Li, P. Zhou, and Y. Zhang, "Internal muscle activity imaging from multi-channel surface EMG recordings: A validation study," in *2014 36th Annual International Conference of the IEEE Engineering in Medicine and Biology Society, EMBC*, 2014, pp. 3559–61. doi: 10.1109/EMBC.2014.6944391.

[113] Holger Urbanek and Patrick van der Smagt, "iEMG: Imaging electromyography," *Journal of Electromyography and Kinesiology*, vol. 27, no. 27, pp. 1–9.

[114] B. He, A. Sohrabpour, E. Brown, and Z. Liu, "Electrophysiological Source Imaging: A Noninvasive Window to Brain Dynamics," *Annual Review of Biomedical Engineering*, pp. 171–196, 2018.

[115] G. V. Dimitrov and N. Dimitrova, “Precise and fast calculation of the motor unit potentials detected by a point and rectangular plate electrode,” *Medical engineering & physics*, vol. 20, pp. 374–81, 1998, doi: 10.1016/S1350-4533(98)00014-9.

[116] F. N. Wilson, A. G. Macleod, and P. S. Barker, “The Distribution of the Action Currents Produced by Heart Muscle and Other Excitable Tissues Immersed in Extensive Conducting Media.,” *J Gen Physiol*, vol. 16, no. 3, pp. 423–456, Jan. 1933, doi: 10.1085/jgp.16.3.423.

[117] R. Plonsey, “Volume Conductor Fields of Action Currents,” *Biophys J*, vol. 4, no. 4, pp. 317–328, Jul. 1964, doi: 10.1016/s0006-3495(64)86785-0.

[118] J. Rodriguez-Falces, “EMG Modeling,” in *Computational Intelligence in Electromyography Analysis*, Javier Navallas, Ed. Rijeka: IntechOpen, 2012, p. Ch. 1. doi: 10.5772/50304.

[119] C. J. Aine, Y. Okada, G. Stroink, S. J. Swithenby, and C. C. Wood, *Biomag 96: Volume 1/Volume 2 Proceedings of the Tenth International Conference on Biomagnetism*. Springer New York, 2013. [Online]. Available: https://books.google.com.lb/books?id=RZ7SBwAAQBAJ

[120] B. He, *Neural Engineering*. Springer US, 2007. [Online]. Available: https://books.google.com.lb/books?id=iw9pi1otD1EC

[121] D. Wallach and B. Goffinet, “Mean Squared Error of Prediction as a Criterion for Evaluating and Comparing System Models,” *Ecological Modelling*, vol. 44, no. 1989, pp. 299–306, 1988.

[122] S. Berro, A. Diab, M. Hajj-Hassan, M. Khalil, H. Amoud, and S. Boudaoud, “Exploration of motor unit activation pattern using high density sEMG minimum norm estimation,” in *2020 IEEE 5th Middle East and Africa Conference on Biomedical Engineering (MECBME)*, 2020, pp. 1–6. doi: 10.1109/MECBME47393.2020.9265172.

[123] D. Chicco, M. J. Warrens, and G. Jurman, “The coefficient of determination R-squared is more informative than SMAPE, MAE, MAPE, MSE and RMSE in regression analysis evaluation,” *PeerJ Comput Sci*, vol. 7, pp. e623–e623, Jul. 2021, doi: 10.7717/peerj-cs.623.

[124] S. Berro, A. Diab, M. Hajj-Hassan, M. Khalil, H. Amoud, and S. Boudaoud, “Retrieving motor unit depth using inverse approach on HD-sEMG signals,” in *2021 Sixth International Conference on Advances in Biomedical Engineering (ICABME)*, 2021, pp. 159–162. doi: 10.1109/ICABME53305.2021.9604853.

[125] L. Mesin, “Volume conductor models in surface electromyography: Computational techniques,” *Computers in biology and medicine*, vol. 43, Mar. 2013, doi: 10.1016/j.compbiomed.2013.02.002.

[126] A. Heringa, D. F. Stegeman, G. J. H. Uijen, and J. P. C. De Weerd, “Solution Methods of Electrical Field Problems in Physiology,” *IEEE Transactions on Biomedical Engineering*, vol. BME-29, no. 1, pp. 34–42, 1982, doi: 10.1109/TBME.1982.324961.

[127] V. Carriou, M. Al Harrach, J. Laforet, and S. Boudaoud, “Sensitivity Analysis of HD-sEMG Amplitude Descriptors Relative to Grid Parameter Variation,” in *XIV Mediterranean*

Conference on Medical and Biological Engineering and Computing 2016, Cham, 2016, pp. 119–123.

[128] V. Mathuranathan and M. Viswanathan, *Digital Modulations Using Matlab: Build Simulation Models from Scratch*. Independently Published, 2017. [Online]. Available: https://books.google.com.lb/books?id=gCTjtAEACAAJ

[129] D. Sandwell, "Biharmonic splines interpolation of GEOS-3 and SEASAT altimeter data," *Geophysical Research Letters - GEOPHYS RES LETT*, vol. 14, pp. 139–142, Mar. 1987, doi: 10.1029/GL014i002p00139.

[130] C. Reyes, T. Hilaire, S. Paul, and C. F. Mecklenbräuker, "Evaluation of the root mean square error performance of the PAST-Consensus algorithm," in *2010 International ITG Workshop on Smart Antennas (WSA)*, 2010, pp. 156–160. doi: 10.1109/WSA.2010.5456452.

[131] S. S. Palve and S. B. Palve, "Impact of Aging on Nerve Conduction Velocities and Late Responses in Healthy Individuals.," *J Neurosci Rural Pract*, vol. 9, no. 1, pp. 112–116, Mar. 2018, doi: 10.4103/jnrp.jnrp_323_17.

[132] L. Lindstrom, R. Magnusson, and I. Petersén, "Muscular fatigue and action potential conduction velocity changes studied with frequency analysis of EMG signals.," *Electromyography*, vol. 10, no. 4, pp. 341–356, Dec. 1970.

[133] E. J. Roelofs, A. E. Smith-Ryan, M. N. Melvin, H. L. Wingfield, E. T. Trexler, and N. Walker, "Muscle size, quality, and body composition: characteristics of division I cross-country runners.," *J Strength Cond Res*, vol. 29, no. 2, pp. 290–296, Feb. 2015, doi: 10.1519/JSC.0000000000000729.

[134] G. A. García, R. Okuno, and K. Akazawa, "A decomposition algorithm for surface electrode-array electromyogram. A noninvasive, three-step approach to analyze surface EMG signals," *IEEE Eng Med Biol Mag*, vol. 24, no. 4, pp. 63–72, Aug. 2005.

[135] C. J. De Luca, A. Adam, R. Wotiz, L. D. Gilmore, and S. H. Nawab, "Decomposition of surface EMG signals," *J. Neurophysiol.*, vol. 96, no. 3, pp. 1646–1657, Sep. 2006, doi: 10.1152/jn.00009.2006.

[136] D. Farina, R. Colombo, R. Merletti, and H. B. Olsen, "Evaluation of intra-muscular EMG signal decomposition algorithms," *J Electromyogr Kinesiol*, vol. 11, no. 3, pp. 175–187, Jun. 2001.

[137] B. He, "Advancing dynamic brain imaging with AI," *Carnegie Mellon University*, 2022.